INDC International Nuclear Data Committee

Neutron Scattering Cross Section Measurements with a New Scintillator Array

a thesis submitted to Ghent University in fulfilment of the requirements for the degree of Doctor of Science: Physics

Elisa Pirovano

Department of Physics and Astronomy, Faculty of Sciences
Ghent University

October 2017

Selected INDC documents may be downloaded in electronic form from
http://www-nds.iaea.org/publications/
or sent as an e-mail attachment.
Requests for hardcopy or e-mail transmittal should be directed to
nds.contact-point@iaea.org
or to:

Nuclear Data Section
International Atomic Energy Agency
Vienna International Centre
PO Box 100
A-1400 Vienna
Austria

Produced by the IAEA in Austria
October 2017

Neutron Scattering Cross Section Measurements with a New Scintillator Array

a thesis submitted to Ghent University submitted in fulfilment of the requirements
for the degree of Doctor of Science: Physics

Elisa Pirovano

Department of Physics and Astronomy, Faculty of Sciences
Ghent University

October 2017

Ghent University
Faculty of Sciences
Department of Physics and Astronomy

Neutron scattering
cross section measurements
with a new scintillator array

Elisa Pirovano

A thesis submitted in fulfilment of the requirements for the degree of
Doctor of Science: Physics

**FACULTEIT
WETENSCHAPPEN**

Academic year 2017-2018

Promoters:
Prof. Dr. Willy Mondelaers
Prof. Dr. Luc Van Hoorebeke

Examination Committee:
Prof. Dr. Natalie Jachowicz (Universiteit Gent, chair)
Dr. Wim Cosyn (Universiteit Gent, secretary)
Prof. Dr. Willy Mondelaers (Universiteit Gent, EC-Joint Research Centre)
Prof. Dr. Dirk Ryckbosch (Universiteit Gent)
Prof. Dr. Luc Van Hoorebeke (Universiteit Gent)
Dr. Luciano Canton (INFN-Sezione di Padova)
Dr. Roberto Capote Noy (IAEA-Nuclear Data Section)
Dr. Arjan Plompen (EC-Joint Research Centre)

Contents

Introduction 1

Nuclei are complex many-body quantum systems whose constituents interact via the strong, weak and electromagnetic forces. The study of the interactions between nucleons and nuclei aims at improving the knowledge on the fundamental processes in physics, and has important applications in both basic research and technology. Apart from studies focused on demonstrating how nuclear forces emerge from quantum chromodynamics [1], the knowledge of nuclear properties is necessary, for example, for weak-decay experiments searching for standard model violations (e.g. experiments searching for neutrinoless double beta decay [2]). Nuclear reactions are required to explain the evolution of stars [3], the origin of the elements [4], the isotopic abundances in the solar system [5], and are used in the development of dark-matter detectors [6]. The progresses in nuclear science have contributed to advances in medicine, in the use of accelerators, energy production, environmental risk monitoring, and space exploration. Theoretical models describing nuclear reactions and other nuclear phenomena (collective motion, spontaneous fission, etc.) are not yet capable of predictions accurate enough to meet the needs of the application communities, so that there is still an important interplay between experiments and theory.

Neutron-nucleus reactions (scattering, neutron-induced fission, capture) are investigated with increasing precision for several reasons. Nuclear energy is one of the main carbon-free alternatives to fossil fuel, and plays an important role in mitigating the effects of climate change and dealing with the increasing energy demand. The safe operation and the advancements of fission [7, 8] and fusion technologies [9] require complete and reliable neutron reaction datasets (cross sections, together with the angular, energy and mass distributions of the reaction products) with improved accuracy [10, 11]. Applications cannot rely on experimental data only, but need "well-behaved" data: for example, the energy-dependent data need to cover a large energy range and cannot be limited to few points. For this reason, experiments need to be evaluated: for every reaction, the existing experimental results have to be collected and selected, the datasets have to be compared, averaged, and then complemented with nuclear model calculations. The result of this process are the evaluated nuclear data libraries: files that report the evaluated data according to a documented format, with the intent of providing reliable input data for nuclear modelling and computations. Currently, several libraries exist, e.g., the OECD-Nuclear Energy Agency library JEFF [12], the U.S. library ENDF/B [13], the Japanese library JENDL [14], the Chinese library CENDL [15] and the Russian libraries BROND [16] and ROSFOND [17]. Each of these libraries has been developed and managed by a separate, often national-based, organization. In the past few years, however, a different approach has been preferred: the CIELO (Collaborative International Evaluated Library Organization) project has provided the framework for an international collaboration aimed at the development of a more accurate evaluated library [18].

Despite the remarkable progress achieved in this field, discrepancies are still observed between experiments and evaluations, for example when trying to simulate the results of benchmark experiments (e.g. [19]). The identification of discrepancies between measurements, evaluations and model calculations, is a natural cycle of the scientific process, leading to increasing completeness and accuracy of our understanding. A central role in this regard is played by the Nuclear Data Section of the International Atomic Energy Agency

(IAEA), which manages numerous international projects aimed at the development and dissemination of nuclear data for applications. An important example could be EXFOR, the database of experimental nuclear reaction data maintained by the International Network of Nuclear Reaction Data Centres (NRDC) under the coordination of the IAEA [20].

From a scientific point of view, the interest in neutron reactions is due mainly to the fact that a full quantitative and even qualitative description of the nuclear interactions is still missing. As an example, for fission, a complete theoretical model is still not available due to the difficulty of describing the motion of each nucleon through the process [21]. Neutron induced reaction data are necessary for the understanding of the nucleon-nucleon interactions [22], find application in the development of nuclear potential models and in nuclear structure studies [23].

1.1   Why neutron elastic scattering

High energy-resolution measurements of elastic scattering differential cross sections are carried out in the interest of nuclear engineering and nuclear applications. Not only engineering, however, can benefit from such measurements: neutron scattering is a unique tool for probing the nucleus and has importance for several branches of nuclear science. In theoretical studies of nuclear interactions, for example, neutron scattering data are necessary for the determination of the parameters describing the nucleon-nucleon potentials. In particular, when the optical potential model is considered, proton and neutron elastic scattering data are necessary because they provide the constraints for the determination of the potential parameters [24–26]. In general, the differential cross sections are used as means of validating theoretical predictions, regardless of whether the calculations are based on phenomenological optical potentials or on the so-called microscopic potentials and interactions derived from the available options of the basic nucleon-nucleon interaction [27]. In particular, such descriptions based on microscopic theory are an active field of investigation and interesting results have been obtained by state-of-the-art parametrisations based on meson-exchange [28], and more recently on effective field theory as the low-energy limit of quantum chromodynamics [29].

For applications where neutrons are involved (not only energy production, but also particle accelerator design, detector development, medical radiotherapy, space travel, etc.), elastic scattering represents the dominant scattering mechanism, of key importance in modelling problems, e.g. with Monte Carlo simulations of neutron transport. It is a reaction channel that is always open, its cross section in the MeV range is typically 50% of the total cross section, and the angular distributions are necessary to determine the neutron flux spatial distribution. For example, in case of shielding calculations, and for criticality as well as for radioprotection assessments, differential cross sections are necessary for the determination of the leakage and backscattering terms. Moreover, it strongly influences the energy distributions and reaction rates as the maximum energy that can be lost in an elastic collision is inversely proportional to mass of the target. This becomes primarily significant when light elements are present in large quantities, e.g. when water or plastic are extensively used.

1.1.1   Carbon

The first experiment presented here is a measurement of the double differential cross section of neutron elastic scattering on carbon. As the carbon cross section is known with high accuracy in the energy range of fast neutrons, this measurement served as proof of principle of the experimental technique and the data analysis method that will be later introduced.

Due to the moderation properties of carbon, its low capture cross section and the widespread availability, graphite is extensively used in nuclear applications. In fission and fusion reactors, for example, graphite is often employed as moderator, reflector, and also as fuel matrix. Since carbon scattering data are required for neutron transport calculations and

the modelling of several different systems, numerous measurements have been carried out starting from the forties. The existence of a large amount of data with reasonable accuracy was one of the reasons why in the seventies the differential cross section of neutron elastic scattering on natural carbon was proposed as a standard [30]. The other motivations include the easy availability of good quality carbon (graphite) samples, and the high inelastic scattering threshold, equal to 4.812 MeV of neutron energy in the laboratory system.

The carbon differential elastic scattering cross section is considered a standard for neutron cross sections only up to 1.8 MeV [31]. Its application for energies above 2 MeV is not recommended because of the presence of resonance structures, except for the case of high energy-resolution measurements. Even so, the accuracy of the evaluation for the elastic scattering cross section is of the order of 1% up to the inelastic scattering threshold, while below 1.8 MeV it ranges from 0.46% to 0.6%. Therefore, if the regions around the resonances are overlooked, it can still be considered a suitable cross-section standard up to 4.8 MeV as it is based on accurate total cross section data. Below the inelastic threshold the only non-elastic process is neutron capture. Its cross section, however, is negligible above thermal energies, two to five orders of magnitude lower than the elastic cross section. So, in practice, the elastic cross section can be taken as identical to the total cross section.

The resonances that limit the use as a cross section standard provide a method for checking the consistency of the neutron energy scale. The first resonance at 2078.05(32) keV is a recognized neutron energy standard [32]. It happens when the (^{12}C,n) reaction reaches the level at 6863 keV in ^{13}C, and has a total width of 6 keV. A second structure that could be used as energy reference is the resonance at 2816(4) keV, which corresponds to the ^{13}C level at 7547 keV and is less than 5 keV wide [30, 32].

1.1.2 Iron

Iron is extensively used as structural material in a variety of systems and most large infrastructures. For this reason, in nuclear facilities where neutrons are generated, the data regarding the angular distributions of neutron scattering on iron are often required for their development, design and safe operation.

In charged-particle beam lines, for example, neutrons are produced when the beam collides on the surrounding media, when it interacts e.g. with the energy degrader or the target (if used), the beam stopper or the beam collimators and deflectors. For radiation protection assessments, in order to establish shielding requirements, the neutron dose rates around the accelerator and the beam lines have to be determined. Monte Carlo models simulating the transport and interaction of both charged particles and neutrons allow to compute the neutron source terms and the other quantities of radiological interest [33]. The neutron field depends not only on the source term distribution, but also on neutron interactions with the surrounding materials. For this reason accurate data on neutron scattering on iron are necessary.

In fission reactors, depending on the reactor type and the vessel structure, the iron volume can be up to ten times higher than that of the fuel. The neutron energy spectrum, the spatial distribution, and the reaction rates, are therefore strongly influenced by interactions with iron. In Generation-IV sodium-cooled fast reactors, for example, the neutron leakage from the core is limited by means of stainless steel reflectors. This means that the calculation of the neutron leakage from the core and of the backscattering term are greatly impacted by the accuracy of the double differential cross section of scattering on iron. In [10], the ^{56}Fe scattering data are cited as one of the major sources of the overall uncertainty in the determination of the most important integral parameters, such as multiplication factor, reactivity coefficients, and power distributions.

The neutron inelastic scattering cross section on ^{56}Fe is an item on the High Priority Request List of the OECD-NEA Data Bank for nuclear data measurements [34]. The target accuracy for this cross section depends on the intended use: it goes from 2% for the Accelerator-Driven Minor Actinides Burner to 7%–9% for the European Fast Reactors. In the current evaluations, the uncertainties range from 7% up to 25%. Moreover, some discrepancies have been found between evaluated and experimental integral cross-sections.

In [35], the results of a spherical shell transmission experiment are reported for three energies between 6 MeV and 11 MeV. The authors suggest that in this energy range the inelastic cross section reported in the ENDF/B-VII library should be 21% to 35% lower.

The number of experiments regarding the scattering angular distributions available in EXFOR for energies higher than 1 MeV is limited. For elastic scattering, differential cross sections were measured with high energy resolution only up to 3 MeV; above 3 MeV, angular distributions were measured only for a restricted number of energies. For inelastic scattering, there are no measurements with a high energy resolution for the differential cross section above 2 MeV. The scarcity of experimental data poses a problem because the iron cross section is characterised by large fluctuations, which are difficult to model otherwise. Below 5 MeV, the predictions based on the optical model do not reproduce the behaviour of the total cross section [26], which implies that elastic scattering is not appropriately represented either. New experimental data describing the elastic scattering distributions provides important guidance for improving the model and the overall description.

All these arguments explain why iron was chosen for the pilot project of the CIELO collaboration [18]. For the same reasons, it was decided that the first experiment in this thesis work of interest for nuclear applications is a measurement of neutron scattering on iron.

1.1.3 Deuterium

Neutron scattering on deuterium represents one of the simplest cases for the application of many-body theory in nuclear physics. For this reason, the experimental observables of this reaction are often used to validate the predictions of theoretical works investigating the three-nucleon forces [28, 36–38]. The main topic of these works is demonstrating how the three-body forces emerge from the principles of the low-energy quantum chromodynamics or meson-exchange based interactions. In recent studies in the framework of the effective field theory [29, 38], the chiral perturbation theory has been applied to investigate the n-d elastic scattering and breakup reactions. For neutron energies below 20 MeV, the theory reproduces well the elastic scattering cross section data, while discrepancies are still observed between predictions and spin observables.

The differential cross section of neutron elastic scattering on deuterium is also an item in the OECD-NEA High-Priority Request List. The experimental angular distributions in EXFOR are scarce and partially inconsistent, the discrepancies being especially evident at backward angles [39]. Evaluation and experiments are generally consistent when it comes to the total elastic cross sections. When the angular distributions are considered, however, an overall poor agreement is observed [39]. Moreover, the evaluated double differential cross sections were found to be a source of inconsistencies when trying to reproduce benchmark experiments for heavy-water moderated critical assemblies [19, 40].

The discrepancies in the evaluated libraries do not only affect criticality calculations for heavy-water moderated reactors: there are multiple applications that require accurate deuterium data. In neutron metrology, for instance, the n-d scattering cross section is necessary to compute the energy distribution of the D_2O-moderated ^{252}Cf fission neutron reference field, which is used for example to calibrate neutron dosimeters [41]. Another example is provided by detector physics: a thorough knowledge of the reaction is crucial for the proper characterisation of C_6D_6 scintillation detectors, whose response to neutrons is a function of the n-d scattering angular distribution [42]. This issue was encountered during this work too, and it will be shown how inaccuracies in the deuterium evaluations affect neutron yield measurements.

1.2 Objectives of the PhD project

The main objectives of this work are the development of a new experimental setup and method for the investigation of neutron scattering reactions, to demonstrate it on the basis of scattering on carbon, and to deliver new data of interest on deuterium and iron. The data should be of a quality and completeness suitable for nuclear applications, with an

important focus in the field of energy production. The goal is therefore the realization of a measurement setup that allows the determination of scattering cross sections and angular distributions as a function of neutron energy with a high energy resolution and low total uncertainty. The PhD work focuses on elastic scattering but in addition explores the potential of the setup and method for the measurement of both elastic and inelastic scattering double differential cross sections. The neutron energy range of interest for iron, and in general for elastic scattering, is that of fast neutrons, above 1 MeV. For this reason the setup developed for this thesis work is based on liquid organic scintillators.

During the course of the work it became clear that the foreseen digitizer-based data-acquisition system with new models from SP Devices in reality involved prototypes suffering from several set-backs that required time-consuming iterations with the manufacturer before they were finally suitable for use. These setbacks were eventually solved and in the final half year of the contract data could be taken for carbon and iron on which most of the results of chapters 3, 4 and 5 are based. To ensure timely completion of a publishable result within the course of the thesis, an improved n-d scattering experiment was undertaken in the low-scattering facility nELBE of the Helmholtz-Zentrum Dresden-Rossendorf with lithium glass scintillators to target an energy range of interest to application (below 2 MeV neutron energy).

Similarly, the slow progress with the data-acquisition system and the concerns that were raised warranted a comparison with a state-of-the-art conventional data-acquisition system. For this reason a second experiment for n-Fe scattering was carried out at nELBE with two arms of the new spectrometer from Geel. The low room background and different intensity ratio of gamma and neutron response at nELBE compared with GELINA made this a further comparison of interest to the new setup. Finally, two additional measurements were made at the Physikalisch-Technische Bundesanstalt (PTB) in Braunschweig that have not been analysed yet, but could have served to better validate the new analysis procedure and to provide further data of interest in support of the PhD work, should the development of the new data-acquisition system not be finalised in time. This concerned another measurement of n-d scattering with a completely different method (using a gas proportional counter), and a measurement dedicated to the determination of response functions for the liquid scintillators used at nELBE and at GELINA. Work on these two experiments was postponed in favour of first measurements for carbon and iron with the new digitizer based data-acquisition system for carbon and iron. It is important to note that the data for n-d scattering obtained at nELBE are of importance also for the development of the new setup since they provide a direct comment on the quality response functions for half of the employed detectors.

1.3 Organisation of the thesis

The experimental methods, and reasons for the implemented solutions, are explained in chapter 2. The technical specifications, the data acquisition system, and the detector characterisation, will be presented in chapter 3. In chapters 4 and 5, the experiments on carbon and iron will be described, and the results for the elastic scattering cross section will be discussed. Finally, in chapter 6, a complementary experiment, with a different detector array, will be presented. There, the asymmetry of the neutron scattering on deuterium will be examined. Chapter 6 is a reprint of a paper published in Physical Review C, volume 95, article 024601 (2017), that resulted from the work of this thesis [43].

Experimental methods

2

The neutron scattering experiments presented here have the following common structure. A white neutron source is used to generate neutrons which are first collimated to form a beam, then directed on a sample of the investigated material (the target). During the irradiation, a neutron monitor is placed upstream to measure the incoming neutron flux Φ_{in}, while an array of neutron detectors surrounds the target to determine the scattered neutron rate as a function of the scattering angle. The rate of detected events R is given by the intrinsic detection efficiency ε and the rate of neutrons striking the detector, which in turn depends on the detector opening angle $\Delta\Omega$, the neutron flux Φ_{in}, the number of target nuclei exposed to the neutron beam n_T, and the differential cross section $d\sigma/d\Omega$. This can be summarized by the expression:

$$R = \varepsilon\,\Delta\Omega\,n_T\,\Phi_{in}\,\frac{d\sigma}{d\Omega} \tag{2.1}$$

If A_b is the cross-sectional area of the neutron beam, then the flux can be written as J_{in}/A_b, where J_{in} is the neutron current, and n_T can be written as $A_b\,\rho_T$, where ρ_T is the atomic areal density of the target. The expression for deducing the differential cross section (its average over the solid angle $\Delta\Omega$) can therefore be written as:

$$\frac{d\sigma}{d\Omega}(E,\theta) = \frac{R(E,\theta)}{\varepsilon(E')\,\Delta\Omega\,\rho_T\,J_{in}(E)} \tag{2.2}$$

where θ is the scattering angle, defined by the detector position relative to the neutron beam, E is the energy of the incident neutron on the target, and E' is the neutron energy after the interaction with the target. The expression still holds when flux and and reaction rate are measured in nearby locations with a slightly diverging beam provided that sample and flux monitor intercept the whole beam.

In order to apply equation (2.2), the neutron energy before and after the collision on the target must be determined. For a white neutron beam, this may be obtained by applying the time-of-flight method, provided the interaction is binary and the scattering process (elastic scattering, inelastic scattering from the first excited state, etc) is known. The target finite size effects such as multiple scattering corrections are important factors to consider and must be evaluated. The signals from neutron events have to be isolated from the detected photons, the different reaction processes (elastic and inelastic) must be separated, and the detection efficiency has to be determined. A key role in this is played by the characterisation of the detectors, and in particular in the determination of its response to neutrons and photons.

In this chapter, the main aspects of the experimental method and the neutron time-of-flight technique will be introduced. The basic working principles of the neutron detectors, why they were chosen, and how it is possible to take advantage of their characteristics to separate elastic from inelastic scattering events will also be explained. The technical specifications and the detector characterisation will be described in chapter 3, where the details of the neutron/photon discrimination procedure, the detector response and detection efficiency determination will be illustrated. For the multiple scattering correction, a
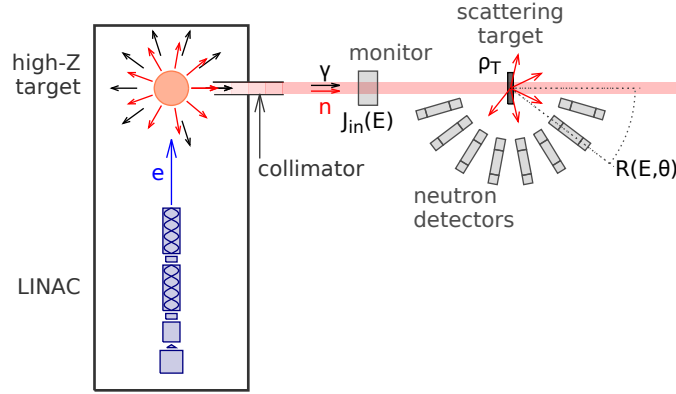
Figure 2.1: General structure of a time-of-flight measurement for the determination of neutron scattering cross sections. The bremsstrahlung photons and the collimated neutron beam, produced by an electron-linac-driven source, strike on a sample of the investigated material, which is characterised by an atomic areal density ρ_T. The incident neutron current $J_{in}(E)$ is measured as a function of the neutron energy E by a monitor placed upstream the target. The other neutron detectors record the scattering reaction rate $R(E, \theta)$ as a function of E and the scattering angle θ.

practical example will be given for the measurements with the carbon target in chapter 4, where all other results will be also applied to determine the differential scattering cross section of n-C elastic scattering.

2.1   Determination of the neutron energy

To make a sensible cross section measurement, the incident neutron energy on the target has to be determined, and the appropriate technique depends on the nature of the neutron source. The experimental setup was designed and assembled at the GELINA facility (in Geel, Belgium) [44]; most of the measurements here presented were carried out there. The experiment on iron, however, was also repeated at the nELBE facility (Dresden, Germany) [45], with a part of the setup of GELINA. Finally, the measurements of deuterium were also carried out at the nELBE facility with a setup using different detectors. In both facilities, neutrons are produced by an electron-linac-driven source, via the photo-nuclear reactions induced by the bremsstrahlung caused by the electron beam striking a high atomic number target (see the basic configuration shown in figure 2.1).

Both at nELBE and GELINA, the neutron energy measurement is achieved by applying the time-of-flight (t.o.f.) technique. The accelerators are operated in pulsed mode: each pulse produces a sharp flash of bremsstrahlung (the so-called γ-flash) and a burst of neutrons with a wide energy distribution. The t.o.f. required to travel from the source to the detector is known a priori for photons ($t.o.f._\gamma$): it depends on the speed of light and on the distance between source and detector. The difference between the arrival time of photons (t_γ) and neutrons (t_n) therefore can be used to determine the neutron time-of-flight: $t.o.f._n = t_n - t_\gamma + t.o.f._\gamma$ The neutron energy is a function of the t.o.f., and the explicit expression can be determined by studying the experiment kinematics.

In scattering experiments, the time-of-flight corresponds to the time required to travel from the source to the target, and then from the target to the detector. It depends on the kinetic energy both before and after the collision (E and E'), and can be written as:

$$t.o.f. = \frac{L}{c\sqrt{1 - 1/\left(1 + E/mc^2\right)^2}} + \frac{L'}{c\sqrt{1 - 1/\left(1 + E'/mc^2\right)^2}} \tag{2.3}$$

where c is the speed of light, m the neutron mass, and L and L' are the length of the flight paths of the incident and scattered neutrons, respectively. Due to the two body kinematics, the energy after the scattering depends just on the initial energy and on the scattering angle. Therefore, it is possible to infer the neutron energy incident on the target through the t.o.f. measured with a fixed detector.

The expression of E' as a function of E and the scattering angle θ can be obtained from the conservation of energy and momentum. In case of elastic scattering from a nucleus of mass M, in the laboratory frame of reference, E' is given by:

$$E'(Mc^2 + mc^2) - E(Mc^2 - mc^2) + E'E = c^2 p p' \cos \theta \qquad (2.4)$$

where $p = \sqrt{E(E + 2mc^2)}/c$ and $p' = \sqrt{E'(E' + 2mc^2)}/c$ are the neutron momentum before and after the collision. For inelastic scattering the equivalent expression is found by adding the excitation energy E^* of the target nucleus to its rest energy:

$$2E'(Mc^2 + mc^2) - 2E(Mc^2 - mc^2) + 2E'E + E^*(2Mc^2 + E^*) = 2c^2 p p' \cos \theta \qquad (2.5)$$

The solution for E of equation (2.3) was obtained based on the assumption that the different reaction processes can always be separated, which means that the value of E^* (zero, for elastic scattering), is always known. An iterative procedure was implemented. For the first iteration ($i = 0$), the average neutron velocity $v_0 = (L + L')/t.o.f.$ is considered, and the incident energy is approximated by: $E_0 = mc^2(-1 + 1/\sqrt{1 - (v_0/c)^2})$. The energy after the collision E'_0 is calculated using equation (2.5), then equation (2.3) is applied to obtain the first estimate of the time-of-flight t_0. For the iteration $i + 1$, the difference between the measured t.o.f. and t_i is used to correct the incident energy: $E_{i+1} = E_i (t_i/t.o.f.)$. This correction only implies that if the calculated time is too long, then it means the neutron should be faster than what was first estimated. The iterations stop when the difference between t_i and the measured t.o.f. is less than 10^{-4} ns.

2.2 Choice of the scattering angles

The typical approach to present the scattering differential cross section is to express it as a Legendre expansion:

$$\frac{d\sigma}{d\Omega} = \frac{\sigma(E)}{2\pi} \sum_{l=0}^{N_l} \frac{2l + 1}{2} a_l(E) P_l(cos\theta) \qquad (2.6)$$

where E is the incident neutron energy and θ the scattering angle, $\sigma(E)$ is the scattering cross section, $P_l(cos\theta)$ is the lth order Legendre polynomials, $a_l(E)$ is the corresponding coefficient, and N_l is the highest order for which a_l is available. The zero-order coefficient a_0 is, by definition, equal to 1; all other coefficients are determined combining experiments and evaluations. The angle θ is normally given in the centre-of-mass reference system; the structure of the expansion however does not change in the laboratory system, the coefficients a_l just assume different values and the number of terms may differ. Expressions (2.6) and (2.7) (to follow) are valid in both the centre-of-mass and laboratory reference frames. Therefore, unless it is specified otherwise, only the laboratory system will be considered here.

The number of coefficients in (2.6) that is possible to determine with one single measurement depends on the number of scattering angles covered by the neutron detectors: more measurement angles means more coefficients. In the new experimental setup the detectors are placed at 8 different angles, which should allow us to determine, in principle, the Legendre coefficients up to the 7th order.

The number of measurement points should be sufficient for a representative comparison with the models. Taking elastic scattering below 6 MeV as a reference, the evaluated nuclear data libraries report coefficients up to the 10th order for deuterium, up to the 6th order for carbon, and up to the 15th order for iron. This means that in the case of carbon the presented measurements should be enough to fully characterise the angular distributions.

Table 2.1: Angles between the detector axis and the neutron beam direction, and corresponding weights for the application of the Gauss-Legendre quadrature rule (equation (2.7)).

angle (°)	cosine	weight
163.8	-0.960290	0.101229
142.8	-0.796667	0.222381
121.7	-0.525532	0.313707
100.6	-0.183435	0.362684
79.4	0.183435	0.362684
58.3	0.525532	0.313707
37.2	0.796667	0.222381
16.2	0.960290	0.101229

For iron, 8 points are enough for the full characterisation up to 3 MeV. Above, they are still sufficient for the appraisal of the evaluations.

The final results will be strongly limited by the experimental uncertainties, so it might not always be possible to determine all possible coefficients. The intention is to assess at least the first and second order coefficients, and to provide the upper limit for the third one. This choice is motivated by the fact that the first and second order coefficients are the most important ones for nuclear applications, because they describe the forward to backward asymmetry of the scattering reaction and the probability of backscattering.

The scattering angles, defined in practice as the angles between the detector axis and the neutron beam direction, are reported in table 2.1. The reason behind these particular angles lies in the choice of the numerical integration technique used to determine the integral cross section from the differential data. More explicitly, the cosines of these angles correspond to the zeros of the Legendre polynomial of 8th order, allowing 8-points Gauss-Legendre quadrature to calculate the cross section σ by:

$$\sigma = 2\pi \sum_{i=1}^{8} w_i \cdot \frac{d\sigma}{d\Omega}(\cos\theta_i) \tag{2.7}$$

where θ_i are the angles, w_i the weight factors (reported in table 3.1), and $\frac{d\sigma}{d\Omega}(\cos\theta_i)$ is the differential cross section measured at θ_i.

In general, the n-points Gauss-Legendre quadrature rule is constructed to give the exact result of $\int_{-1}^{1} p(x)\,dx$ for any polynomial $p(x)$ of order $2n - 1$ or less. If the Legendre polynomial expansion of the differential cross sections is considered, it means that, with 8 points, it is possible to accurately integrate over distributions represented by expansions up to the 15th order. This includes the elastic scattering distributions of all three cases here presented (deuterium, carbon and iron) at least up to 6 MeV of neutron energy.

2.3 Neutron detectors

2.3.1 Liquid organic scintillators

When talking about nuclear applications, in particular about energy production, the importance of neutron scattering is due to its role as moderation mechanism for neutrons in the fast energy range. Therefore, the measurements were aimed at the range from 1 MeV to 20 MeV: below 6 MeV is for fission applications, while above 6 MeV is relevant for fusion and accelerator-driven systems (e.g. MYRRHA [46]). Accordingly, liquid organic scintillators were chosen as neutron detector because they are sensitive to fast neutrons, with their detection efficiency typically reaching the maximum at around 1-2 MeV. Two types of detectors were considered: EJ301 [47] and EJ315 [48] scintillators. The EJ301 detectors (NE213 equivalent) use scattering on protons (^{1}H nuclei) as the conversion reaction for neutron detection, while in the EJ315 detectors (C_6D_6 detectors) the neutrons scatter on the

deuterium nuclei. The neutron response of the two detector types depends on the cross section of the n-p and the n-d scattering, and the pulse height distributions in particular are a function of the scattering angular distributions. This dependence can be explained by considering the relationship between the proton/deuteron recoil energy (proportional to the detector signal pulse height) and the scattering angle. In non-relativistic approximation, the energy $E_{r,LAB}$ of the recoil nucleus in the laboratory system (LAB) is a function of the neutron scattering angle θ_{CM} in the centre of mass reference system (CM) [49]:

$$E_{r,LAB} = E_{n,LAB} \frac{4A}{(A+1)^2} \frac{1-\cos\theta_{CM}}{2} \tag{2.8}$$

where $E_{n,LAB}$ is the incoming neutron energy in the LAB system, and $A = m_T/m_n$ is the ratio between the target mass m_T (in this instance, $T = p$ or d) and the neutron mass m_n. Therefore, the recoil energy distribution $dN_r/dE_{r,LAB}$ in the LAB depends on the neutron scattering angular distribution in the CM:

$$\frac{dN_r}{dE_{r,LAB}} = \frac{4\pi}{\sigma_{el}} \frac{1}{E_{r,LAB}^{MAX}} \frac{d\sigma_{el}}{d\Omega_{CM}} \tag{2.9}$$

where $E_{r,LAB}^{MAX} = E_{n,LAB} \, 4A/(A+1)^2$ is the maximum recoil energy, and $d\sigma_{el}/d\Omega_{CM}$ and σ_{el} are the differential and angle-integrated cross sections of neutron elastic scattering as a function of the incident energy $E_{n,LAB}$. For this reason, detectors that use scattering on different nuclei as conversion for neutron detection, produce different spectra when irradiated with neutrons of the same energy. The different behaviours provide a means to perform consistency checks and to find out potential systematic errors.

EJ301 and EJ315 scintillators have a time resolution typically lower than 1 ns and allow neutron/photon separation via pulse shape analysis, therefore they are well suited for neutron time-of-flight experiments. Since the pulse-height distributions produced by n-p or n-d scattering are a function of the neutron energy, both EJ301 and EJ315 scintillators can be used for neutron spectrometry. Being able to determine the neutron energy distribution incident on the detectors provides a means for discriminating scattering reactions. The neutron energy at the detector (energy after the collision in the target) is different for different reactions, and for scattering in particular it can be calculated using equations (2.3), (2.4) and (2.5). For this reason, the measured neutron energy distributions can be used to identify the different scattering reactions and determine their yield. In principle a full response unfolding could be applied to determine the energy distributions [50], but as the neutron energy is already known from the kinematics, in this work a different approach was used which was focused on the systematic investigation of the role of the response function in relation to the desired differential cross section.

2.3.2 Lithium-6 glass scintillators

In the deuterium experiment, the measurements were aimed at energies below 2 MeV; the results cover the interval from 200 keV to 2 MeV. Organic scintillators are not suited for experiments with these energies because the detection efficiency drops quickly below 1 MeV. Lithium glass detectors enriched in lithium-6 were employed instead. These detectors have a typical time resolution of few nanoseconds, and therefore can be used for time-of-flight experiments. Neutrons are detected via the ^{6}Li(n,α)^{3}H reaction, and produce signals whose integral (the integrated charge) is proportional to the energy deposited by the α particle and the tritium. The ^{6}Li(n,α) reaction is characterised by a fairly large Q-value, equal to 4.78 MeV. This means that neutrons can be discriminated from photons or other low-amplitude events by applying a proper gate on the registered integrated charge values. The spectrometric capabilities of the lithium glass detectors were not investigated because below 2 MeV the only relevant neutron reaction is elastic scattering. The maximum detection efficiency of the lithium glass detectors (8% for neutrons with about 240 keV energy) is less than one third of the maximum efficiency of the organic scintillators (30% to 40% for energies between 1 MeV and 2 MeV). Because of the low efficiency, it was necessary to have

more than one detector at the same angle. For this reason, it was not possible to study the full angular distribution, but only two angles were considered. The experiment therefore focused on the study on the backward-forward asymmetry of the reaction.

2.4   Past investigations

At the end of the eighties, a similar detector array, consisting of 8 organic liquid scintillators, was designed and developed at GELINA [51]. The objective was the same: the measurement of double-differential neutron-emission cross sections in the fast energy range. The method was also similar: the idea was to classify reactions (elastic and inelastic scattering events) on the basis of the neutron energy after the collision, via the unfolding of the t.o.f.-dependent pulse height distributions.

   The procedure here presented does not exactly rely on the detector response spectral unfolding: a simpler solution was sought, considering that the neutron energy at the detector is, in principle, known a priori. The techniques for the detector response characterisation do not change from the point of view of the theory, but it is now possible to apply them by using more powerful simulation tools. Moreover, in view of the past experience, both proton-based (EJ301) and deuterium-based (EJ315) detectors were employed, as the different response functions allow a better understanding of their role. The design is different: in the past, the detectors were placed as close as possible to the target without intercepting the neutron beam. In the present setup, the choice of the scattering angles was based on the possibility of applying numerical techniques for the angle integration. This resulted in a larger distance from the detector to the scattering target (from 20 cm to 30 cm) but also in a larger angle coverage (from 20°–160° to 16°–164°). The data acquisition techniques were improved, and provide greater flexibility and reduced concern for dead time due to γ-flash events.

   The most important difference, however, is represented by the results that could be obtained. The first setup was never systematically employed for routine measurements due to the difficulties encountered in the data analysis. The cross section of elastic scattering on sodium, for example, was found to be inconsistent [52]. This did not turn out to be a problem with the present setup, and that the presented method has good potentialities for studying both elastic and inelastic scattering.

3
A scintillator array
for neutron spectrometry

The whole experimental installation at GELINA is new, including the neutron beam collimation, designed to optimize the neutron flux at the sample position while reducing the background that reaches the detectors; the detector supporting frame, designed to minimize the neutrons scattered; and the data acquisition system based on digitizers, whose implementation was the most challenging part of the development. The complete setup, which was designed in 2013, is fully operational since 2016.

After a brief description of the facilities (GELINA and nELBE) and of the experimental equipment, this chapter is devoted to the procedure for the scintillator characterization and the analysis of their response, depending on the detected particle. This is a crucial feature whose accuracy controls the uncertainties of the results.

3.1 Neutron time-of-flight facilities

3.1.1 GELINA

GELINA (Geel Electron LINear Accelerator) is the pulsed white neutron source for high resolution neutron data measurements operated by the Joint Research Centre in Geel (JRC-Geel) [44]. The facility consists of four main elements: the electron linear accelerator, the compression magnet, the neutron producing target and the flight paths with the measurement stations (see figure 3.1). The linac produces electrons in pulses of typically 10 ns width (full width at half maximum), at a repetition rate up to 800 Hz. The electron energy varies linearly from 140 MeV at the start of the pulse to 70 MeV at its end. This time-correlated linear energy decrease makes possible the use of the compression magnet to reduce the pulse width: when the electrons pass through the 360° deflection dipole magnet, the early high energy electrons travel a large circle while the late low energy electrons travel a shorter circle. Tuning the field ensures a simultaneous exit with a spread (FWHM) of less than 1 ns [53]. The neutron source is a mercury cooled rotating target made of an alloy of molybdenum (10%-weight) and depleted uranium. When the electron beam hits the target, neutrons with a fission like spectrum are produced via (γ,xn) and (γ,f) reactions. In order to increase the number of neutrons with energy below 100 keV, two beryllium tanks filled with water are mounted above and below the target in order to act as moderators for fast neutrons. GELINA serves 12 flight paths, which are built in a star-like configuration around the uranium target. For each flight path, two flux conditions are available: one optimised for energies below 100 keV and the other with fast neutrons. The two different conditions are obtained by placing shadow bars between the source and the given flight path to shield either the neutrons coming directly from the uranium target or the moderated neutrons.

The experimental setup was installed along the new flight path at 108° from the electron beam, in the measurement cabin placed at the nominal distance of 30 m from the neutron source. It is the most backward flight path with respect of the electron beam direction, so
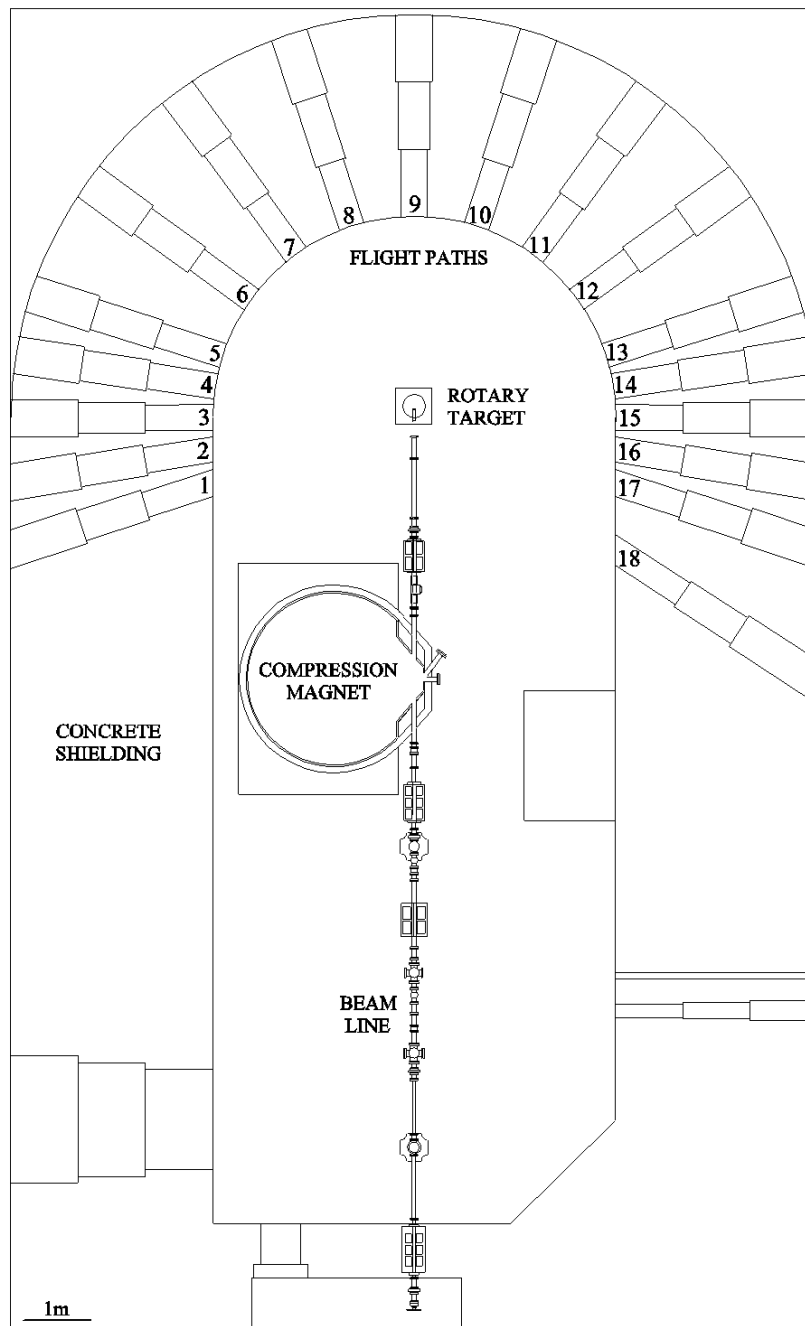
Figure 3.1: Scheme representing the main elements of GELINA: electron accelerator, compression magnet, uranium target, flight paths. Eighteen flight paths are in principle available, GELINA serves only twelve of them; flight paths 7, 8, 9, 10, 11 and 18 are not used. The present work made use of flight path 1, at 108° to the electron beam.
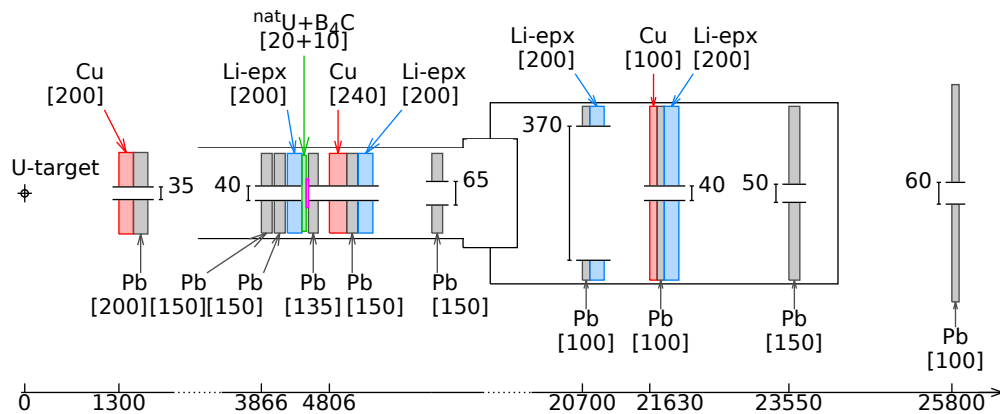
Figure 3.2: Scheme of the collimation for the flight path at 108°. The collimation system consists of a set of pierced disks made of lead, copper and lithium epoxy ("Li-epx") of variable thickness (in square brackets) and with different internal diameter. Two filters are used: a natural uranium filter (for photons) and a boron filter (for slow neutrons). The axis below the figure indicates the distance of the collimators and filters to the neutron producing targets. All dimensions are given in millimetres.

it is where the self-attenuation of the uranium target is at its lowest and the neutron flux has the highest intensity. The energy range of interest is that of fast neutrons; therefore, the unmoderated neutron flux condition was selected. The neutron beam travels from the target hall to the measurement cabin in a tube of 50 cm diameter kept under vacuum. Along the tube, collimators made of copper (fast neutron absorber) are installed to define the beam size, while collimators of lithium epoxy and lead absorb slow neutrons from the moderator and photons (the scheme of the collimation is shown in figure 3.2). An uranium filter (natural uranium) of 2 cm thickness and a boron filter (boron carbide, B_4C) of 1 cm are also used to reduce the bremsstrahlung intensity, and to remove thermal neutrons. The beam profile has been measured with a photographic film and a neutron camera, obtaining a beam diameter of 4.6(1) cm at the exit of the tube and 4.9(2) cm at the scattering target position.

3.1.2 nELBE

nELBE is the neutron time-of-flight facility installed at ELBE, the superconducting Electron Linac for beams with high Brilliance and low Emittance of the Helmholtz-Zentrum Dresden-Rossendorf (HZDR) [54,55]. At nELBE [45], neutrons are produced via (γ,n) reactions by the electron beam impacting on a liquid lead target (see figure 3.3 for a diagram of the facility). The lead flows through a closed circuit driven by an electromagnetic pump at a stabilized temperature of 430°C. The target consists of a molybdenum channel of rhombic cross-section with an inner side length of 11 mm. The neutrons are emitted almost isotropically while the bremsstrahlung is forward peaked: the collimator that defines the neutron beam (a steel tube with lead and borated polyethylene inserts) was therefore placed at 95° with respect to the primary electron beam. At the entrance of the collimator, different absorbers can be set up to adjust the beam properties such as the bremsstrahlung intensity. The experimental hall is separated from the neutron radiator by a 2.5 m thick wall of heavy concrete. There, the detector setup was located at 8.3 m from the neutron radiator.

3.2 The neutron spectrometer

The setup for the measurement of neutron scattering differential cross sections that has been developed for t.o.f. experiments at GELINA is shown in figure 3.4a. It includes a ^{235}U fission chamber for the measurement of the incoming neutron flux and 32 liquid organic
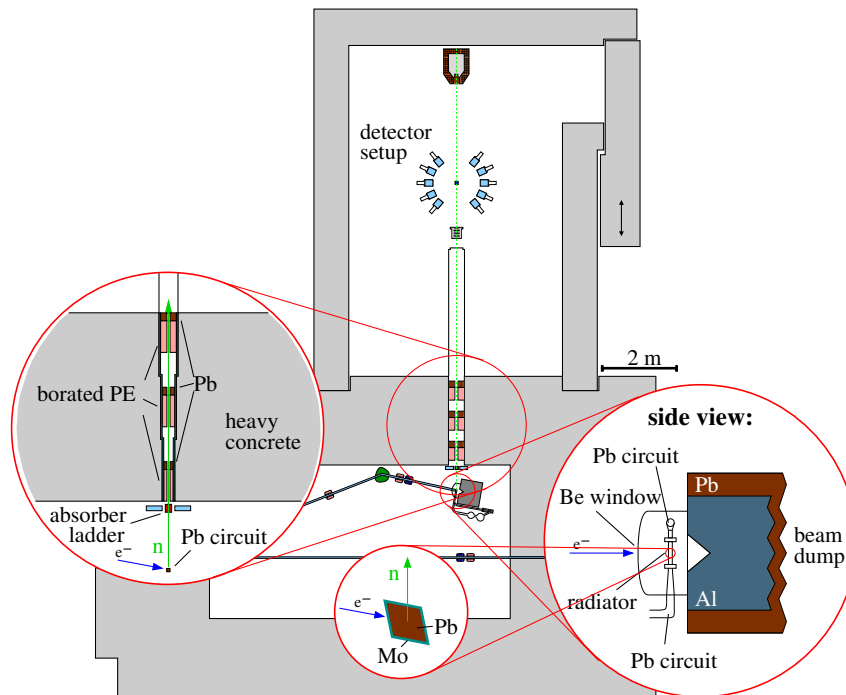
Figure 3.3: Scheme representing the neutron time-of-flight facility nELBE: the electron beam impacts on a liquid lead target confined in a molybdenum channel, the neutron beam is defined by a collimator installed at 95°, and the detector setup is separated from the neutron radiator by a 2.5 m thick wall of heavy concrete.

Table 3.1: Angles between the scintillator axes and the neutron beam direction.

angle (°)	cosine
163.8(1)	-0.9603(5)
142.8(1)	-0.7967(11)
121.7(1)	-0.5255(15)
100.6(1)	-0.1834(17)
79.4(1)	0.1834(17)
58.3(1)	0.5255(15)
37.2(1)	0.7967(11)
16.2(1)	0.9603(5)

scintillators for the detection of the scattered neutrons. The fission chamber is placed upstream at 1.37 m from the scattering target. The scintillators are arranged around the target in four sets of 8 detectors each. For each set, the detectors are mounted at specific angles to the neutron beam direction (see scheme in figure 3.4c) and table 3.1. The uncertainty on the angles is of 0.1°, which is the accuracy achieved in the construction of the frame supporting the detectors. The distance between the front face of detector housing and the centre of the target is of 30.0(3) cm.

### 3.2.1 Liquid organic scintillation detectors

The fast neutron detectors used in this setup are commercially available liquid organic scintillators manufactured by Scionix. Two sets of eight are filled with the EJ301 scintillation liquid (detector model: 51A51/2MQOE1-EJ301-NX), the other two sets with EJ315 (model: 51A51/2MQOE1-EJ315-NX). The EJ301 liquid (by Eljen Technology) is equivalent to the NE-213 [47], while the EJ315 is highly purified deuterated benzene (C_6D_6) with a ^{2}H to ^{1}H ratio of 141 to 1 [48] (details in table 3.2). Both models are cylindrical detectors, with
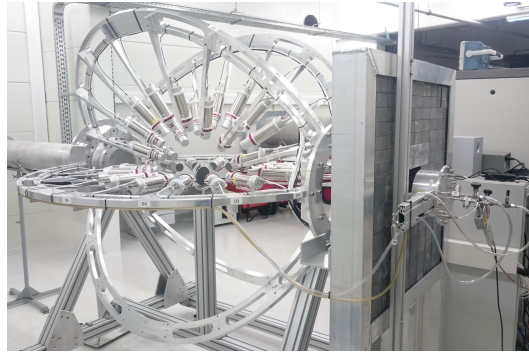
(a) Picture of the setup installed in the measurement station at 108°, 30 m distance from the GELINA neutron source. The neutron beam comes from the right; it first passes through the fission chamber, then hits the target at the centre of the scintillator array. The fission chamber is mounted on a lead wall which is the last collimator (at 25.8 m distance from the source) shown in figure 3.2.

(b) Picture of the setup installed in the nELBE measurement hall for the iron measurement. Here the beam comes from the left. In front of the beam exit the PTB fission chamber is seen. The JRC fission chamber is upstream, just behind it.
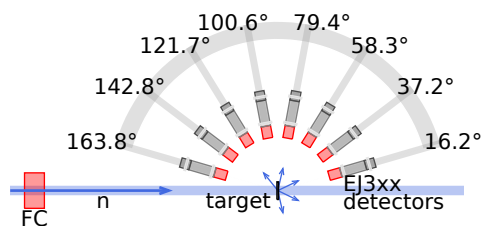
(c) Representation of one set of 8 scintillators (either EJ301 or EJ315 detectors); relative positions to the target and the fission chamber (FC).

Figure 3.4: Experimental setup for scattering cross section measurements.

Table 3.2: EJ301 and EJ315 composition and physical properties [47, 48].

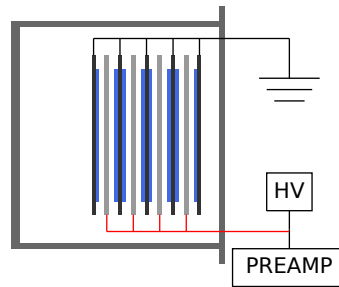|	EJ301	EJ315
Number of ^{1}H atoms per cm^3	4.82×10^{22}	0.0287×10^{22}
Number of ^{2}H atoms per cm^3	-	4.06×10^{22}
Number of C atoms per cm^3	3.98×10^{22}	4.10×10^{22}
Density at 25°C (g/cm^3)	0.874	0.954
Scintillation liquid volume (cm^3)	105.9	105.9
Scintillation efficiency (photons/1 MeV electrons)	12000	9200
Wavelength of maximum emission (nm)	425	425

Figure 3.5: Schematic representation of the parallel plate ionization chamber. The aluminium foils (in black) supporting the UF$_4$ deposits (blue) are grounded, while a positive voltage is applied to the electrodes (grey). HV: high voltage supplier, PREAMP: charge-integrating preamplifier.

a liquid cell of 5.08 cm diameter and 5.08 cm height (see figures 3.11 for a schematic representation). The cells are not fully loaded with the scintillation liquid, but contain an expansion void bubble that accounts for 3% of the total cell volume. The aluminium housing has a thickness of 1.52 mm and is sealed with a quartz window, which provides optical coupling to a photomultiplier tube (PMT, Electron Tubes Ltd., model 9214). The PMT and its voltage divider are mounted in a μ-metal housing of 0.64 mm thickness that shields them against the influence of external magnetic fields.

The light pulses emitted by the scintillation liquid and collected by the light guide (the quartz window) are converted to electrons (the so-called photoelectrons) by the photocathode of the PMT. The photoelectrons are accelerated towards the PMT dynodes where they are multiplied in a cascade process by secondary electron emission. The voltage supplied to the dynode chain through the voltage divider has to be optimized in order to maximize the multiplication process, but maintaining it linear. This optimization ensures that the charge pulses collected at the anode of the PMT are proportional to the light output of the scintillator.

3.2.2 Fission chamber

The ^{235}U fission chamber is a parallel-plate ionization chamber containing eight UF$_4$ deposits arranged on three double-sided and two single-sided aluminium foils. The aluminium backings have a diameter of 84 mm and are 20 μm thick. The UF$_4$ deposits were manufactured by vacuum evaporation, and have a 70 mm diameter. The uranium content of each deposit is reported in table 3.4; it corresponds to a total ^{235}U areal density of

Table 3.3: Isotopic composition of the UF$_4$ powder.

U-isotope	Atom %
^{233}U	< 0.001
^{234}U	0.036
^{235}U	99.94
^{236}U	0.011
^{238}U	0.013

Table 3.4: Uranium areal density of the UF$_4$ deposits contained in the fission chamber. The uranium content was determined by alpha counting, the UF$_4$ content was determined from the 1:4 molar ratio between uranium and fluorine, and ^{235}U content was calculated using the isotopic composition reported in table 3.3

Target	μg U/cm^2	μg UF$_4$/cm^2	μg ^{235}U/cm^2
Target 1	622(1)	823(2)	622(1)
Target 2 side 1	488(1)	646(2)	488(1)
Target 2 side 2	464(1)	614(2)	463(1)
Target 3 side 1	489(1)	647(2)	488(1)
Target 3 side 2	459(2)	607(2)	458(1)
Target 4 side 1	487(1)	645(2)	487(1)
Target 4 side 2	461(1)	610(2)	461(1)
Target 5	628(1)	831(2)	628(1)

4.095(4) mg/cm^2. The total amount of uranium was determined by alpha counting; the amount of ^{235}U was deduced using the isotopic composition reported in table 3.3. The deposits are mounted in the chamber at 14 mm distance one to the other; the two single-sided foils are staying at the two ends with the UF$_4$ deposit facing inwards (see scheme in figure 3.5). Aluminium electrodes of 25 μm thickness are placed between the deposits, equally spaced, at a distance of 7 mm from the two closest deposits. The foils supporting the deposits are grounded, while a positive voltage is applied to the electrodes. The entrance window of the aluminium housing is 0.3 mm thick, the exit window is 0.2 mm thick. The chamber is filled with P10 gas (10% methane, 90% argon) at atmospheric pressure. A small flow rate is supplied to continuously refresh the counter gas, granting stable operation.

3.3 Data acquisition system

3.3.1 Measurements at GELINA

For the measurements at GELINA, a dedicated digitizer-based acquisition system was developed to collect the signals produced by the 32 scintillators (electronics diagram in figure 3.6a). The data acquisition (DAQ) system consists of eight digitizer cards with four input channels each, 14 bit resolution and 500 MS/s sampling rate (SPDevices, model: ADQ14DC-4A-VG-PXIe). The cards are installed in a PXIe chassis (ADLINK PXES-2780) and managed by a controller that runs the Red Hat Enterprise Linux 6.4 operating system. A clock generator (Stanford Research Systems Inc. CG635) provides an external 10 MHz reference for the synchronization of the digitizer clocks. The input channels are connected to the scintillator photomultiplier anode output. Each channel triggers independently from the others when the (negative) signal goes below a given threshold, typically set between -5 mV and -10 mV. The linac reference signal (the "T0 signal") is connected to the digitizer as external "sync" signal and resets the time counter for every GELINA electron burst: the detector signal timestamps are therefore directly proportional to the particle time-of-flight. The T0 signal arrives at the digitizers later than the signals relative to the detection of the bremsstrahl-
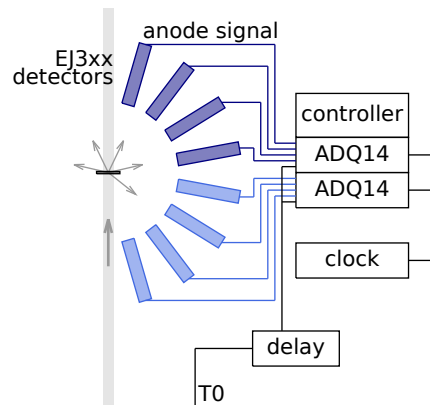
(a) DAQ diagram for one set of 8 scintillation detectors. The full DAQ system consists of 8 ADQ14 digitizer cards: they are all installed on the same PXIe chassis, managed by the same controller PC and the synchronization is performed using one clock generator for all cards.
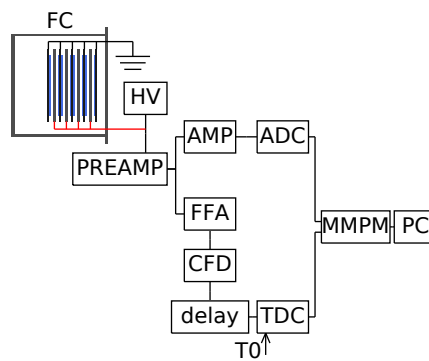
(b) DAQ for the fission chamber (FC). HV: high voltage supplier, PREAMP: charge-integrating preamplifier, AMP: spectroscopy amplifier, ADC: analogue-to-digital converter, FFA: fast filter amplifier, CFD: constant fraction discriminator, TDC: time-to-digital converter, MMPM: multiplexer.

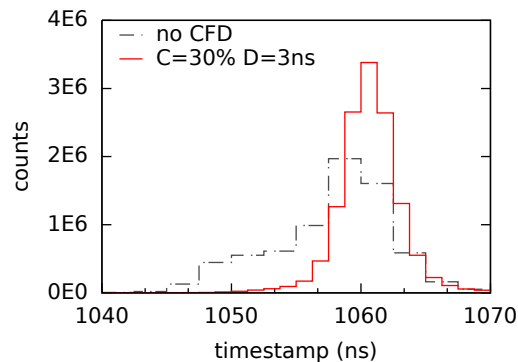Figure 3.6: Diagram of the DAQ system developed at GELINA.

Figure 3.7: Effect of the CFD algorithm on the resolution of the bremsstrahlung arrival time. The photons leave the target at the same instant (within 1 ns, the electron pulse width), and all travel at the same speed, therefore a single time value (with a resolution of 1 ns) is expected. The loss in resolution can be contained by applying the Constant Fraction Discriminator (CFD) algorithm. The signals are, on one side, inverted and delayed by a delay D = 3 ns, on the other side, attenuated by a constant fraction C = 30%. The two components are summed together, and the zero-crossing point of the resulting waveforms is used to correct the timestamps.

ung, but before the end of the neutron burst. To cope with that, a digital delay generator (Stanford Research Systems Inc. DG535) is used to make sure that it arrives later also than the neutrons. Therefore, the time reference for the t.o.f. measurement is given, in practice, at the end of each neutron burst.

Every waveform produced by the scintillators and the respective timestamps are saved to disk for offline processing. The processing includes the determination of the pulse height, the total integrated charge, the correction of the timestamp, and the pulse shape analysis. The correction of the timestamp (a leading edge trigger) is to improve the time resolution; this is achieved by analysing the waveforms applying the Constant Fraction Discriminator (CFD) algorithm [56, 57]. The timestamp given by the digitizer internal trigger is corrected by the offset to the zero-crossing point of the signal obtained using the attenuation-subtraction method, determined by linear interpolation between the two consecutive samples just above and below zero. The effects of the correction are shown in figure 3.7: the full-width-half maximum of the γ-flash time distribution is reduced from 10 ns to 5 ns. For the pulse shape analysis, the well-established charge integration method [58] is applied, according to which the Pulse Shape Discrimination (PSD) factor is defined as the ratio between the integral of the tail to the total integral of the signal waveform.

The DAQ system of the fission chamber consists of conventional front-end electronics (figure 3.6b). The fission chamber output is first fed to a charge-integrating preamplifier (CSTA2HV from the Technische Universität Darmstadt), and then it is split in two. It is given to a spectroscopy amplifier (Ortec 671) and to an Analogue-to-Digital Converter (ADC, FAST ComTec 7072), and, in parallel, to a fast filter amplifier (Ortec 579), a Constant Fraction Discriminator (CFD, Ortec 584) and a Time-to-Digital Converter (TDC, JRC in-house development). The TDC works like a stopwatch: the T0 signal starts the clock and the timestamp of the fission chamber signals is measured relative to it. Here the mismatch between the T0 and the fission chamber signals arrival times is handled by delaying (cable delay) the CFD signals to make sure the T0 signal arrives first at the TDC. A multiplexer (MMPM, JRC in-house development) controls the ADC and TDC, ensuring the coincidence between amplitude and time information, and redirects the data to the PC where they are stored in the form of list files.

3.3.2 Measurements at nELBE

The data acquisition system at nELBE [45] is based on commercially available VME modules including ADCs (CAEN V556), QDCs (Charge-to-Digital Converter, CAEN V965A), CFDs (HZDR in-house development), and TDCs (CAEN V1290A). The modules are read out by a CES RIO4 VME Power-PC running the real time operating system LynxOS and the DAQ software MBS developed by GSI Darmstadt [59]. A FPGA module (CAEN V1495) acts as trigger logic module, producing the trigger for the QDCs and TDCs, and measuring the DAQ dead time due to the analogue-to-digital conversion and the read-out of the buffer memories. The dead time is measured integrally by the internal clock of the FPGA and per event by the trigger logic, using a VETO signal that is the logical OR of the busy signals of all electronic modules.

   For the scattering experiments, the scintillator signals were split and fed to two QDC channels for the charge integration over a long and a short interval, and to a CFD channel which was in turn connected to a TDC and the trigger logic module. The TDC gathered the signals from both the detectors and the accelerator reference signal, determining in this way the time-of-flight. For the fission chamber, the signal-processing chain was identical to that used at GELINA.

3.4 Characterization of the scintillation detectors

In liquid organic scintillators, the scintillation fluorescent light is observed when ionizing radiation interacts with the liquid causing transitions in the energy level structure of its molecules [49, 60]. Only part of the deposited energy is converted to light, the rest is dissipated primarily through heat. The fraction of energy converted into photons depends on the particle energy and on the stopping power of the scintillation material. The light output is linear in energy for electrons with energies above 40 keV [61]; for protons, deuterons, and heavy ions in general, the output is always less compared to electrons with the same kinetic energy, and the response is not linear with the energy.

   Neutrons and photons do not directly cause light emission; they induce it by transferring energy to the nuclei and the orbital electrons of the liquid molecules. The predominant interaction mechanism for photons is Compton scattering, while neutrons are mainly detected via elastic scattering on the hydrogen nuclei (protons or deuterons). The contribution of the carbon nuclei recoil is very limited because of the low energy and the strong quenching effects: the light production is low and the signals are typically below the detection threshold [62].

   The signals produced by the organic scintillators are characterised by a fast rise time, principally determined by the properties of the photomultiplier tube, and a tail consisting of fast and slow components. The fast component, the prompt fluorescence, represents the main contribution to the light emission and has a typical decay time of few nanoseconds. The slow components, the delayed fluorescence, decay in a few hundred nanoseconds [60, 62]. The ratio of the intensity of the slow to the fast component depends again on the stopping power: it is higher for particles that produce a higher ionization density in the liquid. This means that it is possible to discriminate between different particles that produce the same light output by analysing the shape of the pulses.

3.4.1 Pulse shape analysis

The discrimination between neutron-induced and photon-induced events implies discriminating between protons (or deuterons) and electrons. For events producing the same total light output, the difference between the signals induced by the two particle types lies in the fraction of light appearing in the slow component, that is, in the tail of pulse. To quantify it, several methods exists; the most common methods are almost equivalent in terms of neutron/photon separation performances [63].

(a) EJ301 detector.

(b) EJ315 detector.
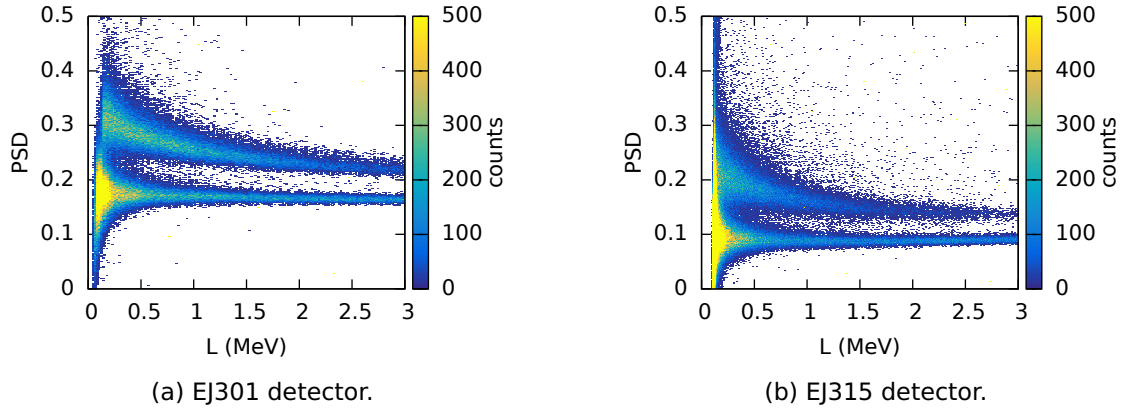
Figure 3.8: Two-dimensional histograms representing the PSD distribution as a function of the light output L. The data taken during a measurement with an AmBe source are shown for one of the EJ301 and one of the EJ315 detectors.

In this work, the well known charge integration method [58,62,64] was applied. According to this method, the scintillator signals have to be integrated over two different intervals: a long interval that includes the whole area of the pulse, and a short interval that starts where the long interval starts, but finishes early enough so that the tail is excluded. The Pulse Shape Discrimination (PSD) factor is defined as the ratio of the integral of tail to the total integral:

$$PSD = \frac{Q_L - Q_S}{Q_L} \qquad (3.1)$$

where Q_S and Q_L are the integral over the short and long interval, respectively.

The total integrated charge Q_L is directly proportional to the total light output produced in an event; the PSD factor is a measurement of the contribution of the slow component to the total light output. In figure 3.8, the data obtained during a measurement with an AmBe source are represented in a two-dimensional histogram with the PSD factor plotted against the light output (the definition of the light output units is given in the following section, equation (3.8)). The upper structure, with a higher tail-to-total ratio, corresponds to the neutron events; the lower structure corresponds to the photons.

The starting point of the Q_L and Q_S intervals were given by the starting point of the signal, i.e. by the CFD algorithm. The length of the long interval was set to 150 ns in order to make sure to include the whole tail of the waveforms, while the short interval was 30 ns long. This value was chosen to optimize the separation between neutron-induced and photon-induced signals, which was accomplished by maximizing the figure of merit (FOM) of the neutron/photon discrimination. The FOM is defined as:

$$FOM = \frac{M_n - M_\gamma}{FWHM_n + FWHM_\gamma} \qquad (3.2)$$

where M_n, M_γ represent the mode, while $FWHM_n$, $FWHM_\gamma$ the full-width half-maximum of the PSD distributions of neutrons (n) and photons (γ). The mode and the FWHM were computed assuming that the PSD follows the normal distribution. This assumption is in general valid if, instead of considering the whole light output range, the data are arranged in smaller intervals. In figure 3.9, for example, the distribution obtained by gating the two-dimensional histogram of figure 3.8 on the light output interval from 1.8 MeV to 2 MeV is shown. The sum of two Gaussian functions,corresponding to the contributions of photons and neutrons, is fitted to the experimental PSD distribution.

In figure 3.10, the FOM computed for several PSD distributions, obtained for the same data set considering different values for the length of the short integration interval, are shown for one EJ301 detector (3.10a) and one EJ315 detector (3.10b). The EJ315 detector
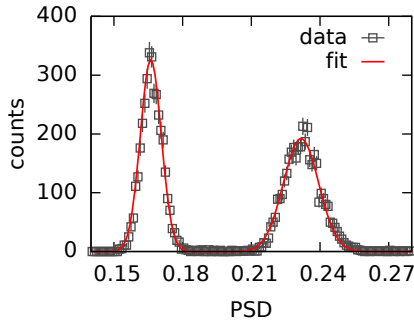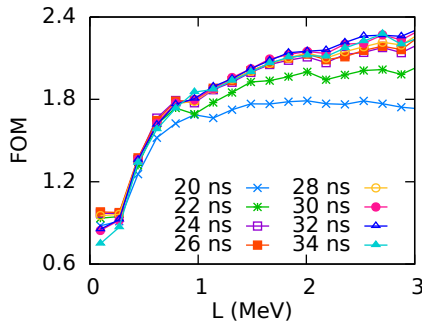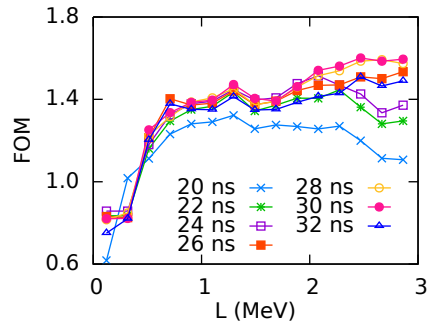
(a) Data from an EJ301 detector.
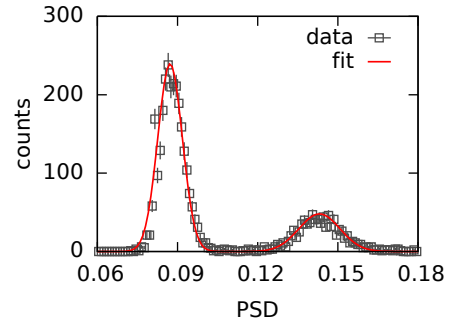
(b) Data from an EJ315 detector.

Figure 3.9: PSD distribution for the data lying in the light output interval from 1.8 MeV to 2 MeV: experimental histogram and result of the fit with the sum of two Gaussian functions.

(a) Data taken with an EJ301 detector.

(b) Data taken with an EJ315 detector.

Figure 3.10: Figure of merit of the PSD distributions obtained for the same data set using different short integration intervals (interval length as reported in the graphs), plotted as a function of the light output L.

exhibits slightly worse separation capabilities than the EJ301, but both of them perform well (the figure of merit is greater than one) in the light output range above 400 keV. The separation becomes problematic when the FOM becomes smaller than one: below 400 keV for the EJ315 detectors, and below 250 keV for EJ301 detectors. The best separation is obtained for the EJ301 detector when the short interval is from 30 ns to 32 ns long, for the EJ315 detector when it is 28 ns–32 ns long. The value of 30 ns was chosen because it was found to be suitable for the analysis of the waveforms of both detectors.

3.4.2 Detector response function

One of the reasons for choosing EJ301 and EJ315 scintillators was to use them as neutron spectrometers, to separate the elastic and inelastic components. Spectrometry is however possible only after a proper characterization of the detectors. To determine the detector response function, a combination of calibration measurements and Monte Carlo simulations was used to establish the light output functions for the detected secondary charged particles, the pulse height resolution function and the intrinsic detection efficiency.

The response function or response matrix $R(L, E_x)$ of a detector gives the probability for an incident neutron ($x = n$) or photon ($x = \gamma$) of energy E_x to produce a light output signal of intensity L. It depends on the probability for the particle to interact with the scintillation liquid, to transfer a given amount of energy $E_{x'}$ to the electrons ($x' = e$) or hydrogen nuclei ($x' = p$ for ^{1}H, or d for ^{2}H), and on the relationship between deposited energy and light output, i.e. the light output function $L' = L(E_{x'})$. It is also a function of the energy resolution of the detector, which depends, for example, on the statistical variations in the light

production and its transmission through the liquid, on the multiplication of photoelectrons in the photomultiplier tube, and on the noise of the dynode chain [65].

If the response function is known, the light output distribution $N(L)$ resulting from the irradiation with any incident energy spectrum $\Phi(E_x)$ can be predicted using:

$$N(L) = \int R(L, E_x)\, \Phi(E_x)\, dE_x \tag{3.3}$$

An important property of $R(L, E_x)$, is that it also allows to calculate the intrinsic detection efficiency $\varepsilon(E_x)$:

$$\varepsilon(E_x) = \int_{L_{thr}} R(L, E_x)\, dL \tag{3.4}$$

where L_{thr} is the detection threshold (which depends on the settings of the data acquisition system).

One way to determine $R(L, E_x)$ is to first compute the light output spectrum $N_{theor}(L', E_x)$ produced by the irradiation of the detector with monoenergetic neutrons or photons, in the theoretical case of infinitesimal resolution. Then, the broadening effect of the detector resolution has to be taken into account. This can be done by folding $N_{theor}(L', E_x)$ with the resolution function $r(L, L')$ [62, 65–67]. The response function thus is given by:

$$R(L, E_x) = \int r(L, L')\, N_{theor}(L', E_x)\, dL' \tag{3.5}$$

The resolution function $r(L, L')$ is defined as a Gaussian function with varying width:

$$r(L, L') = \frac{1}{\sqrt{2\pi}\sigma_{L'}}\, e^{-\frac{(L-L')^2}{2\sigma_{L'}^2}} \tag{3.6}$$

The variance $\sigma_{L'}^2$ is a function of the light output, and was parametrized with the empirical formula [68]:

$$\sigma_{L'}^2 = B_2^2 L'^2 + B_1^2 L' + B_0^2 \tag{3.7}$$

This parametrization represents an uncorrelated superposition of contributions due to the position-dependent variations in the light transmission to the photocathode of the photomultiplier tube (B_2), the statistical variations in the photon emission or the production of photoelectrons and secondary electrons (B_1), the noise of the electronic system (B_0).

In this work, the theoretical spectrum $N_{theor}(L', E_x)$ was established using Monte Carlo simulations, modelling the detector and the Compton scattering or the n-p, n-d (n-C, etc) collisions happening inside the liquid cell, computing for each reaction the deposited energy $E_{x'}$ and consequently determining the light output $L(E_{x'})$ distribution. To do that, the light output functions for electrons $L(E_e)$, protons $L(E_p)$ and deuterons $L(E_d)$ had to be parametrized.

The electron light output can be taken as linear in the electron deposited energy for values above 40 keV [61]; therefore, the light output function can be generally written as:

$$L(E_e) = A_1(E_e + A_0) \tag{3.8}$$

The scaling parameter A_1 can be arbitrarily chosen; here it was set equal to 1, following the convention of measuring L in terms of equivalent electron energy deposition [65, 69, 70]. The offset $A_0 = -5\,\text{keV}$ is needed to take into account the non-linearity due to quenching effects for small values of E_e [68].

For the proton and deuteron light output functions, the modified version of the empirical expression of Kornilov et al. [66, 67] was adopted:

$$L(E_{x'}) = A_1 E_{x'} + \frac{A_2 E_{x'}^2}{E_{x'} + A_3} \tag{3.9}$$

where $E_{x'} = E_p$ or E_d is the recoil energy of the hydrogen nucleus. The parameters A_1, A_2 and A_3 are characteristic of each individual detector [70] and have to be determined experimentally.

Table 3.5: Material composition of the elements included in the Monte Carlo model for the simulation of the response of the EJ301 and EJ315 detectors. (PMT: photomultiplier tube)

Detector component	Material	Chemical composition
Housing	aluminium	Al
Scintillation liquid	EJ301	$H_{1.212}C_1$
	EJ315	C_6D_6, $^2H{:}^1H{=}141{:}1$
Optical window	quartz	SiO_2
PMT shield	μ-metal	80.0%weight Ni, 4.5%weight Mo, 15.5%weight Fe
PMT glass	borosilicate glass	83.34%mol SiO_2, 11.19%mol B_2O_3, 4.08%mol Na_2O, 1.33%mol Al_2O_3, 0.03%mol CaO, 0.04%mol K_2O
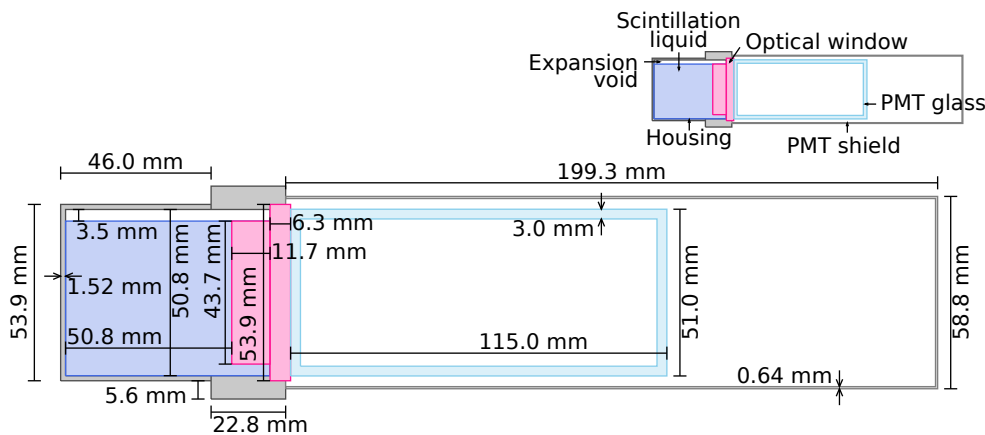
Figure 3.11: Diagram of the MCNP model: the vertical plane passing through the detector axis is shown.

3.4.3   Monte Carlo model of the scintillators

The simulations for the determination of the light output distribution N_{theor} were implemented in the Monte Carlo n-particle transport code MCNP5 [71]. The EJ301 and EJ315 detectors both have the same structure: the dimensions are given in the sketch in figure 3.11, where a scheme of the geometry implemented in MCNP is shown. In the model, the detector was placed horizontally in vacuum at 30 cm from the particle source. In the experimental setup, this is the distance from the detectors front face to the centre of the target holder. The material composition of the various detector elements is reported in table 3.5.

   The particle sources were defined as a monoenergetic sources of either photons or neutrons; the dimensions and the particle direction distributions were chosen to reproduce the experimental conditions. For the simulations of photon irradiation, the sources were modelled as isotropic, and had the same dimensions of the particular calibration source (γ-ray emitter) used during the actual measurements. The light output distributions reproduce the electron energy distributions except for the 5 keV offset. They can be obtained with MCNP by tallying the energy distribution of the pulses created in the liquid cell (tally "F8"). In figure 3.12, for example, Compton spectra obtained for a ^{137}Cs and a [207]Bi source are shown. It can be seen that there is virtually no difference between the EJ301 and the EJ315
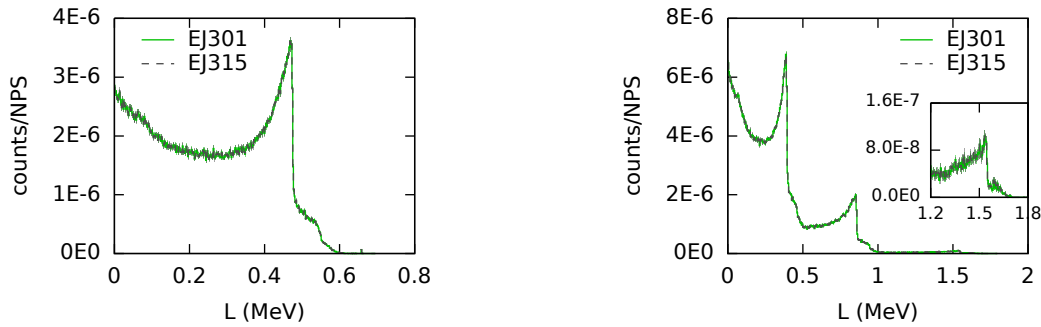
(a) Simulated Compton spectrum for a ^{137}Cs source (photon energy: 662 keV; Compton edge at 478 keV)

(b) Simulated Compton spectrum for a ^{207}Bi source (photon energies: 570 keV, 1064 keV, 1770 keV; Compton edges at 394 keV, 858 keV, 1547 keV)

Figure 3.12: Light output spectra simulated with MCNP for EJ301 and EJ315 detectors with infinitesimal resolution, using photon sources. The number of pulses generated per photon (counts per starting particle, NPS) is represented as a function of the electron light output.

detectors when it comes to photon spectrometry.

The neutron simulations were meant to replicate the neutron beam scattering on the sample. The source was therefore represented as a disk with the same diameter as the beam (4.9(2) cm at the sample position). The sources could have been modelled as isotropic, but to make the simulations more efficient, the neutron direction was uniformly sampled only in the solid angle covered by the detector. When considering the neutron interactions, the non-linearity of the light output function has to be taken into account. This means that when a neutron collides multiple times inside the detector, the light output cannot be determined by the total energy deposition, but the contribution of each collision has to be computed separately. In MCNP it is possible to use the "PTRAC" card to follow every neutron history event by event. This feature was used to select the collision events happening in the liquid cell volume. For each collision, the light output was determined applying equation (3.9), while the light output distribution was determined by summing together the contributions of events belonging to the same history. The spectra obtained for neutrons of 2 MeV energy are shown in figure 3.13. The elastic scattering recoil energy distribution is directly proportional to the angular distributions measured for the target nucleus in the centre-of-mass (CM) reference frame. The n-p scattering distribution is isotropic in the CM frame, and this leads to a flat pulse height response for the EJ301 detector. The n-d scattering is not isotropic, and in the EJ315 pulse height spectrum it is possible to recognize the backscattering peak corresponding to roughly 8/9 of the neutron energy.

3.4.4 Response to monoenergetic photons

The γ-ray emitters used for the calibration of the light output scale and their properties are reported in table 3.6. For each source, the simulated, resolution-folded detector response was fitted to the measured pulse-height spectra in correspondence with the Compton-edge position (see figure 3.14). The simulated spectra were computed by modelling a source with the same dimensions of the radionuclide sample used for the irradiation, producing γ-rays with intensity as reported in table 3.6. The fit of the resolution-folded detector response to the experimental data returned the parameters B_0, B_1, B_2 of the resolution function. It was also used to determine the calibration curve between the integrated charge Q_L and the light output L:

$$Q_L = F \cdot L + O \tag{3.10}$$

(a) EJ301 detector.   (b) EJ315 detector.
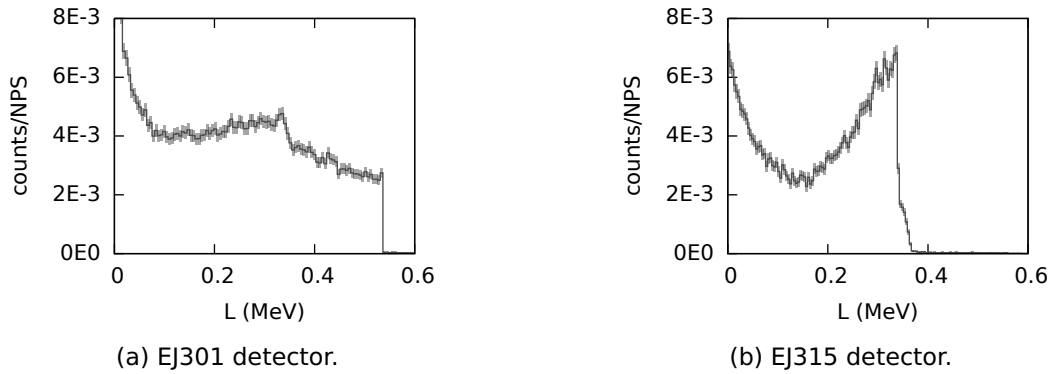
Figure 3.13: Light output spectra (counts per starting particle, NPS) simulated with MCNP for theoretical EJ301 and EJ315 detectors with infinitesimal resolution and for 2.0 MeV incident neutrons.

Table 3.6: γ-ray emitters used for calibration. A is the declared activity (if available), E_γ the energy of the observed γ-rays, and E_{CE} is the energy corresponding to the Compton edge. When more than one γ-line is considered for the same nuclide, the relative intensity I is also given.

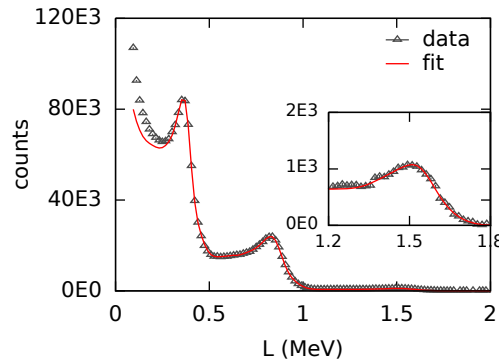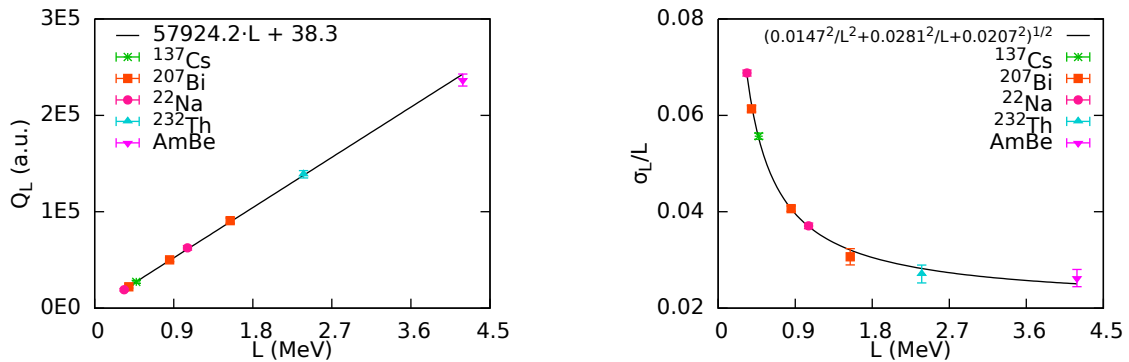| Source	$T_{1/2}$ (years)	A (kBq)	E_γ (keV)	E_{CE} (keV)	I (%)
^{137}Cs	30.08	395.2	662	478	
^{22}Na	2.6018	343.3	511	341	180.76
			1275	1062	99.94
^{207}Bi	31.55	387.4	570	394	97.75
			1064	858	74.50
			1770	1547	6.87
^{208}Th (from ^{232}Th)	1.40×10^{10}	N.A.	2615	2382	
AmBe	432.60	N.A.	4438	4196	

Figure 3.14: Experimental ("data") and modelled ("fit") spectra for the [207]Bi source, for an EJ301 detector.

(a) Calibration of the Q_L scale: position of the Compton edge (in equivalent electron energy deposition) plotted against the corresponding value of the integrated charge Q_L (arbitrary units).

(b) Relative resolution σ_L/L measured as a function of the light output L.

Figure 3.15: Characterization of the photon response of an EJ301 detector: position of the Compton edge (left) and resolution (right), measured for the photons produced by the radionuclides listed in table 3.6.

where F represents the conversion factor from photons to electrons and O the offset of the DAQ system.

Figure 3.15a shows the results of the calibration of one of the EJ301 detectors. The position of the Compton edges of the γ-rays produced by the sources listed in table 3.6 are plotted as a function of the electron light output. The final calibration curve for the given detector was obtained by fitting equation (3.10) to these points. Similarly, for the resolution function parameters, in figure 3.15b the values of the relative resolution σ_L/L, obtained at the Compton edge positions, are plotted against the light output. Here equation (3.7) is fitted to the data.

3.4.5 Response to monoenergetic neutrons

To determine the parameters of the light output functions of protons and deuterons, calibration measurements with (quasi-)monoenergetic neutron sources are necessary. For each neutron energy, the simulated detector response is fitted to the measured pulse height distribution to obtain, for the given energy, the corresponding light output. The values obtained from each single fit are then used for a global fit with equation (3.9), to determine the parameters that work best over the whole energy range.
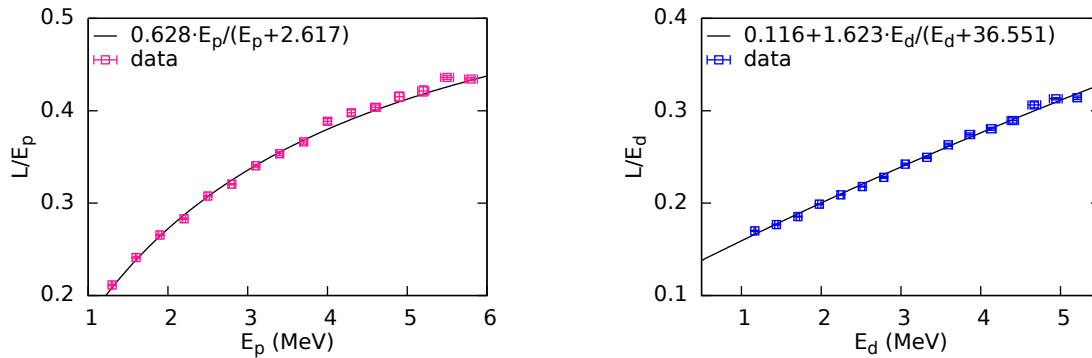
(a) EJ301 detector. The parameter A_1 of equation (3.9) is set to zero.

(b) EJ315 detector.

Figure 3.16: Ratio of the light output to the recoil energy as a function of the recoil energy of protons (E_p) and deuterons (E_d): experimental points ("data") and fit (solid line). The data points were taken using an EJ301 and an EJ315 detector. The neutron energy was determined using the t.o.f. method; E_p and E_d correspond to the maximum recoil energy a the given neutron energy.

One way to obtain quasi-monoenergetic neutrons in a t.o.f. experiment, is to select a short time interval, which corresponds to a narrow energy interval. For the light output determination, it was decided to use the data collected in a scattering experiment with a graphite sample. The threshold for inelastic scattering of carbon is at about 4.81 MeV of neutron incident energy (in the laboratory frame of reference). Therefore, below 4.8 MeV only elastic scattering occurs and there is a one-to-one correspondence between t.o.f. and neutron energy. Moreover, the separation between the ground state and the first excited level is such that it easily allows the separation of elastic and inelastic events via spectrometry.

The light output function was determined for each detector by selecting 16 t.o.f. intervals of 5 ns width corresponding to energies (incident energy on the detector, after the collision with carbon) from 1.3 MeV to 5.8 MeV. For each neutron energy E_n, the maximum recoil energy E_r^{MAX} of protons (for the EJ301 detectors) or deuterons (EJ315 detectors) was determined using the non-relativistic approximation:

$$E_r^{MAX} = \frac{4A}{(A+1)^2} E_n \tag{3.11}$$

where A is the ratio between the proton or the deuteron mass and the neutron mass. In figure 3.16 the light output measured as a function of the recoil energy is shown for one EJ301 detector and one EJ315 detector. Each point corresponds to an interval that includes energies that vary in the order of a few percents. The light output function parameters were determined by fitting equation (3.9) to the data points.

In figures 3.17 and 3.18, some examples of light output spectra obtained by selecting the events according to their t.o.f., are shown. These data were recorded at GELINA with four EJ301 detectors (figure 3.17) and four EJ315 detectors (figure 3.18) placed at four different angles: 163.8°, 121.7°, 58.3°, and 16.2° (see figure 3.4c). For each detector, three different t.o.f. intervals of 5 ns are displayed. If only elastic scattering on carbon is considered, these intervals correspond to roughly 2.19–2.22 MeV, 3.38–3.43 MeV, and 4.55–4.65 MeV of neutron energy at the detectors (energy after the collision). The corresponding incident energies on carbon (energy before the collision) depend on the scattering angle and therefore are different for each of the detectors; the exact values are reported below the figures. As the energy was determined from the elastic scattering kinematics, the incident energy represents a lower limit only. When inelastic scattering is considered, the same t.o.f. intervals correspond to higher energies. The data are compared with the results of
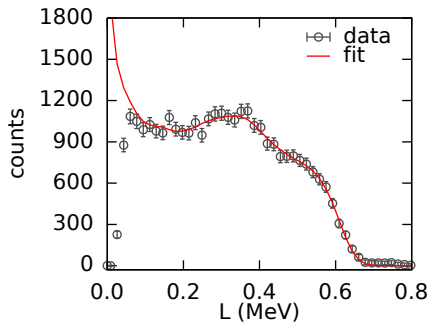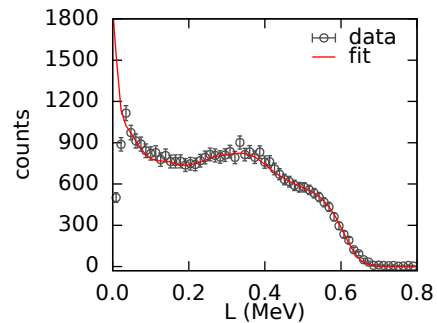
(a) Detector at 163.8°
- ❖ t.o.f. = 1131–1136 ns
- ❖ E_i = 3.06–3.09 MeV
- ❖ E_n = 2.20–2.22 MeV
- ❖ $E_{n,simul}$ = 2.2 MeV
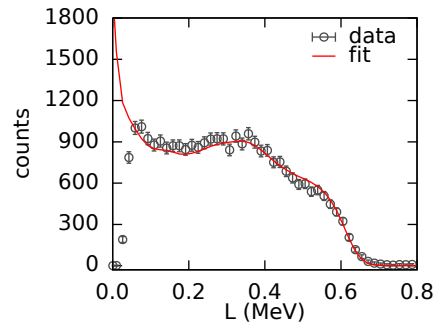
(b) Detector at 121.7°
- ❖ t.o.f. = 1175–1180 ns
- ❖ E_i = 2.83–2.85 MeV
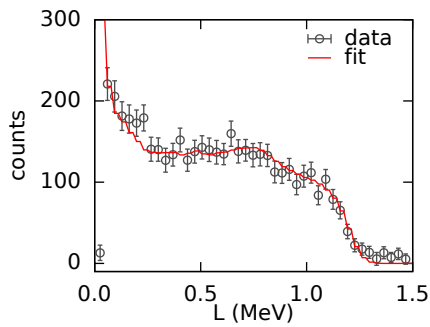- ❖ E_n = 2.19–2.21 MeV
- ❖ $E_{n,simul}$ = 2.2 MeV
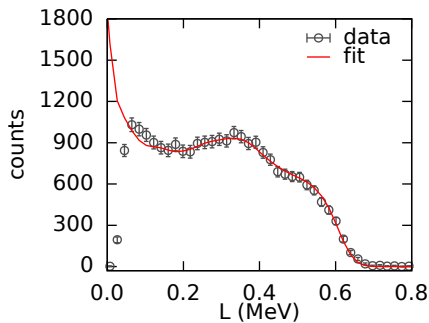
(c) Detector at 58.3°
- ❖ t.o.f. = 1284–1289 ns
- ❖ E_i = 2.37–2.39 MeV
- ❖ E_n = 2.19–2.20 MeV
- ❖ $E_{n,simul}$ = 2.2 MeV

(d) Detector at 16.2°
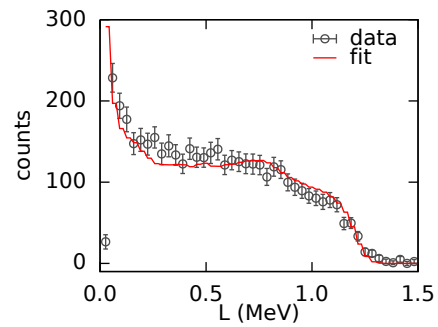- ❖ t.o.f. = 1328–1333 ns
- ❖ E_i = 2.21–2.23 MeV
- ❖ E_n = 2.19–2.21 MeV
- ❖ $E_{n,simul}$ = 2.2 MeV

Figure 3.17: Experimental light output histograms ("data") measured with EJ301 detectors at different angles, compared with the simulated detector responses ("fit"). The histograms represent the light output spectra obtained for neutrons in the t.o.f. intervals indicated below each figure. E_i and E_n are the neutron energy before and after the collision with carbon (elastically scattered neutrons). The detector response functions are modelled for monoenergetic neutrons with energy $E_{n,simul}$.
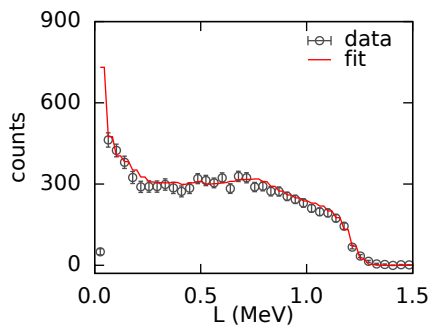
(e) Detector at 163.8°
   ❖ t.o.f. = 911–916 ns
   ❖ E_i = 4.72–4.77 MeV
   ❖ E_n = 3.39–3.43 MeV
   ❖ $E_{n,simul}$ = 3.4 MeV

(f) Detector at 121.7°
   ❖ t.o.f. = 946–951 ns
   ❖ E_i = 4.38–4.42 MeV
   ❖ E_n = 3.38–3.42 MeV
   ❖ $E_{n,simul}$ = 3.4 MeV

(g) Detector at 58.3°
   ❖ t.o.f. = 1029–1034 ns
   ❖ E_i = 3.68–3.72 MeV
   ❖ E_n = 3.40–3.43 MeV
   ❖ $E_{n,simul}$ = 3.4 MeV

(h) Detector at 16.2°
   ❖ t.o.f. = 1069–1074 ns
   ❖ E_i = 3.41–3.45 MeV
   ❖ E_n = 3.39–3.42 MeV
   ❖ $E_{n,simul}$ = 3.4 MeV

Figure 3.17: Continued from previous page.

(i) Detector at 163.8°
- ❖ t.o.f. = 786–791 ns
- ❖ E_i = 6.35–6.43 MeV
- ❖ E_n = 4.56–4.61 MeV
- ❖ $E_{n,simul}$ = 4.6 MeV

(j) Detector at 121.7°
- ❖ t.o.f. = 816–821 ns
- ❖ E_i = 5.89–5.96 MeV
- ❖ E_n = 4.55–4.60 MeV
- ❖ $E_{n,simul}$ = 4.6 MeV

(k) Detector at 58.3°
- ❖ t.o.f. = 890–895 ns
- ❖ E_i = 4.93–4.99 MeV
- ❖ E_n = 4.55–4.61 MeV
- ❖ $E_{n,simul}$ = 4.6 MeV

(l) Detector at 16.2°
- ❖ t.o.f. = 919–924 ns
- ❖ E_i = 4.62–4.67 MeV
- ❖ E_n = 4.59–4.64 MeV
- ❖ $E_{n,simul}$ = 4.6 MeV

Figure 3.17: Continued from previous page.

(a) Detector at 163.8°
  ❖ t.o.f. = 1131–1136 ns
  ❖ E_i = 3.06–3.09 MeV
  ❖ E_n = 2.20–2.22 MeV
  ❖ $E_{n,simul}$ = 2.2 MeV
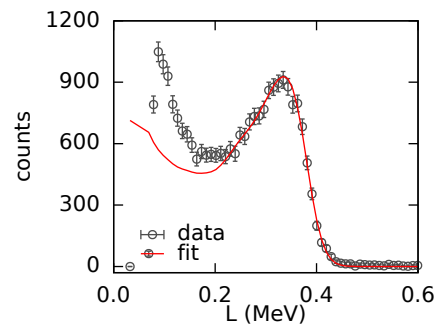
(b) Detector at 121.7°
  ❖ t.o.f. = 1175–1180 ns
  ❖ E_i = 2.83–2.85 MeV
  ❖ E_n = 2.19–2.21 MeV
  ❖ $E_{n,simul}$ = 2.2 MeV
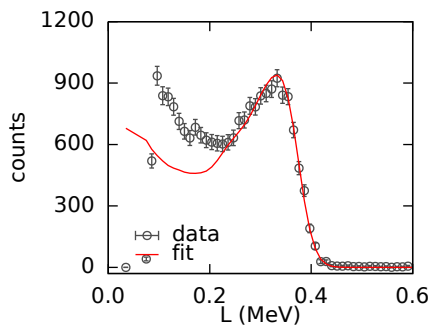
(c) Detector at 58.3°
  ❖ t.o.f. = 1284–1289 ns
  ❖ E_i = 2.37–2.39 MeV
  ❖ E_n = 2.19–2.20 MeV
  ❖ $E_{n,simul}$ = 2.2 MeV
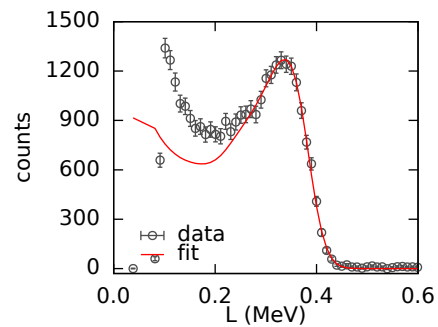
(d) Detector at 16.2°
  ❖ t.o.f. = 1328–1333 ns
  ❖ E_i = 2.21–2.23 MeV
  ❖ E_n = 2.19–2.21 MeV
  ❖ $E_{n,simul}$ = 2.2 MeV

Figure 3.18: Experimental light output histograms ("data") measured with EJ315 detector at different angles, compared with the simulated detector responses ("fit"). The meaning of the quantities reported below the figures is the same as for figure 3.17.

(e) Detector at 163.8°
- ❖ t.o.f. = 911–916 ns
- ❖ E_i = 4.72–4.77 MeV
- ❖ E_n = 3.39–3.43 MeV
- ❖ $E_{n,simul}$ = 3.4 MeV

(f) Detector at 121.7°
- ❖ t.o.f. = 946–951 ns
- ❖ E_i = 4.38–4.42 MeV
- ❖ E_n = 3.38–3.42 MeV
- ❖ $E_{n,simul}$ = 3.4 MeV

(g) Detector at 58.3°
- ❖ t.o.f. = 1029–1034 ns
- ❖ E_i = 3.68–3.72 MeV
- ❖ E_n = 3.40–3.43 MeV
- ❖ $E_{n,simul}$ = 3.4 MeV

(h) Detector at 16.2°
- ❖ t.o.f. = 1069–1074 ns
- ❖ E_i = 3.41–3.45 MeV
- ❖ E_n = 3.39–3.42 MeV
- ❖ $E_{n,simul}$ = 3.4 MeV

Figure 3.18: Continued from previous page.

(i) Detector at 163.8°
  ❖ t.o.f. = 786–791 ns
  ❖ E_i = 6.35–6.43 MeV
  ❖ E_n = 4.56–4.61 MeV
  ❖ $E_{n,simul}$ = 4.6 MeV

(j) Detector at 121.7°
  ❖ t.o.f. = 816–821 ns
  ❖ E_i = 5.89–5.96 MeV
  ❖ E_n = 4.55–4.60 MeV
  ❖ $E_{n,simul}$ = 4.6 MeV

(k) Detector at 58.3°
  ❖ t.o.f. = 890–895 ns
  ❖ E_i = 4.93–4.99 MeV
  ❖ E_n = 4.55–4.61 MeV
  ❖ $E_{n,simul}$ = 4.6 MeV

(l) Detector at 16.2°
  ❖ t.o.f. = 919–924 ns
  ❖ E_i = 4.62–4.67 MeV
  ❖ E_n = 4.59–4.64 MeV
  ❖ $E_{n,simul}$ = 4.6 MeV

Figure 3.18: Continued from previous page.

the simulations modelling the detector response to monoenergetic neutrons with 2.2 MeV, 3.4 MeV and 4.6 MeV energy. The interval around 2.2 MeV energy (figures 3.17a, 3.17b, 3.17c, and 3.17d for the EJ301 detectors; figures 3.18a, 3.18b, 3.18c, and 3.18d for the EJ315 detectors) and around 3.4 MeV (figures 3.17e, 3.17f, 3.17g, 3.17h and 3.18e, 3.18f, 3.18g, 3.18h) correspond to incident energies on the target that are below the carbon inelastic scattering threshold for all detectors. As inelastic scattering does not occur, the t.o.f. intervals correspond to quasi-monoenergetic neutrons, and the modelled detector responses should reproduce the experimental histograms over the whole light output range. That is indeed the case for the EJ301 detectors. For the EJ315 detectors, the model is consistent with the upper part of the spectrum but underestimates the number of counts for the low light output values. This inconsistency is possibly partially caused by the imperfect separation between neutrons and photons, which could produce a higher number of counts in the low part o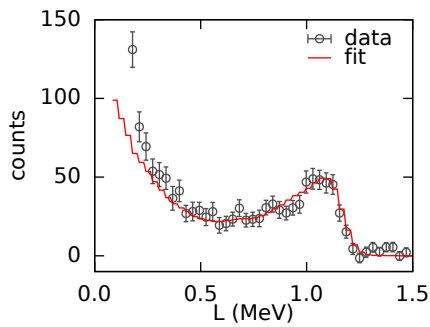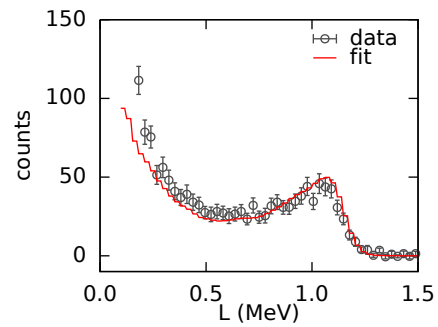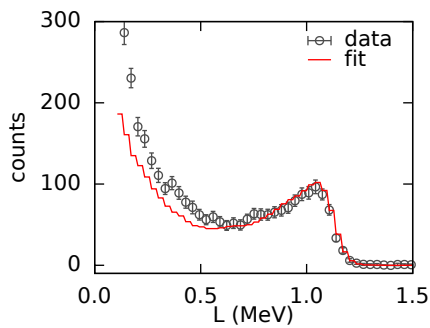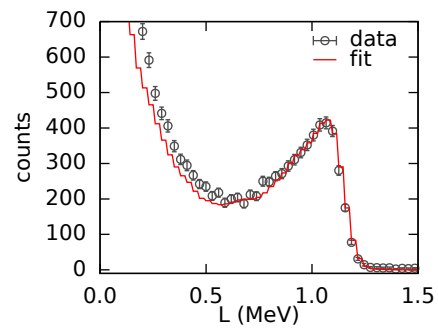f the spectrum. As the EJ315 detectors have worse pulse shape separation capabilities, it would be reasonable to suppose that the effects are more evident for them than for the EJ301 detectors. The difference however is not such that it could fully explain the discrepancy. As the shape of the spectrum depends on the angular distribution of neutron scattering on deuterium, another reason could be that the nuclear data libraries loaded in MCNP (ENDF/B-VII.1 in this particular case) do not properly report the backward-forward asymmetry of the reaction. The t.o.f. interval for the selection of the 4.6 MeV neutrons (figures 3.17i, 3.17j, 3.17k, 3.17l and 3.18i, 3.18j, 3.18k, 3.18l) corresponds to energies above the inelastic scattering threshold for all detectors, except the most forward one at 16.2°. For the two most backward detectors (163.8° and 121.7°), the inelastic events significantly contribute to the low part of experimental histograms of the backward detectors (below 500 keV). For the forward detector at 58.3°, if instead of the elastic scattering the inelastic scattering kinematics is considered, the t.o.f. interval corresponds to incident neutrons of 5.22–5.26 MeV energy and scattered neutrons of 0.43–0.48 MeV. The maximum light output is of about 50 keV, and therefore the inelastic scattering events lie below the detection threshold.

3.4.6 Intrinsic efficiency

Having determined the parameters of the detector response, it is possible to apply equation (3.4) to determine the detector's intrinsic efficiency. In figure 3.19, the efficiency is represented as a function of the neutron energy. The curves obtained for all 32 detectors are shown divided into sets of eight.

Even though the different parameters cause a bit of spread in the efficiency of the different detectors, the trend is still very similar for all of them. The efficiency reaches its maximum for neutrons with energies between 1 MeV and 2 MeV, it slowly decreases for higher energies, while below 1 MeV it quickly drops. It is higher for the EJ301 detectors (figures 3.19a and 3.19b), ranging from 20% to 30%–40% for neutrons above 1 MeV. For the EJ315 detectors (figures 3.19d and 3.19c), it goes from 15% to 25%.

3.5 Accuracy of the detector model

3.5.1 Comparison with NRESP

Two critical points of the scattering experiments are the efficiency and the separation of the elastic and inelastic contributions. The idea of deconvolving the spectrum to separate the two components on the basis of the neutron energy requires having a good handle on the detector response function, which ultimately depends on how well the Monte Carlo model of the detector performs. To validate the scintillator model based on the MCNP simulations and the analysis of the neutron histories, a comparison with the code NRESP [72] was implemented.

NRESP is a Monte Carlo code developed at the Physikalisch Technische Bundesanstalt (PTB) in Braunschweig (Germany) for the determination of the neutron response function of NE213 scintillators (EJ301 equivalents). This code considers only a very specific detector
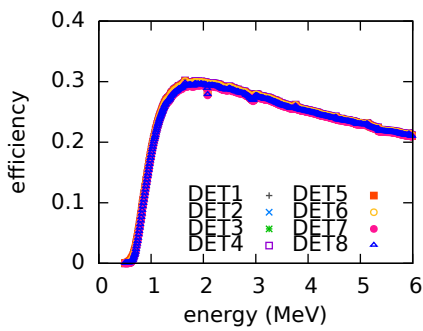
(a) EJ301 detectors.
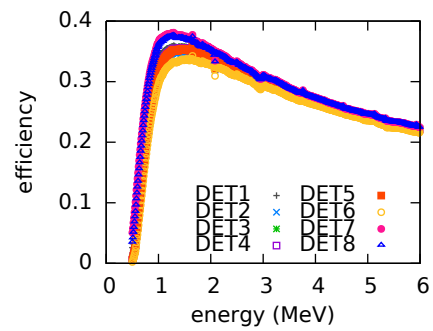
(b) EJ301 detectors.
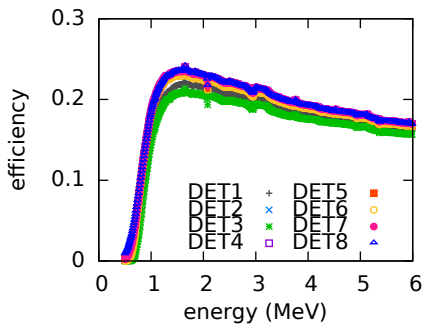
(c) EJ315 detectors.
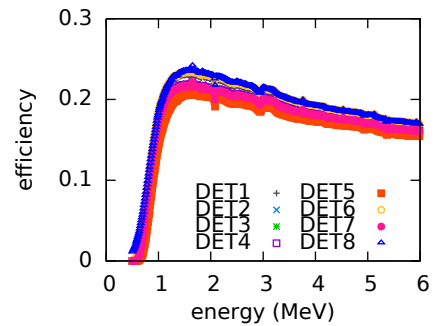
(d) EJ315 detectors.

Figure 3.19: Intrinsic efficiency of the scintillation detector as a function of the neutron energy. Every figure represents one set of 8 detectors; for each set, the numbers indicate the detector position (number 1 is the most backward scattering angle and number 8 the most forward).

geometry, which consists of a cylindrical liquid cell (of customizable dimensions), contained in an aluminium housing, coupled with a light guide of the same diameter and variable height. It does not foresee the possibility of an expansion bubble in the liquid cell. It already includes some predefined parametrization for the proton light output function, but it also gives the possibility to use a custom expression. In contrast to the analysis of the MCNP histories, NRESP takes into account the contribution of the carbon recoil to the light output, and provides an expression to quantify it. In the MCNP-based approach, the carbon light output is assumed to be negligible.

For the comparison, the same model was reproduced in both NRESP and MCNP: a NE213 cell of 5.08 cm diameter and 5.08 cm height, coupled with a light guide 1.8 cm high, contained in a 0.155 cm thick housing was placed at 30 cm distance from an isotropic point source. For the light output function, the parametrization expressed in equation (3.9) was again employed. The parameters were set to:

- ❖ $A_1 = 0$
- ❖ $A_2 = 0.616\,\mathrm{MeV}^{-2}$
- ❖ $A_3 = 2.51\,\mathrm{MeV}$

which are typical values found while characterising the EJ301 detectors response. The scintillator response was determined for monoenergetic neutrons of 1, 2, 3, 4, 5 and 6 MeV; the results are shown in figures from 3.20a to 3.20f. The light output distributions $dn/dL/n_{TOT}$ (number of pulses per light output per total number of neutrons incident on the detector) obtained with NRESP and the MCNP-based method are consistent, in the limit of the statistical uncertainties of the Monte Carlo simulations, for all investigated energies.

The detection efficiency (equation (3.4)) was determined as a function of the detection threshold, or in other words,

$$\varepsilon|_{THR=L} = \int_L (dn/dL'/n_{TOT})\, dL'$$

was determined as a function of the lower integration limit L. In figure 3.20, the ratio MCNP to NRESP is shown. Edge effects excluded, the difference between the two codes is always less than 2%. The MCNP model systematically underestimates the efficiency, but as the ratio to NRESP is (for a given neutron energy) almost constant over the whole light output range, the difference cannot be ascribed to lack of a method for the treatment of the carbon collisions in the MCNP history analysis. This comparison therefore justifies the assumption that the carbon light output is negligible. Also, it has to be noted that NRESP still takes the cross sections and angular distributions from the ENDF/B-IV evaluations, while for the MCNP calculation the more recent ENDF/B-VII was used. The discrepancies could be also an effect of using different cross section evaluations, especially since the typical difference is around 1%.
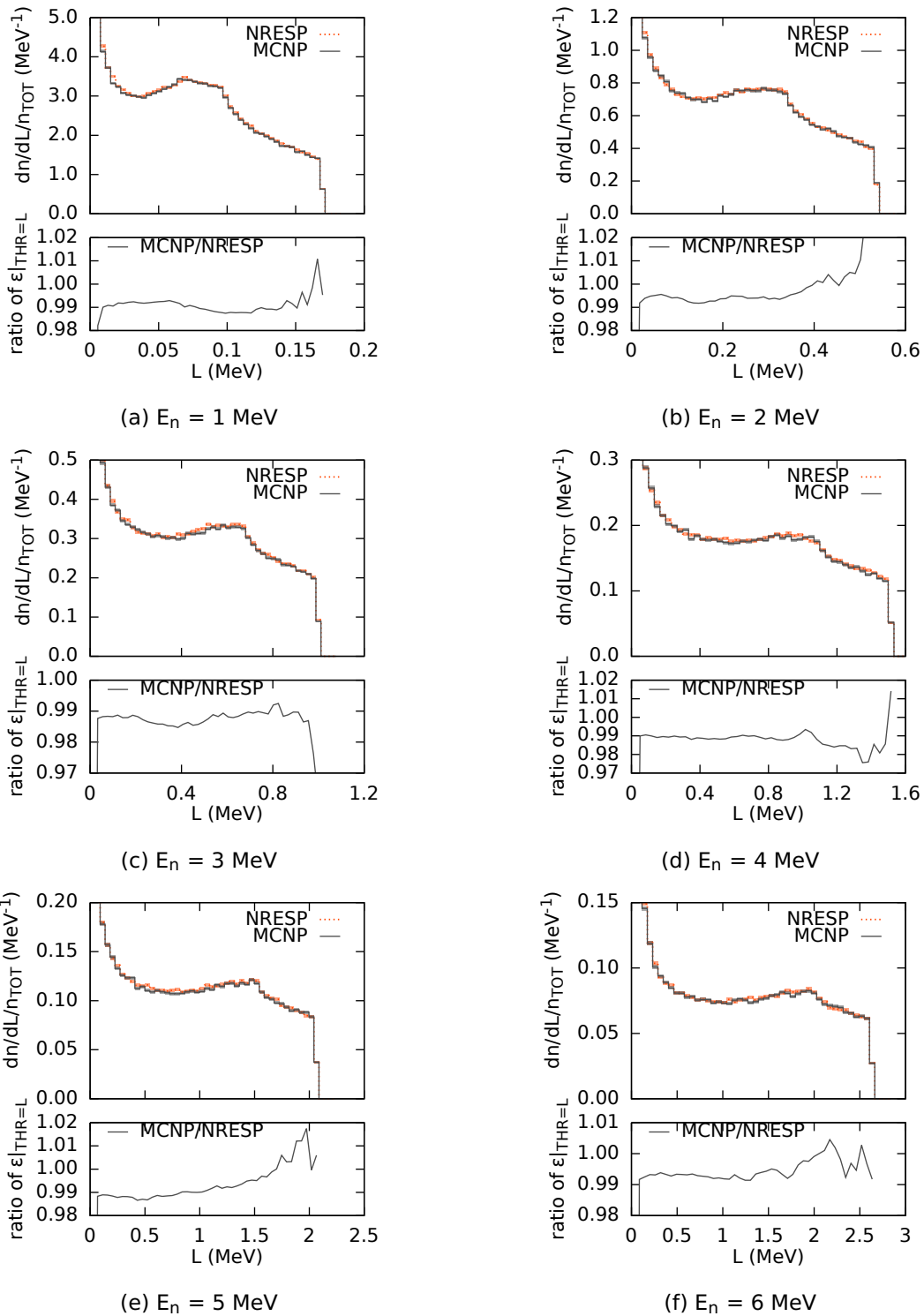
Figure 3.20: Comparison of the unbroadened response function of a NE213 detector computed with NRESP and with MCNP for different neutron energies (E_n as indicated below each plot). For each neutron energy, the detector response is represented as number of pulses per light output per total number of neutrons entering the detector ($dn/dL/n_{TOT}$). For both models, the efficiency was determined as a function of the threshold ($\varepsilon|_{THR=L}$); here the ratio of MCNP to NRESP is shown.

3.5.2 The detector orientation

For the sake of simplicity, in the MCNP model prepared for the light output parameter determination, the detector was laid horizontally. This arrangement makes it easier to define geometrically the section of the liquid cell occupied by the expansion void bubble. Moreover, half of the scintillators in the real experimental setup do actually lie horizontally. The other half is at 60° to the horizontal, facing downwards (see picture 3.4a). To investigate the effects of the detector orientation on its efficiency, three limit cases were investigated:

❖ the first case was the reference case, with the detector in horizontal (case labelled as "HO");

❖ for the second study case, the detector stood in vertical, facing downwards ("VD");

❖ the third detector was also put in vertical, but this time facing upwards ("VU").

For each of the three cases, the light output distribution and the efficiency as a function of the threshold were again determined for neutrons of 1, 2, 3, 4, 5 and 6 MeV energy.

In figure 3.21, the light output obtained for the three orientations and the ratio of detection energy of the vertical detectors (VU and VD) to the horizontal detector (HO) are shown. The efficiency of both vertical detectors is higher than the horizontal detector, because the entrance surface to the liquid is larger. In the VD detector, the liquid is closer to the centre of the frame or, in the simulations, closer to the neutron source; in the VU detector, the neutrons have first to cross the expansion bubble before they can reach the scintillation liquid. The geometrical efficiency is therefore higher for the detector facing downwards. The effects are a bit stronger for neutrons with lower energies, but nevertheless they are comparable with the statistical uncertainty of the Monte Carlo simulations, which is around 1%–2%.
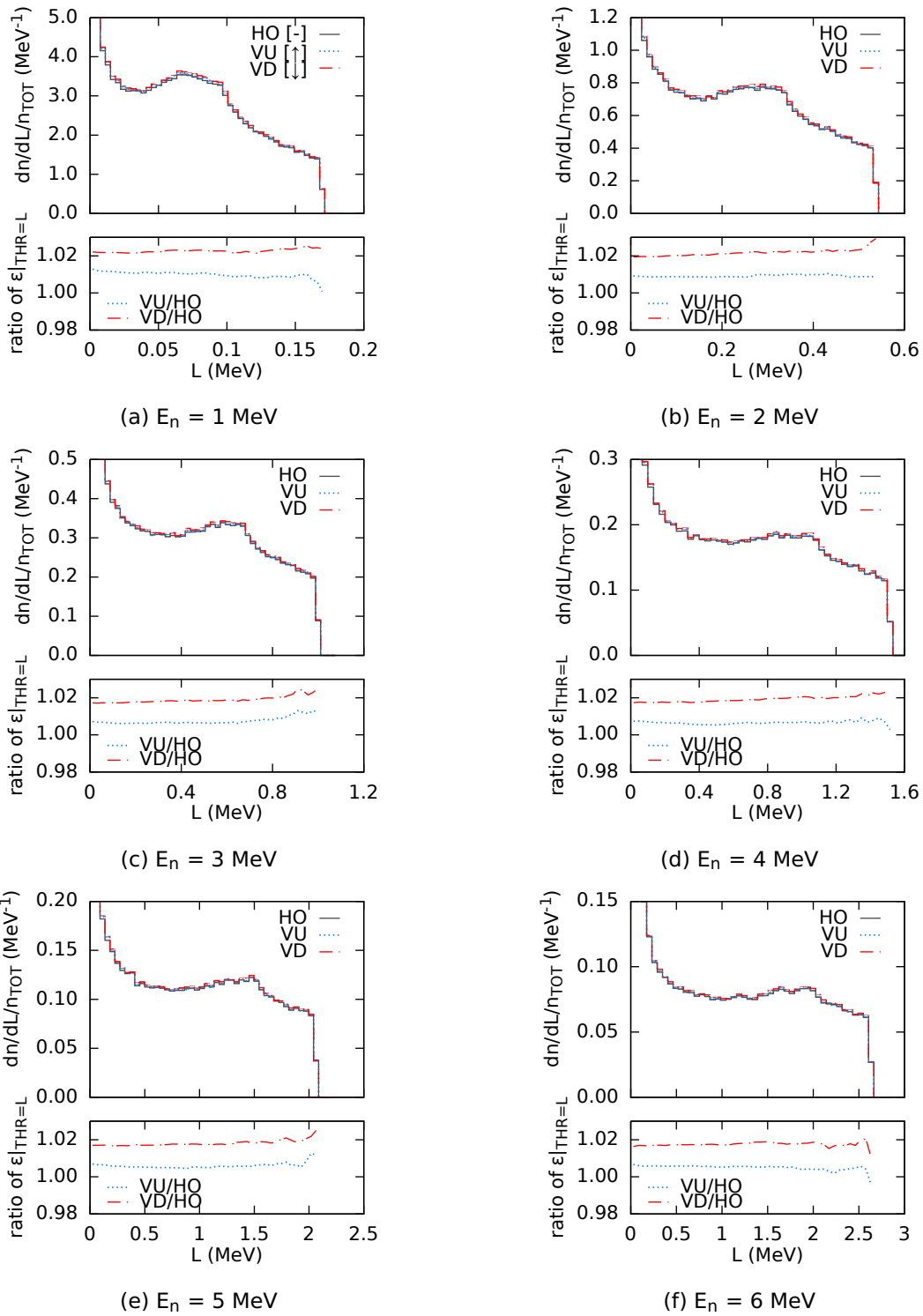
Figure 3.21: Differences in the EJ301 neutron response and efficiency caused by placing the detector in different orientations. "HO": detector in horizontal; "VU": detector in vertical, facing upwards; "VD": detector in vertical, facing downwards. The light output distributions per total number of neutrons entering the detector $dn/dL/n_{TOT}$ and the ratio of the efficiency as a function of the threshold $\varepsilon|_{THR=L}$ of the vertical detectors to the horizontal detector are shown.

Neutron scattering on carbon 4

The cross section of neutron elastic scattering on natural carbon is known with 1% or less total uncertainty up to 4.8 MeV. The differential cross section represents a neutron standard up to 2 MeV [31]. The angle-integrated cross section is characterised by two sharp resonances at 2078.05(32) keV and at 2816(4) keV, and the first of them is a recognized neutron energy standard [32]. For these reasons, the first experiment with the scintillator spectrometer was a measurement of neutron scattering on a graphite sample.

The measurement covers the neutron energy range from 1 MeV to 8 MeV. The energy spectrum of the neutron source (GELINA) is actually broader and reaches energies above 20 MeV. In practice, the neutron flux drops above 8 MeV and this limits the obtainable statistics. The lower limit is set at 1 MeV because of the detector efficiency (see figure 3.19).

Table 4.1 lists the already available n-C elastic scattering measurements in the neutron energy range from 1 MeV to 8 MeV. Up to 4.8 MeV, the elastic scattering cross section coincides with the total neutron cross section, so the results here presented could have been compared with both elastic scattering and total neutron cross section measurements. However, only experiments clearly targeted at elastic scattering are considered.

4.1 Experimental details

The measurement of the differential cross section of n-C scattering was carried out at GELINA, at the flight path at 108˚ from the electron beam direction. The neutron flight path measured from the source to the scattering target centre was 27.037(5) m; from the source to the fission chamber it was 25.667(5) m. The experiment lasted two weeks (ten days of beam time), during which GELINA was operated at a repetition rate of 800 Hz.

The scattering target was a graphite disk made of natural carbon with an areal density of 1.6606(3) g/cm^2, 10 cm diameter and 1 cm thickness (all properties are in table 4.2). The target was relatively thick, which means that the multiple-scattering correction played an important role in the data analysis. The diameter, much larger than the diameter of the neutron beam (4.9(2) cm at the target position), ensured that the beam was completely intercepted. The UF$_4$ deposits in the fission chamber (the flux monitor) also fully intercepted the beam. Therefore, it was not necessary to worry about the homogeneity and size of the beam, but only that of the target, which were excellent.

The measurements with the carbon sample were accompanied with "sample-out" measurements, during which the sample was removed from the neutron beam. This established the background due to neutrons and photons scattering in air or on surrounding materials.

4.2 Data analysis

4.2.1 Incoming neutron flux

The neutron flux incident on the carbon target was determined by the analysis of the fission chamber data, utilizing the standard ^{235}U(n,f) cross section to correlate the fission fragment counts with the number of incident neutrons. In figure 4.1, a pulse-height histogram of the

Table 4.1: From the EXFOR database: measurements of the reaction cross section ("CS") and of the differential cross section with respect to the angle ("DA") of neutron elastic scattering on ^{nat}C, covering the incident neutron energy from 1 MeV to 8 MeV. For each experiment, referred with the name of the first author and the year of publication, the incident neutron energy range and the number of points ("N.Points") are indicated.

Reference		Energy (MeV)	Quantity (N.Points)	
Barschall (1947)	[73]	2.8	CS (1)	
Bostrom (1959)	[74]	4.21–7.58	CS (3)	DA (35)
Galati (1972)	[75]	3.03–6.94		DA (476)
Haddad (1959)	[76]	6–7	CS (3)	
Hosoe (1959)	[77]	2.85–3		DA (56)
Knox (1973)	[78]	2.63	CS (1)	DA (8)
Lane (1961)	[79]	1.958–2.242		DA (256)
Lane (1969)	[80]	0.55–2	CS (39)	DA (133)
Langsdorf (1957)	[81]	0.06–1.782	CS (34)	
Little (1955)	[82]	2.7		DA (9)
Perey (1969)	[83]	4.6–8.56	CS (13)	DA (265)
Perey (1978)	[84]	5.22–8.69	CS (40)	DA (670)
Smith (1979)	[85]	1.502–3.99	CS (31)	DA (438)
Walt (1955)	[86]	4.1	CS (1)	DA (8)
Willard (1955)	[87]	0.55–1.5	CS (3)	
Wills (1958)	[88]	1.45–4.1		DA (107)

Table 4.2: Physical and chemical properties of the graphite sample. The isotopic composition of ^{nat}C comes from [89] and is in atom percent; the atomic mass comes from [90]. The dimensions and the mass of the sample were measured at the JRC-Geel.

^{nat}C composition	^{12}C: 98.94(10)%
	^{13}C: 1.06(10)%
Atomic mass	12.01(1) g/mol
Diameter	10.00(1) cm
Thickness	0.99(1) cm
Mass	130.424(5) g
Areal density	1.661(3) g/cm^2
	0.0832(2) atoms/b

events recorded with the ^{235}U fission chamber during a "sample-in" measurement (about 48 h of irradiation) is shown. The peak at low amplitudes is produced by α-particles from the uranium decay, while the fission fragments form the structure at higher amplitudes. The fission fragment and α-particle peaks are separated by a flat area, the so-called "plateau".

The α-particle events were rejected by applying a threshold on the pulse-height histogram corresponding to the middle point of the plateau, and the fission chamber yield above the threshold $Y_{FC}(E)$ was determined as a function of neutron energy. The neutron fluence $\Phi(E)$ was then determined by:

$$\Phi(E) = \frac{Y_{FC}(E)}{\varepsilon_{FC}\,\sigma_{235U(n,f)}\,\rho_{235U}\,A_b} \tag{4.1}$$

where $\sigma_{235U(n,f)}$ is the neutron-induced fission cross section, ρ_{235U} is the ^{235}U areal density in atoms per unit surface, and A_b is the cross-sectional area of the neutron beam. ε_{FC} is the fission chamber efficiency, and it is defined as [91, 92]:

$$\varepsilon_{FC} = \frac{Y_{FC}}{Y_{FC} + Y_A + Y_B} \tag{4.2}$$
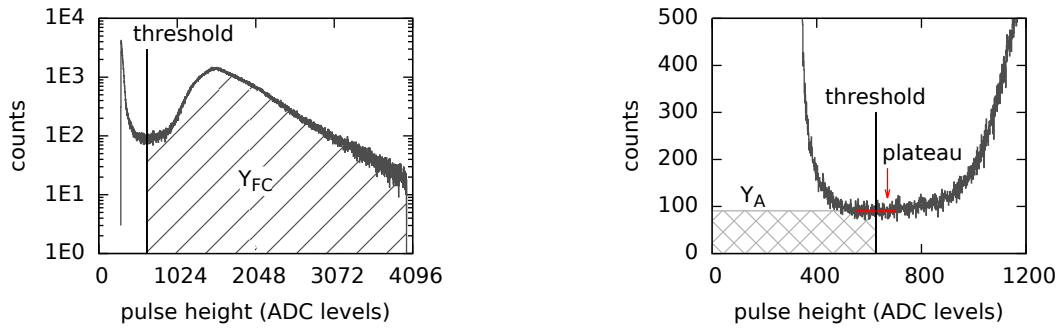
(a) Full pulse height histogram, threshold for the rejection of the α-particle events and fission fragments above threshold Y_{FC}.

(b) Plateau separating the fission fragments from the α-particles, and extrapolation of the events below threshold Y_A.

Figure 4.1: ^{235}U fission chamber pulse height histograms. These data were taken during the experiment with the graphite target for a duration of 47.8 hours.
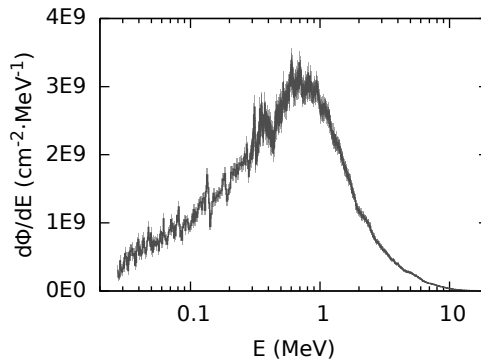
Figure 4.2: Neutron fluence energy distribution $d\Phi/dE$ incident on the carbon sample as function the neutron energy E (47.8 h measurement).

where Y_{FC} is the total number of fission fragments above the threshold (see figure 4.1a), Y_A (figure 4.1b) is the number of fragments below the threshold, and Y_B are the fragments emitted in the direction of the counter gas but stopped in the deposit.

The number of fragments below threshold Y_A was determined making a linear fit of the counts in the plateau region around the threshold, extrapolating to zero amplitude and evaluating the area underneath. The number of fragments stopped in the UF$_4$ deposits Y_B was determined by introducing a correction factor F_{YB}: $Y_{FC} + Y_A + Y_B = (Y_{FC} + Y_A)/F_{YB}$. The correction factor $F_{YB} = 1 - \Delta_{UF4}$ was found experimentally for evaporated UF$_4$ deposits from the inefficiency of the 2π counting in [93]. It amounts to $\Delta_{UF4} = 0.105(7) \times t_{UF4}$, where t_{UF4} is the thickness of the UF$_4$ layers in mg/cm^2. Considering the areal densities reported in table 3.4, the correction factors have an average value of $\Delta_{UF4} = 0.072(10)$ and $F_{YB} = 0.929(10)$. The uncertainties on Δ_{UF4} and F_{YB} were estimated from the distribution around the mean of the values obtained for the single deposits. The fission chamber efficiency was computed separately for the sample-in and sample-out measurements. As expected, in both cases the result was the same: the sample-in data gave $\varepsilon_{FC} = 0.890(10)$, while the sample-out data gave $\varepsilon_{FC} = 0.891(10)$.

In figure 4.2, the neutron fluence energy distribution incident on the graphite target during the 48 h measurement is shown. Integrating the distribution over the energy interval from 25 keV to 20 MeV and considering the measurement time, the fluence shown in figure 4.2 corresponds to a time-averaged neutron flux of $3.904(8) \times 10^4$ n/cm^2/s.

(a) EJ301 detector.   (b) EJ315 detector.
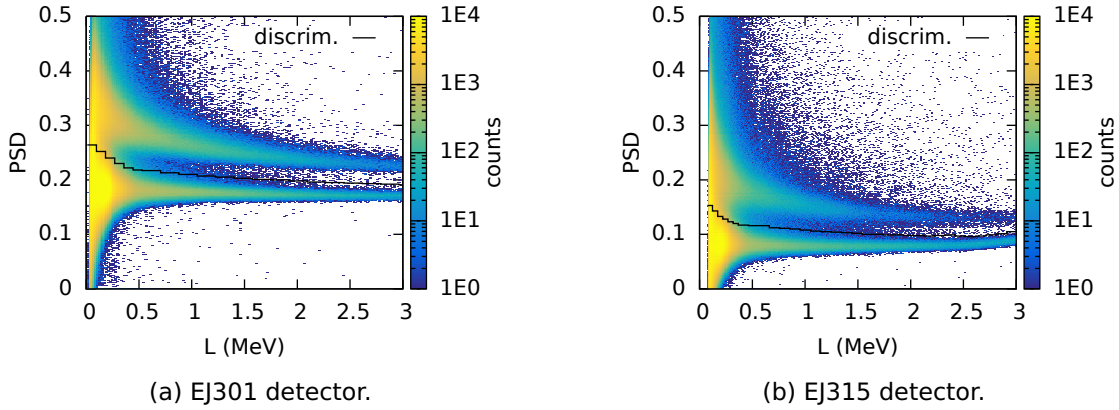
Figure 4.3: Two-dimensional histograms representing the events recorded by a EJ301 detector and an EJ315 detector arranged according the signal light output L (in equivalent electron energy) and the Pulse Shape Discrimination factor PSD. The segmented line ("discrim.") represents the "optimal" separation point between neutrons and photons found applying equation (4.3) in the light output interval subtended by each segment.

4.2.2   Neutron t.o.f. distribution

The scattered neutron events recorded by the scintillator array are mixed with photon-induced events from the bremsstrahlung scattering on the graphite target, or from neutron inelastic scattering or capture on the sample or the setup components. The separation between neutron-induced and photon-induced events can be accomplished through pulse shape analysis.

The two-dimensional histograms in figure 4.3 are the signals recorded by an EJ301 and an EJ315 detector classified according to their light output and PSD factor (defined in equation (3.1)). The photon and neutron events are separated by a line which represents the "optimal" PSD discrimination value. The separation was achieved slicing first the two dimensional histograms into smaller light output intervals. The resulting PSD distributions were fitted with the sum of two Gaussian functions ($g_\gamma(x)$ for photons and $g_n(x)$ for neutrons), and the optimal separation point PSD_{opt} was computed applying [64]:

$$PSD_{opt} = \underset{0 \leq x \leq 1}{\arg\min} \left\{ \int_x^1 g_\gamma(x)\,dx + \int_0^x g_n(x)\,dx \right\} \tag{4.3}$$

If x is the PSD factor that corresponds to the separation point between photons and neutrons, then $\int_x^1 g_\gamma(x)dx + \int_0^x g_n(x)dx$ represent the number of misclassified events. Choosing PSD_{opt} according to equation (4.3) means therefore minimizing the number of misclassified events per light output interval. The reliability of this method depends on the figure of merit of the PSD distribution (equation (3.2), and does not guarantee perfect neutron/photon separation, especially at low light output values.

The results of the separation based on the pulse shape analysis is shown in figure 4.4, where the t.o.f. distributions of the neutron events and photon events recorded during the sample-in measurement with the detectors in the most forward position (16.2°) are represented. The t.o.f. spectra are characterised by a sharp peak at 91 ns, which is the arrival time of the bremsstrahlung photons at the detectors; its presence in the neutron distribution is a consequence of an imperfect neutron/photon pulse shape discrimination. The broadening of the γ-flash peak is due to the electron pulse duration, the time evolution of the bremsstrahlung production process, and the time resolution of the detectors and the DAQ system. Its full-width half-maximum gives the lower limit for the time resolution in the given experimental conditions. At the given distance from the source, the time resolution of 5 ns in t.o.f. corresponds to 5 keV energy resolution at 1 MeV, 26 keV at 3 MeV, and 57 keV at 5 MeV. The structures in the neutron distribution in the t.o.f. interval from
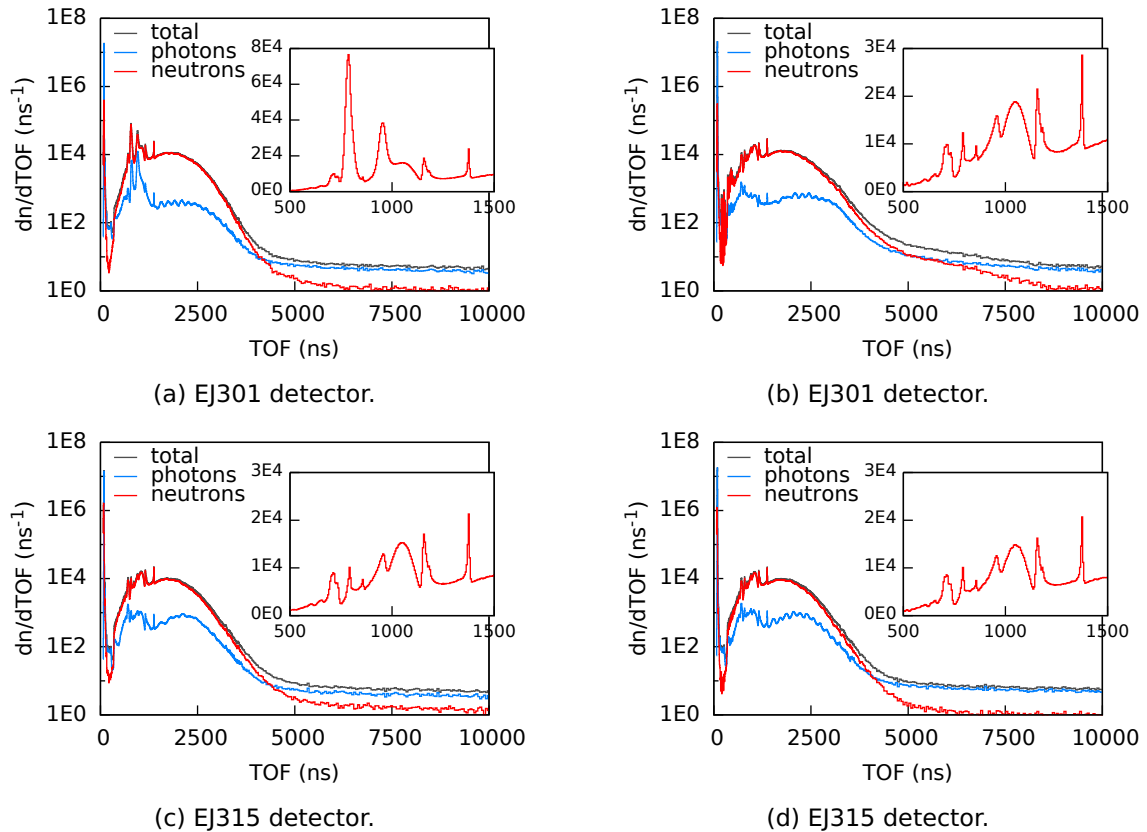
Figure 4.4: Time of flight distribution measured with the four scintillators at 16.2°. The neutron distribution, the photon distribution, and the sum of the two ("total") are represented. The insets show a linear representation of the neutron signals over a reduced time-of-flight range.

630 ns to 1500 ns (from ca. 10 MeV to 1.75 MeV in neutron energy) are the result of the neutrons interacting with carbon. In figure 4.4a, the structures at short t.o.f. are partially distorted by noise, probably signal overshoot from the photomultiplier tube. The peak at 1375 ns corresponds to the resonance in the carbon cross section at 2.078 MeV. The second resonance at 2.816 MeV, which should be found at 1181.5 ns, is not visible with the given time/energy resolution. In the same interval, the photon histograms present similar structures, but the photon counts are one to two orders of magnitude lower than the neutron's. The time-correlated photons can only be due to carbon above the inelastic threshold. The other photons are due to inelastic scattering on structural parts (e.g. detector housing, collimators, beam stop). The factor of 10–100 between photons and neutrons is an indication of a good experimental design. At long t.o.f., the flat photon background is a sum of the natural radioactivity background and the neutron capture reactions on the walls of the measurement cabin.

The neutron t.o.f. histograms are affected by two background components, one t.o.f dependent and the other independent. The t.o.f.-independent background consists of room return neutrons scattered from the walls, floor and ceiling of the measurement cabin, producing photons by capture reactions. the neutron contribution is almost negligible, but it can still be evaluated by averaging the number of counts per t.o.f. bin for times well beyond the end of the neutron burst (e.g., for t.o.f.>9000 ns). The t.o.f.-dependent background is due mostly to beam neutrons scattering on air once or twice before reaching the detectors, and it is determined during the sample-out measurement. To take into account the different incident neutron fluences during the two runs (which depend on the measurement time and the stability of GELINA), the sample-out data ("*out*") were rescaled to the sample-in data ("*in*") according to the ratio of the fission counts $\left(Y_{FC}^{in} \middle/ Y_{FC}^{out} \right)$ recorded with the ^{235}U chamber.
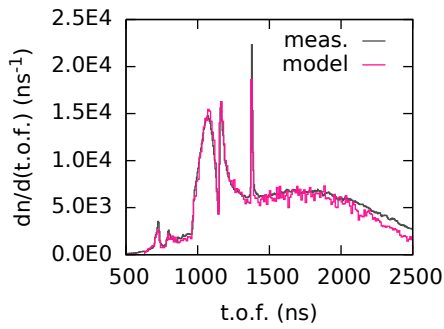
(a) Detector at 163.8°.
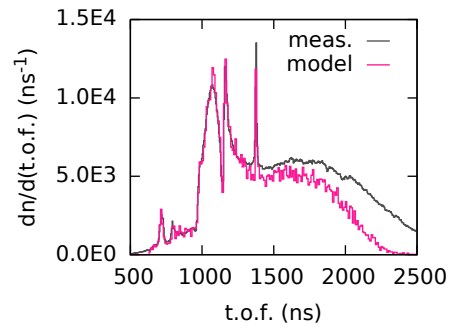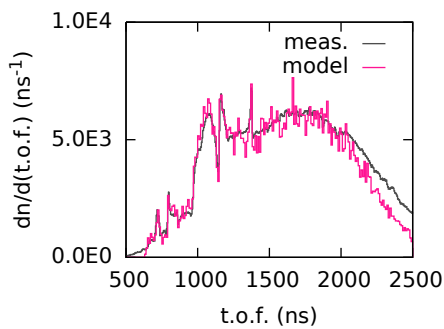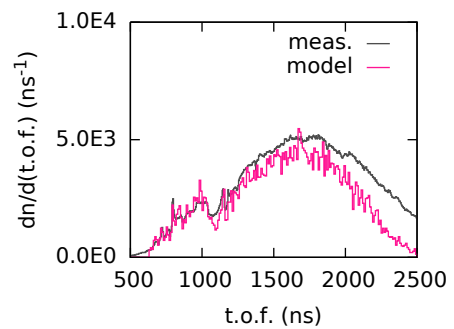
(b) Detector at 142.8°.

(c) Detector at 121.7°.
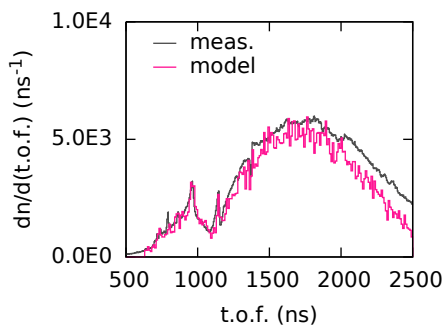
(d) Detector at 100.6°.
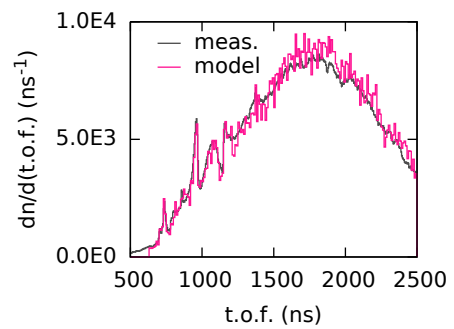
(e) Detector at 79.4°.
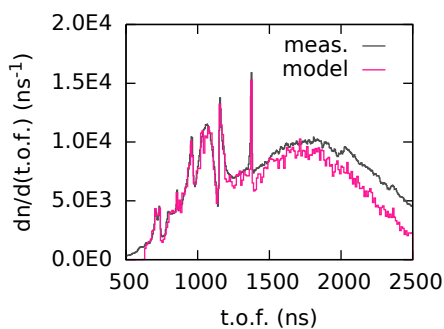
(f) Detector at 58.3°.
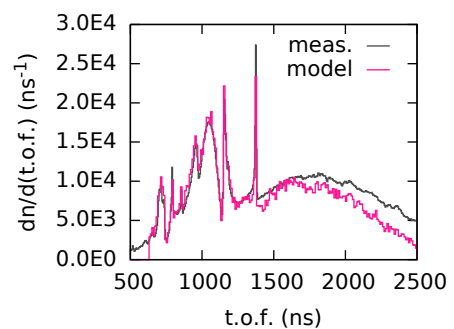
(g) Detector at 37.2°.

(h) Detector at 16.2°.

Figure 4.5: Comparison of the measured neutron t.o.f. distribution ("meas.") and results of the MCNP "full-setup" simulation ("model") for one set of EJ301 detectors.
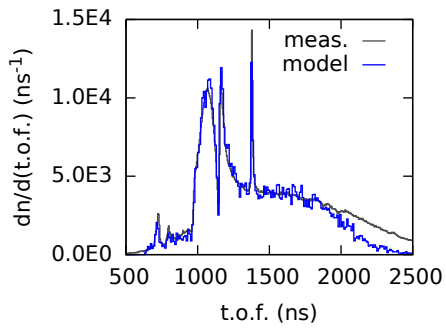
(a) Detector at 163.8°.
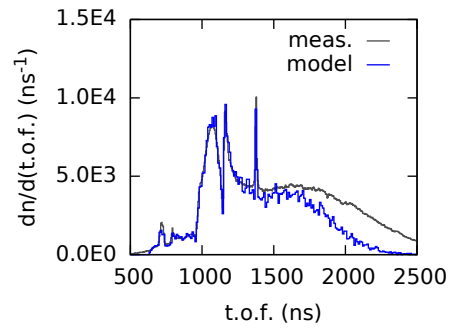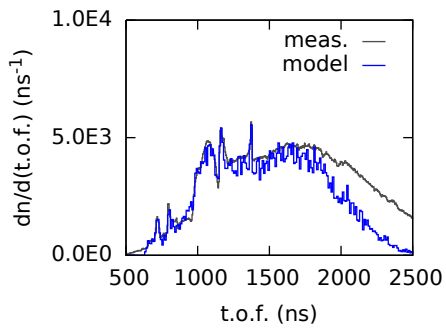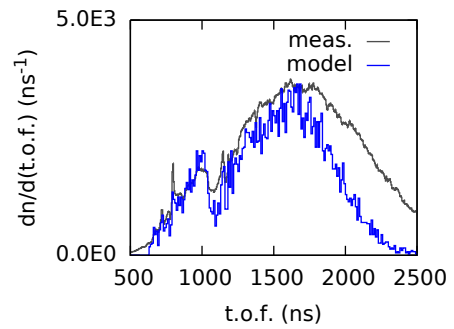
(b) Detector at 142.8°.

(c) Detector at 121.7°.
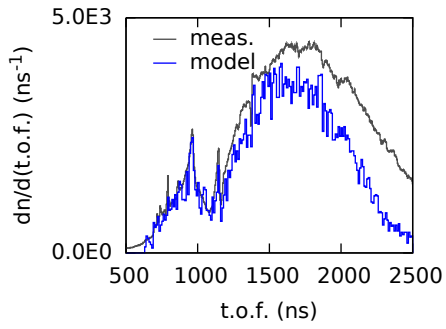
(d) Detector at 100.6°.
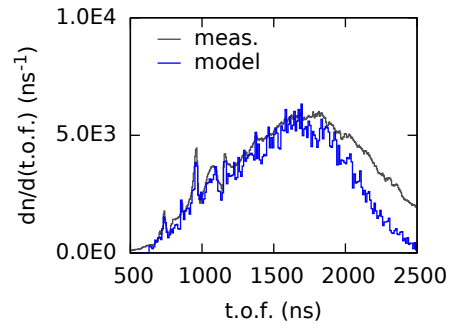
(e) Detector at 79.4°.
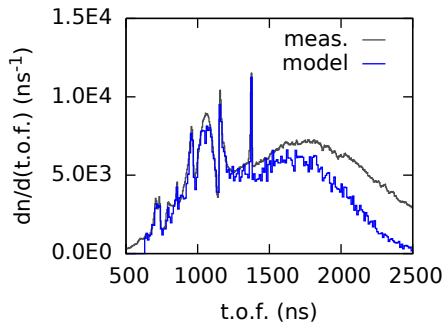
(f) Detector at 58.3°.
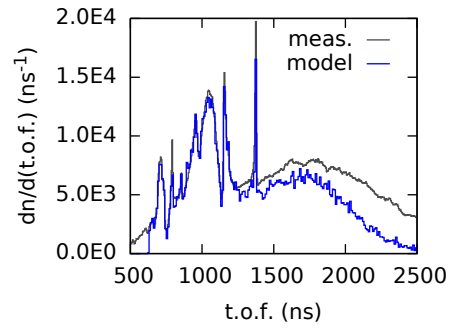
(g) Detector at 37.2°.

(h) Detector at 16.2°.

Figure 4.6: Same as figure 4.5 but for a set of EJ315 detectors.
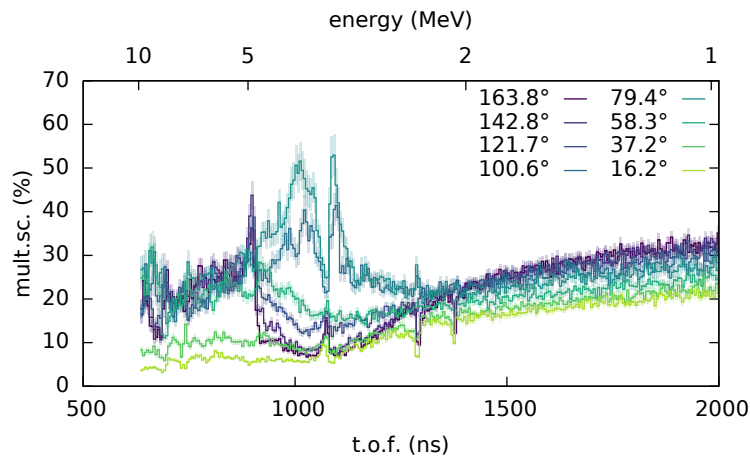
Figure 4.7: Percentage (as a function of the t.o.f.) of events characterised by a neutron colliding multiple times in the graphite target then scattering in the direction of a detector at a given angle. The secondary x-axis gives the incident energy on the target of a neutron scattering elastically to 90°.

4.2.3 Monte Carlo simulations

In figures 4.5 and 4.6, the neutron t.o.f. distributions, measured with one set of EJ301 detectors and one set of EJ315 detectors, are shown after the subtraction of the sample-out measurement. The data are compared with the result of a MCNP simulation modelling the experiment. The "full-setup" simulation included all 32 scintillators, the graphite target and the elements of the experimental setup close by. These consisted of the target holder, the aluminium bars supporting the detectors and the air all around them. The air along the neutron beam path was not taken into account (the simulated neutron beam propagates in vacuum), because its contribution was already taken care of when subtracting the sample-out measurement. The neutron source energy distribution was defined using the measurement with the fission chamber (using the fluence data shown in figure 4.2).

One of the reasons to implement this simulation was to investigate how well the detector model performed and how well the detector response was known. To reproduce the measurements, each neutron history generated by MCNP was analysed individually, to determine if it crossed any of the scintillator liquid cells, and if it generated light by colliding with ^{1}H or ^{2}H. The light output L determined only as a function of the ^{1}H or ^{2}H recoil energy (see equation (3.9)). To take into account the effects of the finite resolution of the detector, a random increment δL (either positive or negative) was also generated, following a normal distribution centred around 0 with a variance given by equation (3.7)). The parameters A_1, A_2, A_3 of the light output function, and B_0, B_1, B_2 of the resolution function, were set for each detector individually, according to the results of its calibration. If the final light output ($L + \delta L$) was higher than the experimental detection threshold of the detector, it was used to build the t.o.f. distribution. If not, it was rejected. Figure 4.5 shows the results of this procedure applied to one set of EJ301 scintillators, while in figure 4.6 the same is repeated for a set of EJ315 detectors.

The simulation agrees well with the measurement for t.o.f. shorter than 1500 ns (neutron energies higher than 1.75 MeV). This applies to both the EJ301 and EJ315 detectors; the agreement is overall better in the case of the EJ301 detectors. This is not surprising considering the difficulties already met during the scintillator characterisation when trying to reproduce the light output distribution of the EJ315 detectors. For t.o.f. longer than 1500 ns, in general the simulation tends to underestimate the data. This indicates a low-energy limit below which the simulated detector response might not be reliable.

The other objective of the full-setup simulation was the assessment of the impact of multiple scattering. Analysing the path followed by each simulated neutron, it was possible to evaluate the number of scattering events. Only neutrons scattering to the solid

angles subtended by the detectors were considered. The multiple scattering percentage was defined as the ratio of neutrons that collided twice or more in the target to the total number of neutrons. The multiple scattering percentage as a function of the detector position (the nominal scattering angle) and the t.o.f. is represented in figure 4.7. As the target is a disk of 1 cm thickness, the multiple scattering contribution is non-negligible for all time-of-flights. It affects in particular the detectors placed at angles close to 90°, i.e. closer to the side of the graphite disk than the other detectors. For these detectors, the number of multiple scattering events can, depending on the t.o.f., amount up to 50% of the total. The less affected detectors are the most forward ones: in the t.o.f. range of interest (500 ns–1500 ns), the multiple scattering percentage never exceeds 20%.

The considerations on the multiple scattering correction concern also to the measurements shown in chapter 3 regarding the determination of the detector neutron response. The light output histograms shown in figures 3.17 and 3.18 are not corrected for multiple scattering events, which however represent a non-negligible percentage of the recorded events. This implies that the inconsistencies found for EJ315 detectors between modelled and measured distributions might be also caused by multiple scattering events, especially since the discrepancies are most noticeable for low light output values. The light output parameter determination is based on the selection of elastic scattering events, which are characterised by the highest light output values. Therefore it is possible that multiple scattering did not affect the results of the analysis too much. The results of the characterisation procedure based on the detection of scattered neutrons should nevertheless be validated. This could be achieved by carrying out a second measurement in which the detectors are directly irradiated with neutrons. Actually, such experiment was already carried out at the cyclotron of the Physikalisch-Technische Bundesanstalt (PTB) in Braunschweig using the (d,Be) reaction to produce neutrons, and the analysis is ongoing.

4.2.4 Elastic scattering separation

The light output distributions obtained by gating the data on t.o.f. intervals of 5 ns each (the time resolution that characterises this measurement) were already shown when discussing the calibration of the scintillators, in figures 3.17 and 3.18. The experimental distributions in those figures were obtained after the subtraction of the sample-out background component. The separation of the elastic scattering was performed, in that case, to obtain quasi-monoenergetic neutrons. The same results, however, could be also used to determine the elastic scattering reaction yields.

The method for determining the elastic scattering reaction yield as a function of the scattering angle is based on the consideration that for a given t.o.f. interval the most energetic neutrons must have arrived at the detector after a single elastic collision in the target. Any other process will inevitably produce less energetic neutrons.

For each t.o.f. interval, the highest detected neutron energy E'_{el}, corresponding to elastic scattering, and the second highest energy E'_{inl}, corresponding to inelastic scattering from the first excited level of carbon, are determined using equations (2.3), (2.4) and (2.5). Neutrons corresponding to these two energies generate in the detector two light output distributions that overlap only for values lower than a certain threshold, which basically depends on the energy gap between ground state and first excited state of the target. Therefore it is possible to isolate an interval where only elastic scattering events occur by applying a proper threshold on the light output distributions.

The threshold L_{THR} depends on the energy E'_{inl}, therefore it is different for each t.o.f. interval. It can be determined by calculating the maximum light output $L_{MAX,inl}$ produced in an inelastic event. Each value of E'_{inl} corresponds to a maximum deposited energy E_r^{MAX} (the maximum recoil energy of either protons or deuterons) that can be calculated using equation (3.11). From E_r^{MAX}, the maximum light output $L_{MAX,inl}$ can be determined by applying the light output function (3.9): $L_{MAX,inl} = L(E_r^{MAX})$. The threshold value L_{THR} has to take into account also the effect of the detector resolution σ_L (3.7), and therefore is defined as: $L_{THR} = L_{MAX,inl} + 2\,\sigma_L$.

(a) t.o.f. = 976–981 ns
* E_{el} = 2.95–2.98 MeV
* E_{in} = NA

(b) t.o.f. = 781–786 ns
* E_{el} = 4.61–4.67 MeV
* E_{in} = 1.10–1.15 MeV

(c) t.o.f. = 756–761 ns
* E_{el} = 4.93–4.99 MeV
* E_{in} = 1.38–1.44 MeV
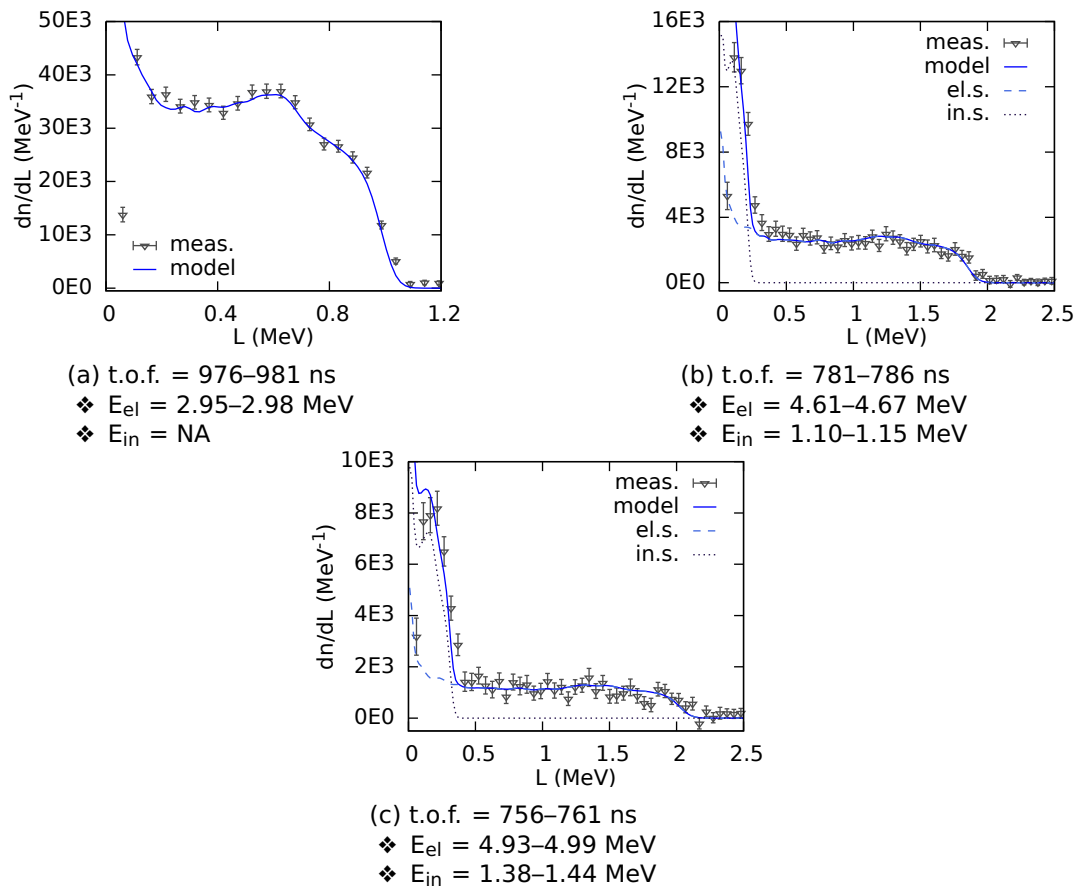
Figure 4.8: Neutron light output distribution (dn/dL) measured with an EJ301 detector at 163.8° ("meas."), compared to the detector response ("model"). The response is the sum of the contribution of elastic scattering ("el.s.") and of inelastic scattering from the first excited state of carbon ("in.s."). The experimental light output distributions were obtained gating on the t.o.f. intervals indicated below each figure. E_{el} and E_{in} are the corresponding neutron energies after an elastic ("el") or inelastic ("in") collision with carbon.

(a) t.o.f. = 976–981 ns
- E_{el} = 2.95–2.98 MeV
- E_{in} = NA

(b) t.o.f. = 781–786 ns
- E_{el} = 4.61–4.67 MeV
- E_{in} = 1.10–1.15 MeV

(c) t.o.f. = 756–761 ns
- E_{el} = 4.93–4.99 MeV
- E_{in} = 1.38–1.44 MeV
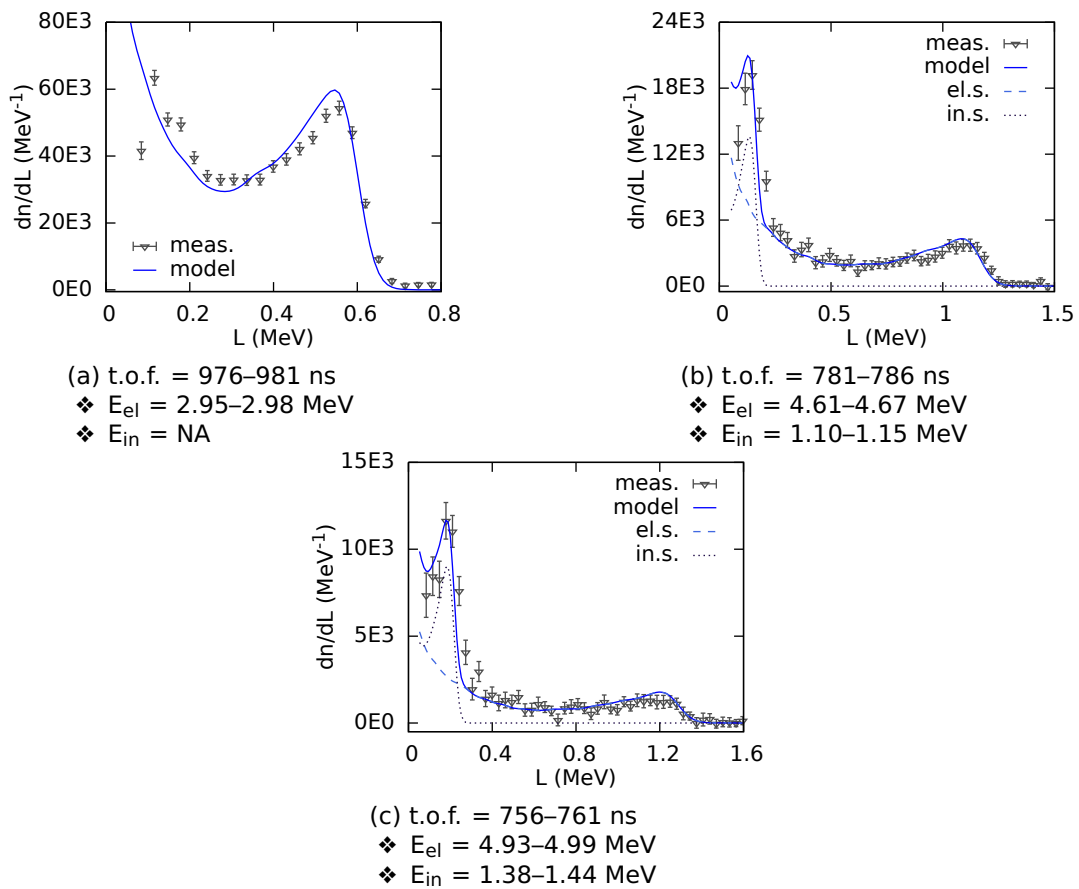
Figure 4.9: Same as figures 4.8, but for an EJ315 detector at 163.8°.

The detector response $R(L, E'_{el})$ to neutrons with energy E'_{el} (elastically scattered neutrons) is calculated, then fitted to the experimental light output spectrum in the interval above the threshold L_{THR}. The resulting distribution $R_{fit}(L, E'_{el})$ gives the contribution of the elastic scattering events to the total light output distribution. The same principle can be applied, using appropriate thresholds, to discriminate neutrons scattering from the first level to those scattering from the second level, the second level can be separated from the third, and so forth depending on the experimental limitations. In figures 4.8 and 4.9, the decomposition of the detector response into the elastic and inelastic contributions is shown for two detectors (one EJ301 and one EJ315) placed at 163.8°.

The integral of R_{fit} divided by the detection efficiency ε and the detector opening angle $\Delta\Omega$ gives the number of neutrons emitted to the scattering angle θ. This number is still affected by the multiple scattering contribution, but the fraction F_{msc} of multiple scattering events is known: it was obtained as a function of t.o.f. and θ by analysing the MCNP full-setup simulation (figure 4.7). Therefore, the number of elastic scattering events is computed using the formula:

$$Y_{el}(t.o.f., \theta) = \frac{1 - F_{msc}(t.o.f., \theta)}{\varepsilon(E'_{el})\big|_{L_{THR}} \Delta\Omega} \int_{L_{THR}} R_{fit}(L, E'_{el}) \, dL \qquad (4.4)$$

where $\varepsilon(E'_{el})\big|_{L_{THR}}$ is the detection efficiency as a function of the detected neutron energy E'_{el} obtained for the threshold value L_{THR} using equation (3.4).

As the result includes only single scattering events, the equation giving the neutron incident energy as a function of the t.o.f. (equation (2.3)) can now be uniquely solved. If $Y_{el}(E, \theta)$ is the elastic scattering reaction yield as a function of the neutron incident energy E, the differential cross section $\frac{d\sigma}{d\Omega}(E, \theta)$ is determined by applying:

$$\frac{d\sigma}{d\Omega}(E, \theta) = \frac{Y_{el}(E, \theta)}{\rho_T \, \Phi(E) \, A_b} \qquad (4.5)$$

where ρ_T is the target areal density (in atoms per unit surface), $\Phi(E)$ is the incident neutron fluence, and A_b is the cross-sectional area of the neutron beam. An important observation (as it affects the uncertainties) is that the area A_b (appearing both here and in the fluence expression, equation (4.1)) is never used when calculating cross sections. The relevant quantity in equation (4.5) is the total number of incoming neutrons $A_b \Phi(E)$. This can be determined from equation (4.1) without knowing the value of A_b. In this way, the beam divergence (and the fact that $\Phi(E)$ and A_b actually assume different values in the two equations) is also automatically taken into account (see chapter 2, equation (2.2) and discussion). The angle-integrated cross section $\sigma(E)$ is then calculated applying the Gauss-Legendre quadrature rule (equation (2.7)).

4.3   Results and comments

In figures 4.10 and 4.11, the results for the angle-integrated cross section of neutron elastic scattering on carbon is shown. In figure 4.10a, the result determined for each of the four sets of scintillators individually is shown, while in figures 4.10b and 4.11 the average of the four measurements is reported. The data are compared with the standard neutron cross section reported in the ENDF/B-VII.1 nuclear data library (figure 4.10) and the other measurements from the EXFOR database (figure 4.11).

The results of the four detector sets can be used to test the repeatability of the measurement. The four cross section sets turned out all to be compatible with each other in the neutron energy range from 1.5 MeV to 7.2 MeV. These datasets were analysed individually but are not uncorrelated, because they all depend, e.g, on the same fluence measurement, and the same multiple scattering correction. As they are not independent measurements, they cannot be taken separately, and the final cross section is determined as their average.
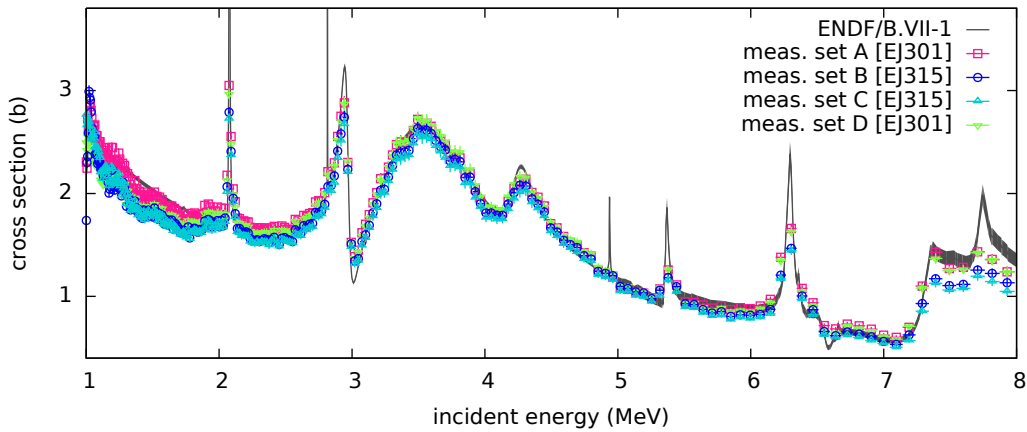
(a) The results of each set of scintillators (identified as set A, B, C and D) is shown. For each set, the detector type (EJ301 or EJ315) is indicated in the plot key in square brackets.
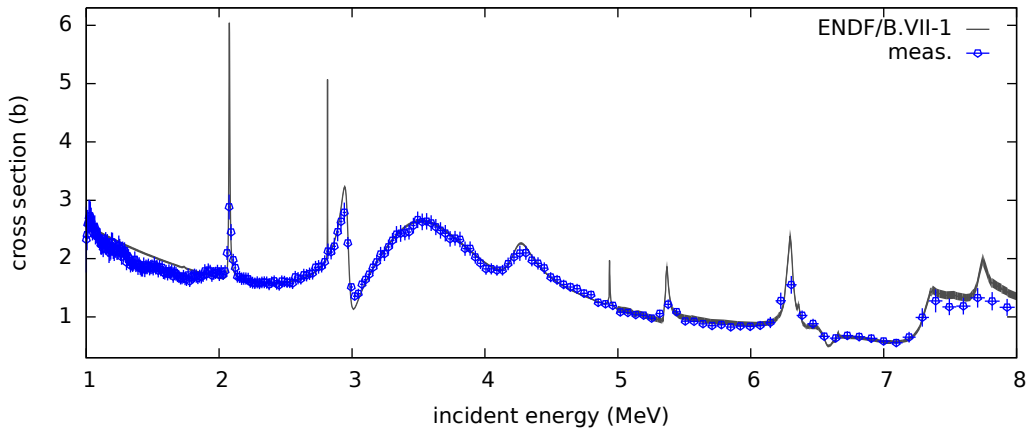
(b) The measured values are the average of the results obtained with the four sets of scintillators.

Figure 4.10: Angle-integrated cross section of neutron elastic scattering on natural carbon as a function of the neutron incident energy: comparison of the measured ("meas.") values with the neutron cross-section standard reported in the ENDF/B-VII.1 library.
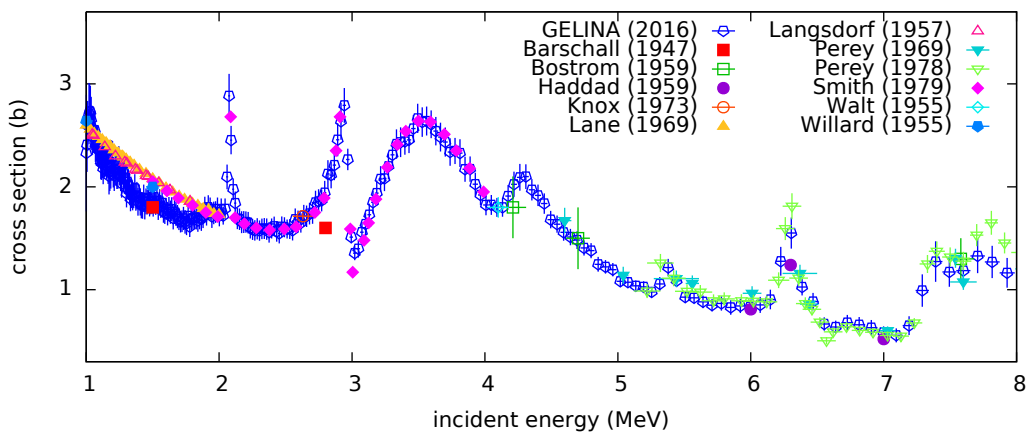
Figure 4.11: Comparison of the elastic cross section measured at GELINA with the other experiments from the EXFOR database (see table 4.1).
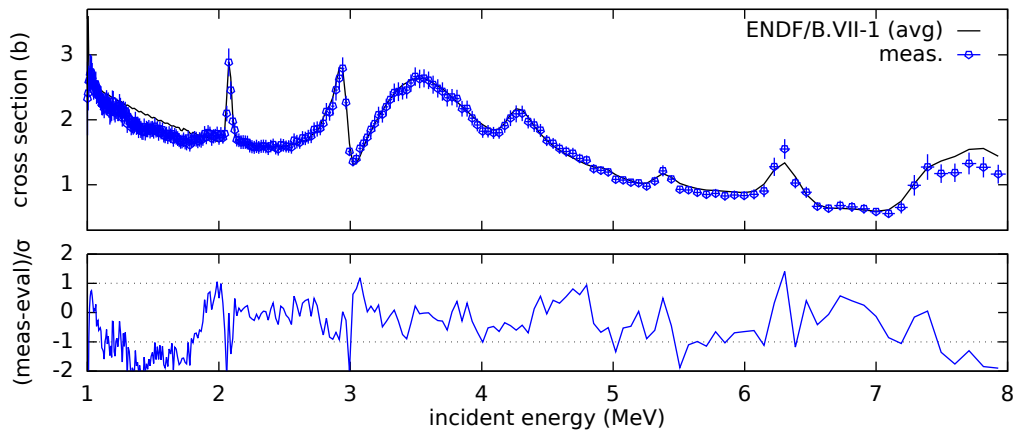
Figure 4.12: Elastic scattering cross section: the measurements are compared to the evaluation averaged according the experimental energy resolution ("ENDF/B-VII.1 (avg)"). The deviation of the experimental data from the evaluated cross section, expressed as the difference between measurement and evaluation (*meas* − *eval*) divided by the experimental uncertainty (σ), is also shown as a function of the neutron incident energy.

The uncertainty of the average was resolved from the spread of the four values around the average. This was done in order to take into account the systematic uncertainties deriving from that fact that, in the MCNP model used for the determination of the detector efficiency, the fluctuations in the hydrogen content from one detector to other were not known, so the nominal values stated by the manufacturer had to be used instead. The final uncertainties range from 5% to 10% (up to 12% for some points): Below 6 MeV, they vary between 5% to 7%; above, they start to increase.

The experimental cross-section data are compatible with the cross-section standard and the other experiments in the range from 1.9 MeV to 7.5 MeV. The sharp resonances at 2.816 MeV and 4.937 MeV, however, could not be measured because of the energy resolution. The resonance at 2.078 MeV is observed, but the resolution effects are clearly visible there as well. To better account for those effects, in figure 4.12 the measurements are compared with the evaluation averaged according to the experimental energy resolution. In the interval from 1.9 MeV to 7.5 MeV, the ratio experiment to "averaged evaluation" varies between $-\sigma$ and σ (here σ indicates the experimental uncertainty), except in few points close to the resonances, where however it never exceeds $|2\sigma|$. Above 7.5 MeV, i.e. for t.o.f. shorter than 741–743 ns (depending on the scattering angle), the reason for the discrepancies is possibly the poor statistics, which made the determination of the reaction yields difficult. Below 1.9 MeV (t.o.f. longer than 1437–1440 ns), the fit of the detector response to the experimental light output distributions did not work out well. The neutron energy after the collision is very close to the detection threshold which means that the pulse height distributions do not extend much above said threshold, and this leaves only few points for the fit.

The differential cross section (the average of the four sets of results) measured at GELINA is compared with other measurements in figure 4.13. In this figure, the cross section is represented as a function of the scattering angle for 10 different energy intervals. The experimental points are also compared with the ENDF/B-VII.1 evaluation. In figure 4.14, the data are presented by angle, as a function of the incident energy, and compared with the evaluation only. The uncertainties on the differential cross section are a bit higher than on the reaction cross section, and range between 9% and 15%.

Above 1.8 MeV, the evaluated differential cross section is not recommended as a standard. The uncertainty on the angle-integrated cross section is still low enough that it can be used for comparisons, however the same does not apply to the angular distributions. Therefore, some discrepancies between measured and evaluated distributions are not auto-

matically regarded as a consequence of a measurement error.

Below 1.9 MeV, the issues with the data analysis are visible in particular at 100.6° and 79.4°, while at the forward angles this does not seem to have been a problem. Above 7.5 MeV, instead, the discrepancy is registered only at 16.2°, the most forward angle.

In the range from 1.9 MeV to 7.5 MeV, the agreement of measurements and the evaluation (figure 4.14) is overall good at the most backward (163.8°, 142.8° and 121.7°) and most forward angles (58.3°, 37.2° and 16.2°). In figures 4.13a and 4.13b (at ca. 2.087 MeV and 2.5 MeV), it is even possible to see how at backward and forward angles the evaluation seems to favour GELINA measurements over the other datasets.

Close to 90° (at 100.6° and 79.4°) some discrepancies are observed, especially in the energy interval from 3 MeV to 5 MeV. Looking at the other available measurements in the same energy range, figures 4.13d and 4.13e in particular, it is possible to observe that the different datasets are compatible with each other, and that the evaluation does not reproduce them well. Also the data plotted in figures 4.13f belong to the range 3 MeV– 5 MeV; there however, the two datasets are not compatible at angles close to 90°. In the same energy interval, centred at 4.6 MeV, and for the same angles, the multiple scattering percentage (figures 4.7) is close to 50%, which might explain this difference. The angle integration in the same range gives nevertheless very good results, and this is despite of the fact that the central angles are those with the highest weight in the Gauss-Legendre quadrature (see table 2.1). There is in principle no reason to suspect a systematic error, however a second measurement with a thinner carbon sample would be recommended. If these results were to be confirmed, these discrepancies would raise a question over the evaluation of the differential cross sections.

In general, it was possible to prove that with this experimental setup, accurate differential and angle-integrated scattering cross section measurements can be achieved for fast neutrons in the energy range from 2 MeV to 7 MeV. Some improvements could nevertheless be envisioned, principally trying to extend the energy range. The extension to lower energies is probably the easiest to implement: lowering the detector electronic thresholds could possibly suffice (if the noise levels allow it). Another recommendation arises from the investigation of the multiple scattering impact: the thickness and diameter of the target are important parameters to consider in order to avoid that the analysis is dominated by the corrections.

The measurement on carbon was meant to be used for validation only; however some discrepancies between evaluations and measurements, not only those here presented, but also works from other authors, were observed. Further investigations might be worthwhile.
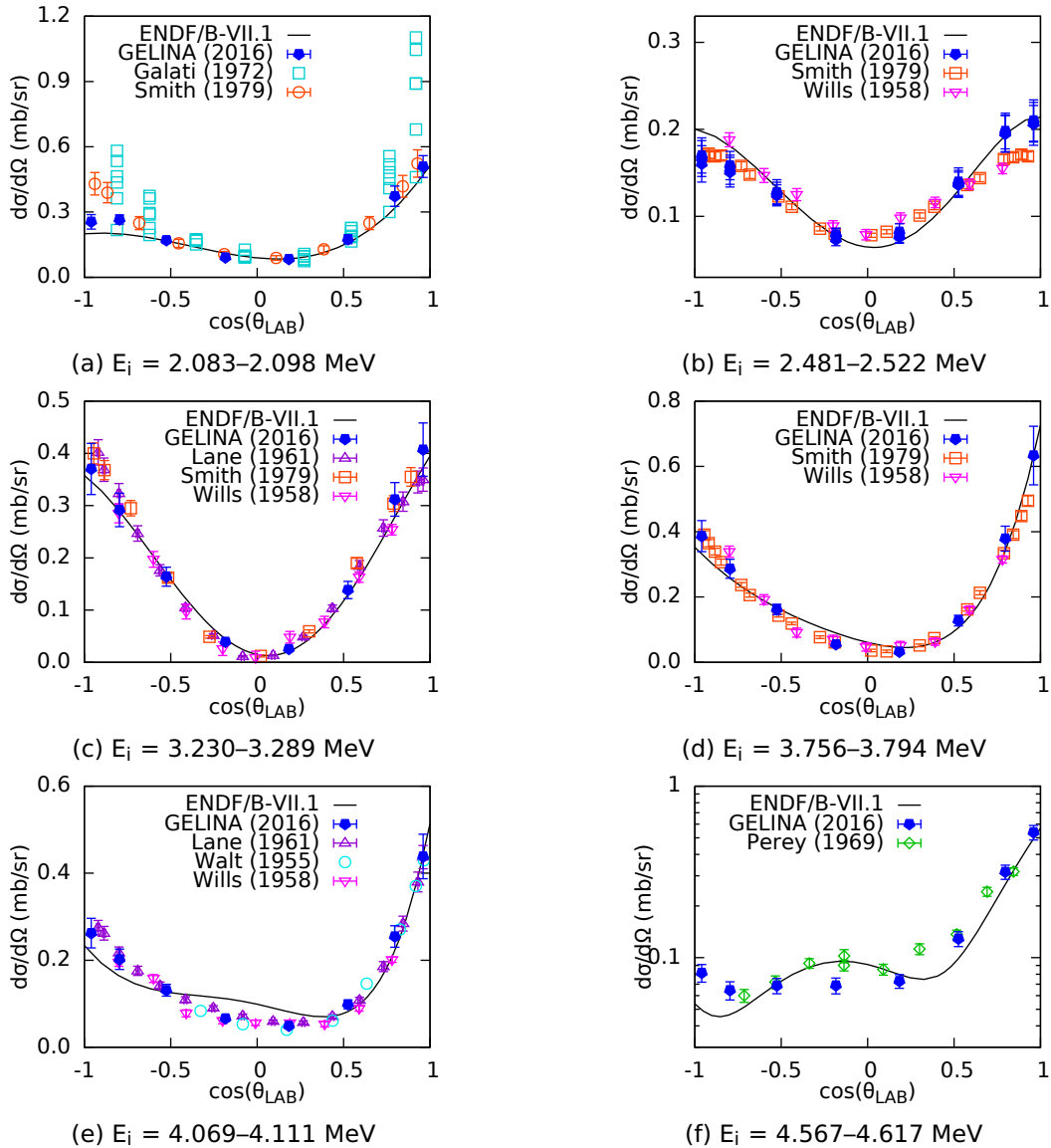
Figure 4.13: Differential cross section $d\sigma/d\Omega$ of neutron elastic scattering on carbon as a function of the cosine of the scattering angle in the laboratory system θ_{LAB}, for selected incident neutron energy intervals (E_i as indicated below each plot). The results of the measurements at GELINA are compared with the measurements from the EXFOR database and the angular distribution reported in the ENDF/B-VII.1 library.

(g) E_i = 5.285–5.347 MeV

(h) E_i = 5.540–5.607 MeV

(i) E_i = 6.530–6.596 MeV

(j) E_i = 6.953–7.047 MeV
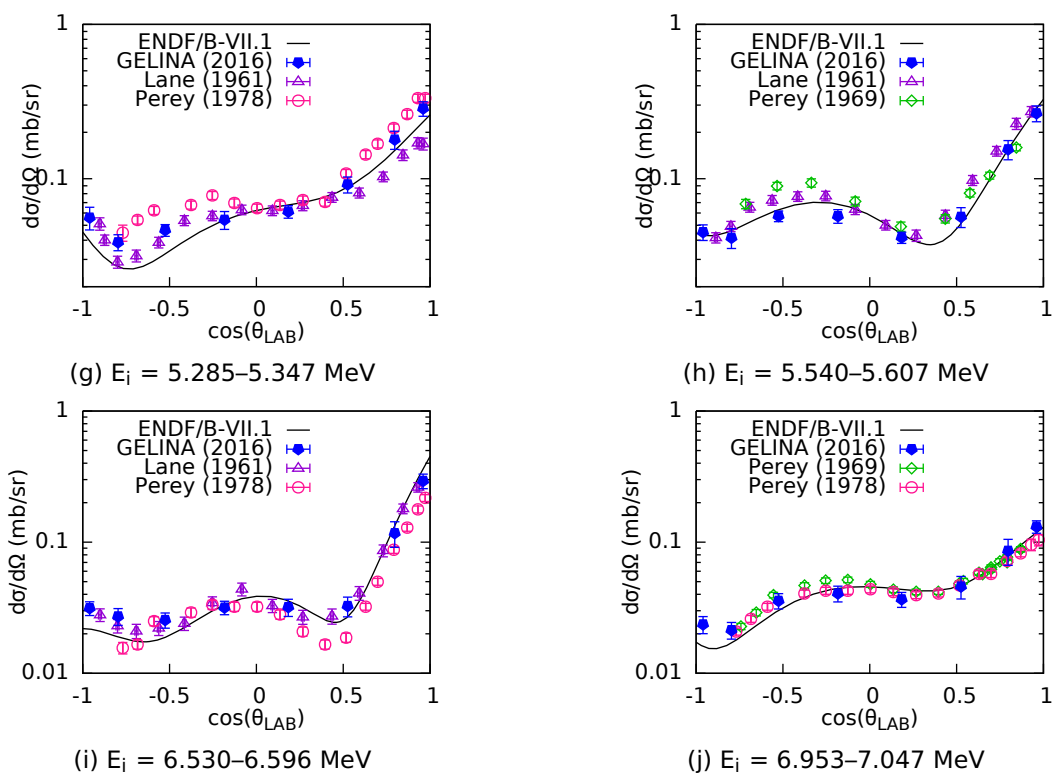
Figure 4.13: Continued from previous page.
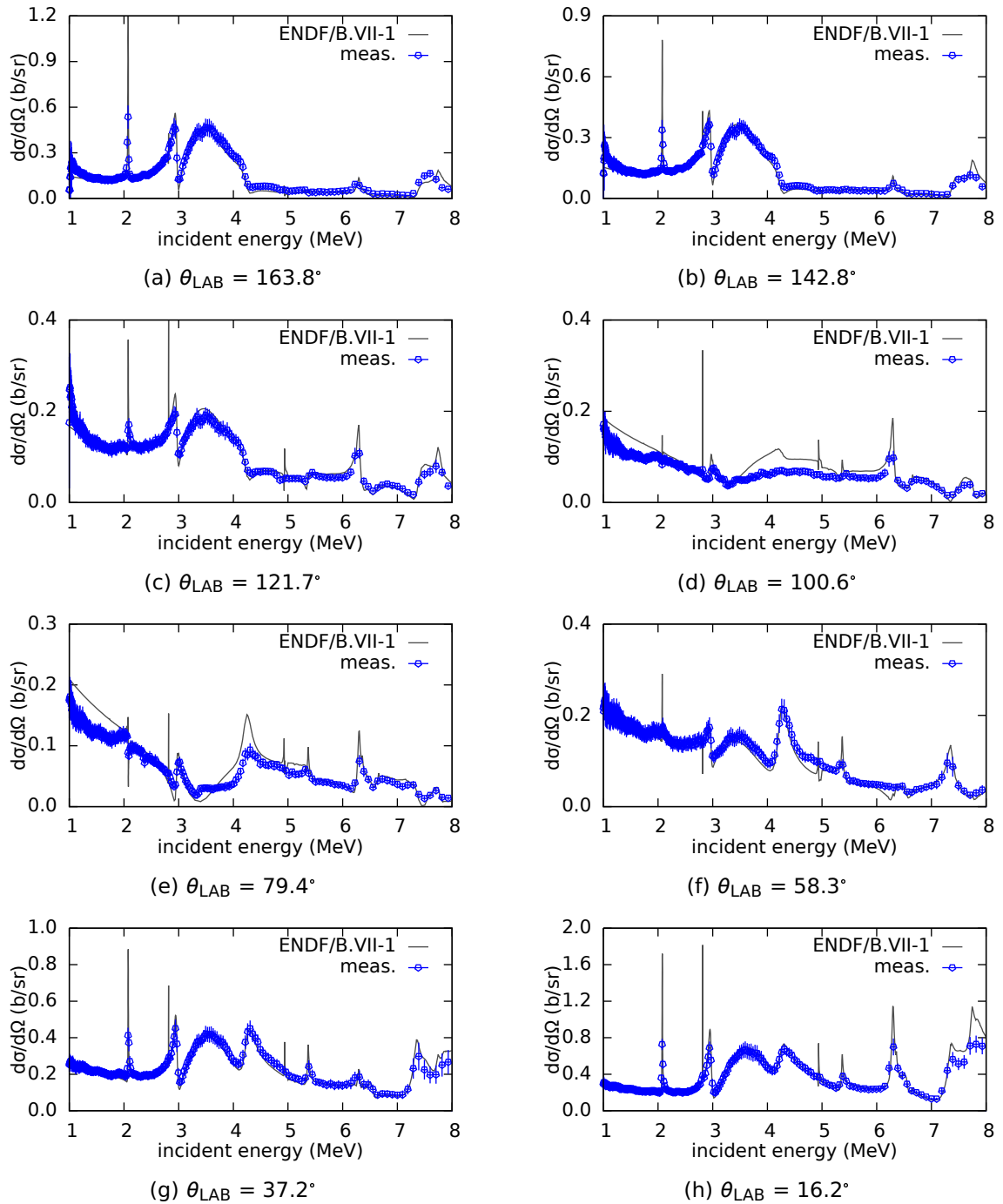
Figure 4.14: Differential cross section $d\sigma/d\Omega$ of neutron elastic scattering on natural carbon as a function of the neutron incident energy: comparison of the measured values ("meas.") with the evaluation from the ENDF/B.VII-1 nuclear data library at the laboratory angles θ_{LAB}.

Neutron scattering on iron

The experiment for the investigation of neutron scattering cross section on iron was first carried out in 2015 at the nELBE facility using 16 detectors (8 EJ301 and 8 EJ315). It was then repeated in 2016 at GELINA with the full setup of 32 detectors. The experiment was repeated using two different samples of similar thickness, and two different data acquisition systems; only the detectors (scintillators and fission chamber), and the scintillators supporting frame were the same at both facilities. This provided further validation of the new experimental setup at GELINA, in particular the data acquisition system.

As an enriched ^{56}Fe sample is difficult to obtain, natural iron was considered instead for these first measurements. Natural iron includes four isotopes (^{54}Fe, ^{56}Fe, ^{57}Fe ^{58}Fe), and consists of 91.8% of ^{56}Fe (see table 5.1). Knowing the different level schemes, it is possible, in principle, to separate the inelastic scattering reactions on the different isotopes of iron. In this work, however, only ^{56}Fe was considered, because the abundances of the other isotopes are such to make the determination of their cross sections unfeasible. In the case of elastic scattering, however, the contribution of the single isotope cannot be easily disentangled. For this reason, for elastic scattering, the cross section and the angular distribution were obtained just for ^{nat}Fe.

In table 5.2, the energy levels of ^{56}Fe are listed up to 3 MeV. The neutron source covers all these energies, and goes even higher. In practice, however, the resolution of the detectors does not allow to distinguish between neutrons scattering from two levels too close in energy, e.g. like the level at 2941.5 keV and the following one at 2960.0 keV. Therefore, the inelastic scattering results will be limited to a reduced number of levels. For comparison, the first four excited levels of ^{54}Fe and ^{57}Fe are also given in tables 5.3a and 5.3b. The first excited state of ^{57}Fe (14 keV) is practically indistinguishable from elastic scattering, and the other three levels are all below the first excited level of ^{56}Fe, so their contributions will all be added to the elastic scattering yield. The first level of ^{54}Fe (1408 keV) is higher than the first level of ^{56}Fe but lower than the second, meaning that it will contribute to the cross section of inelastic scattering. The contributions of ^{54}Fe and ^{57}Fe are limited, however they increase the uncertainties on the measurement of ^{56}Fe. The low abundances of these two isotopes and the scintillator resolution, it is not possible to account for them. The use of an enriched ^{56}Fe sample in future experiments would be ideal.

For inelastic scattering on ^{56}Fe, it will be shown that scattering from the first three excited states can be separated reasonably well from the rest of the data. However, the uncertainty on the cross section increases remarkably with increasing level energy. This is

Table 5.1: Physical properties of natural iron. The isotopic composition is given in atom percent, and was taken from [89]; the atomic mass is from [90].

^{nat}Fe composition	^{54}Fe: 5.845(105)%
	^{56}Fe: 91.754(106)%
	^{57}Fe: 2.119(29)%
	^{58}Fe: 0.282(12)%
Atomic mass	55.845(2) g/mol

Table 5.2: List of the levels of ^{56}Fe [94] up to 3 MeV. E^* is the energy of the level, J^π gives the angular momentum and parity (values between brackets are uncertain), $T_{1/2}$ is the half-life of the state.

E^* (keV)	J^π	$T_{1/2}$
0	0^+	stable
846.7778(19)	2^+	6.07(23) ps
2085.1045(25)	4^+	0.64(12)ps
2657.5894(25)	2^+	21(1) fs
2941.50(3)	0^+	0.45(9) ps
2959.972(4)	2^+	28(3) fs
3076.2(4)	(3^-)	

Table 5.3: First levels of ^{54}Fe [95] and ^{57}Fe [96]. E^* is the energy of the level, J^π gives the angular momentum and parity, $T_{1/2}$ is the half-life of the state.

(a) ^{54}Fe

E^* (keV)	J^π	$T_{1/2}$
0	0^+	stable
1408.19(19)	2^+	0.76(2) ps
2538.1(3)	4^+	4.0(8) ps
2561.3(4)	0^+	$\geq$1.4 ps
2900	2^+	

(b) ^{57}Fe

E^* (keV)	J^π	$T_{1/2}$
0	$1/2^-$	stable
14.4129(6)	$3/2^-$	98.3(3) ns
136.4743(5)	$5/2^-$	8.7(3) ns
366.759(7)	$3/2^-$	10.5(14) ps
706.416(16)	$5/2^-$	4.1(11) ps

because the cross section (and the statistics) tends to decrease, but the most significant contribution is given by the subtraction of the underlying levels' contribution, which is a progressively increasing source of uncertainty. For this reason, the cross section of scattering from the first excited state only will be presented. The results will be used as example to discuss the data analysis method and the uncertainties.

The results cover the incident neutron energy range from 2 MeV to 6 MeV, and will be compared with the existing measurements in the same energy range. For elastic scattering on natural iron, the references are listed in table 5.4, while for inelastic scattering from the first excited state of ^{56}Fe they are in table 5.5. For elastic scattering, high energy resolution measurements are present for both the reaction cross section and the angular distribution for energies up to 3 MeV. Above 3 MeV the measurements become sparse, however, they are still more abundant than those for inelastic scattering. For inelastic scattering, the reaction cross section has been measured with high resolution up to 4.5 MeV, and up to 5 MeV a good number of experimental points are available. For the angular distributions, the measurements are scarce, in particular above 3 MeV.

5.1 Experimental details

In both experiments, at GELINA and nELBE, a 3 mm disk of natural iron was employed as neutron target (the other dimensions are reported in table 5.6). For the experiment at GELINA, the iron disk was placed at a flight path at 108° from the direction of the electron beam, at a distance of 27.037(5) m from the neutron source. At nELBE, the neutron flight path from the source to the sample was 8.300(5) m long, and to reduce the photon fluence on the target, a lead absorber of 3 cm thickness was set up in front of the neutron beam collimator. The scintillator array at nELBE included two sets of detectors, 8 EJ301 and 8 EJ315 (see figure 3.4b); at GELINA the full array with 32 scintillators was used (figure 3.4a). For the data acquisition, the in-house developed systems already installed at the two facilities were used. The conditions at GELINA were the same as for the carbon experiment, therefore the t.o.f. resolution remained unchanged (5 ns). At nELBE, the t.o.f. resolution was found to be of 1 ns, which is close to the time resolution of the detectors. It corresponds to

Table 5.4: From the EXFOR database: measurements of the reaction cross section ("CS") and of the differential cross section with respect to the angle ("DA") of neutron elastic scattering on ^{nat}Fe, covering the incident neutron energy from 2 MeV to 6 MeV. For each experiment, referred with the name of the first author and the year of publication, the incident neutron energy range and the number of points ("No. points") are indicated.

Reference		Energy (MeV)	Quantity (No. points)	
Becker (1966)	[97]	3.2		DA (14)
Begum (1981)	[98]	2.9		DA (11)
Beyster (1956)	[99]	2.5–7		DA (30)
Bostrom (1959)	[100]	3.67–4.7	CS (3)	DA (36)
Cierjacks (1978)	[101]	0.4889–3.0625		DA (18399)
Cranberg (1956)	[102]	2.25–2.45	CS (2)	DA (25)
Galloway (1979)	[103]	2.9		DA (9)
Gilboy (1965)	[104]	0.98–3.99	CS (4)	
Hill (1956)	[105]	5		DA (6)
Hill (1958)	[106]	5		DA (13)
Holmqvist (1969)	[107]	2.96–8.5	CS (5)	DA (60)
Holmqvist (1970)	[108]	1.77–2.76	CS (5)	DA (72)
Holmqvist (1971)	[109]	5.96	CS (1)	DA (13)
Hopkins (1964)	[110]	2–5		DA (7)
Jacquot (1966)	[111]	0.45–2.28	CS (8)	DA (264)
Kinney (1970)	[112]	4.6–8.56	CS (10)	DA (168)
Kinney (1976)	[113]	0.5–2.5	CS (2001)	DA (16008)
Korzh (1977)	[114]	1.5–3		DA (36)
Landon (1958)	[115]	2.2	CS (1)	DA (14)
Machwe (1959)	[116]	3.66	CS (1)	DA (24)
Pasechnik (1958)	[117]	2.8		DA (7)
Poole (1953)	[118]	2.5		DA (1)
Popov (1957)	[119]	2.9	CS (1)	DA (6)
Salnikov (1957)	[120]	2.34		DA (5)
Smith (1980)	[121]	1.684–3.905		DA (490)
Smith (1996)	[122]	4.5–9.99		DA (506)
Tomita (1970)	[123]	2.038–2.152		DA (54)
Tsukada (1961)	[124]	3.44–4.61		DA (59)
Tsukada (1969)	[125]	1.37–3.26		DA (5)
Walt (1955)	[86]	4.1	CS (1)	DA (11)

Table 5.5: From the EXFOR database: measurements of the partial cross section ("CSP") or the partial differential cross section with respect to the angle ("DAP") of neutron inelastic scattering on ^{56}Fe, with partial meaning that only scattering from the first excited state is considered. The measurements cover the incident neutron energy from 2 MeV to 6 MeV. For each experiment, referred with the name of the first author and the year of publication, the incident neutron energy range and the number of points ("No. points") are indicated.

Reference		Energy (MeV)	Quantity (No. points)	
Almen-Ramstrom (1975)	[126]	2.02–4.5	CSP (11)	
Barrows (1968)	[127]	2.9	CSP (1)	
Beyer (2014)	[128]	0.847–9.562	CSP (30)	
Boschung (1971)	[129]	5.05–5.58	CSP (2)	DAP (19)
Cranberg (1956)	[102]	2.25–2.45		DAP (26)
Degtjarev (1967)	[130]	1.37–3.76	CSP (7)	
Gilboy (1965)	[104]	2.01–3.99	CSP (3)	
Hicks (2015)	[131]	1.5–4.7	CSP (30)	
Kinney (1968)	[132]	4.6–7.55	CSP (7)	DAP (85)
Korzh (1977)	[133]	1.5–3.0	CSP (4)	DAP (35)
Lebedev (1977)	[134]	4.7		
Mittler (1975)	[135]	0.878–3.962	CSP (36)	DAP (5)
Negret (2013)	[136]	0.861–4.50	CSP (645)	
Nemilov (1982)	[137]	0.893–2.115	CSP (25)	
		4.13–5.0	CSP (7)	
Rodgers (1967)	[138]	2.33	CSP (1)	
Salama (1981)	[139]	2.02–3.96	CSP (6)	DAP (100)
Schweitzer (1978)	[140]	3.4	CSP (1)	DAP (12)
Tomita (1970)	[123]	2.038–2.152		
Tsukada (1969)	[125]	1.37–3.26		
		1.37–4.49		

Table 5.6: Dimensions and areal densities (measured quantities) of the two iron samples used at the two facilities, GELINA and nELBE.

	GELINA	nELBE
Diameter	7.103(1) cm	7.90(1) cm
Thickness	0.30(1) cm	0.31(1) cm
Mass	96.215(5) g	119.689(1) g
Areal density	2.4283(7) g/cm^2	2.442(6) g/cm^2
	0.026185(7) atoms/b	0.02633(7) atoms/b

Table 5.7: Comparison of the experimental conditions at GELINA and nELBE.

		GELINA	nELBE
Flight path	source-FC	25.667(5) m	6.044(5) m
	source-target	27.037(5) m	8.300(5) m
Beam-time		10 days	7 days
LINAC repetition rate		800 Hz	101 kHz
Flux @target		$2.965(2) \times 10^4$ n/cm^2/s	$1.076(2) \times 10^4$ n/cm^2/s
T.o.f. resolution		5 ns	1 ns
Energy resolution @1 MeV		5 keV	3 keV
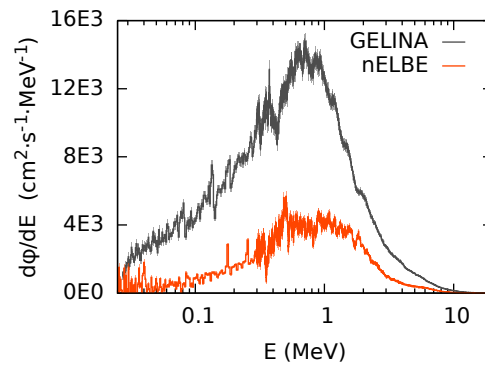
Figure 5.1: Energy distribution $d\varphi/dE$ of the neutron flux incident on the iron sample. The flux φ given here is the average over the measurement time.

3 keV resolution at 1 MeV of neutron energy. The incoming neutron fluence was measured in both experiments with the ^{235}U fission chamber from the JRC-Geel. At GELINA, the fission chamber was positioned 1.37 m upstream the iron target, while at nELBE is was at 2.256 m distance. In figure 5.1, the average over the measurement time of the incoming neutron flux energy distribution is shown. If energies between 25 keV and 20 MeV are considered, the corresponding flux on the target was, on average, of $1.076(2) \times 10^4$ neutrons/cm^2/s at nELBE and $2.965(2) \times 10^4$ n/cm^2/s at GELINA. This and other values related to the experimental conditions are also summarized in table 5.7.

5.2 Data analysis

The data analysis procedure was already explained in chapter 4, therefore here only the main differences will be highlighted. Two points will be discussed: the multiple scattering correction, and the discrimination of the inelastic scattering events.

5.2.1 Multiple scattering correction

To establishing the multiple scattering correction the same procedure was followed as for carbon: a MCNP simulation including all detectors (32 dectors for GELINA, 16 forn nELBE) was implemented, every neutron history was analysed and, for every detector, the percentage of multiple scattering events over the total number of neutrons striking it was computed. The results for detectors placed at the same angle were averaged in order to reduce the statistical fluctuations. In figure 5.2, the multiple scattering percentage is plotted as a function of the t.o.f. for two simulations, one for GELINA (figure 5.2a) and the other for nELBE (figure 5.2b). The targets used in the two experiments have almost the same thickness (3 mm for the GELINA target and 3.1 mm for the nELBE target, see table 5.6), so it is not surprising that the simulations give similar results. The most affected detectors are, as expected, those close to 90°, with the multiple scattering percentage ranging
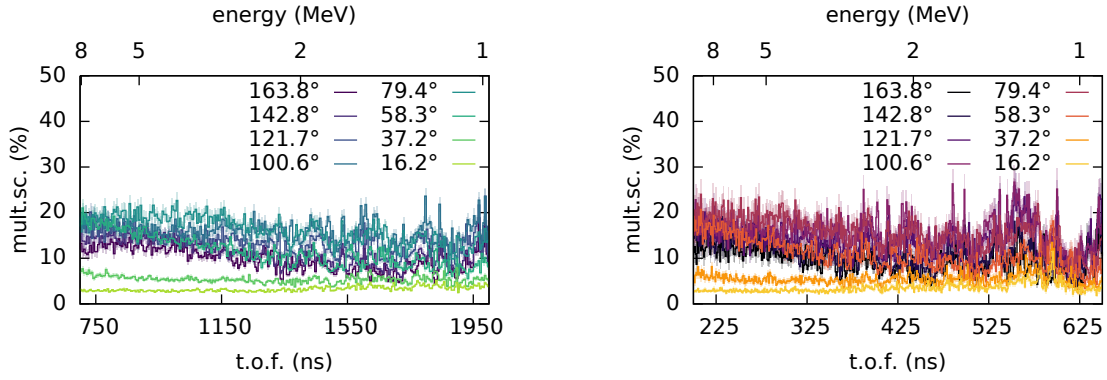
(a) Simulation for the measurements at GELINA.

(b) Simulation for the measurements at nELBE.

Figure 5.2: Percentage (as a function of the t.o.f.) of events characterized by a neutron colliding multiple times in the iron target then scattering in the direction of a detector at a given angle. The secondary x-axis gives the incident energy on the target of a neutron undergoing an elastic collision with ^{56}Fe then scattering at 90°.

between 12% and 22% for energies above 2 MeV. The most forward detectors are those less affected, with percentages not going beyond 10% in the energy range of interest. The multiple scattering correction is non-negligible, however it is much less critical than for the carbon measurement; these results highlight once again the importance of properly choosing the target dimensions when planning the experiments. The target cannot be too thin because the reaction rate would be too low, however the diameter, for example, should not be much larger than the beam, as the detectors close to its sides are clearly the most affected.

5.2.2   Separation of elastic from inelastic scattering

A similar procedure as that outlined for the analysis of the carbon data is followed also for iron. For each detector, the neutron events are divided into small t.o.f. intervals, and the analysis is performed starting from the longest t.o.f., moving towards shorter times. As the time decreases, the neutron energy and the number of open scattering channels increase. In non-relativistic approximation, the inelastic scattering threshold for a level of energy E^* is given by $E^*(A + 1)/A$, where A is the ratio between the target mass and the neutron mass. Using this expression and equation (2.3), it is possible to know which channels are open for which t.o.f interval. For each open channel, equation (2.5) is applied to determine the energy of the neutrons striking the detector, and the resulting energy is employed to model the detector response.

For each level LV (from the ground state, $LV = 0$, to the highest level for which the incident neutron energy is higher than the inelastic threshold), the following quantities are computed:

- ❖ the neutron energy before the collision in the target E_{LV};

- ❖ the energy after the collision E'_{LV};

- ❖ the detector response $R(L, E'_{LV})$ as a function of the light output L;

- ❖ the maximum proton/deuteron recoil energy that can be registered $E^{MAX}_{r,LV}$ (equation (3.11)), and the maximum light output signal that can be produced in the detector $L_{MAX,LV} = L(E^{MAX}_{r,LV})$ where $L(E)$ is the light output function of the detector (equation (3.9));

- ❖ the light output threshold below which the contribution of the level LV+1 can also be observed: $L_{THR,LV} = L_{MAX,LV} + 2\,\sigma_L$, where σ_L (equation (3.7)) is calculated in $L_{MAX,LV}$.
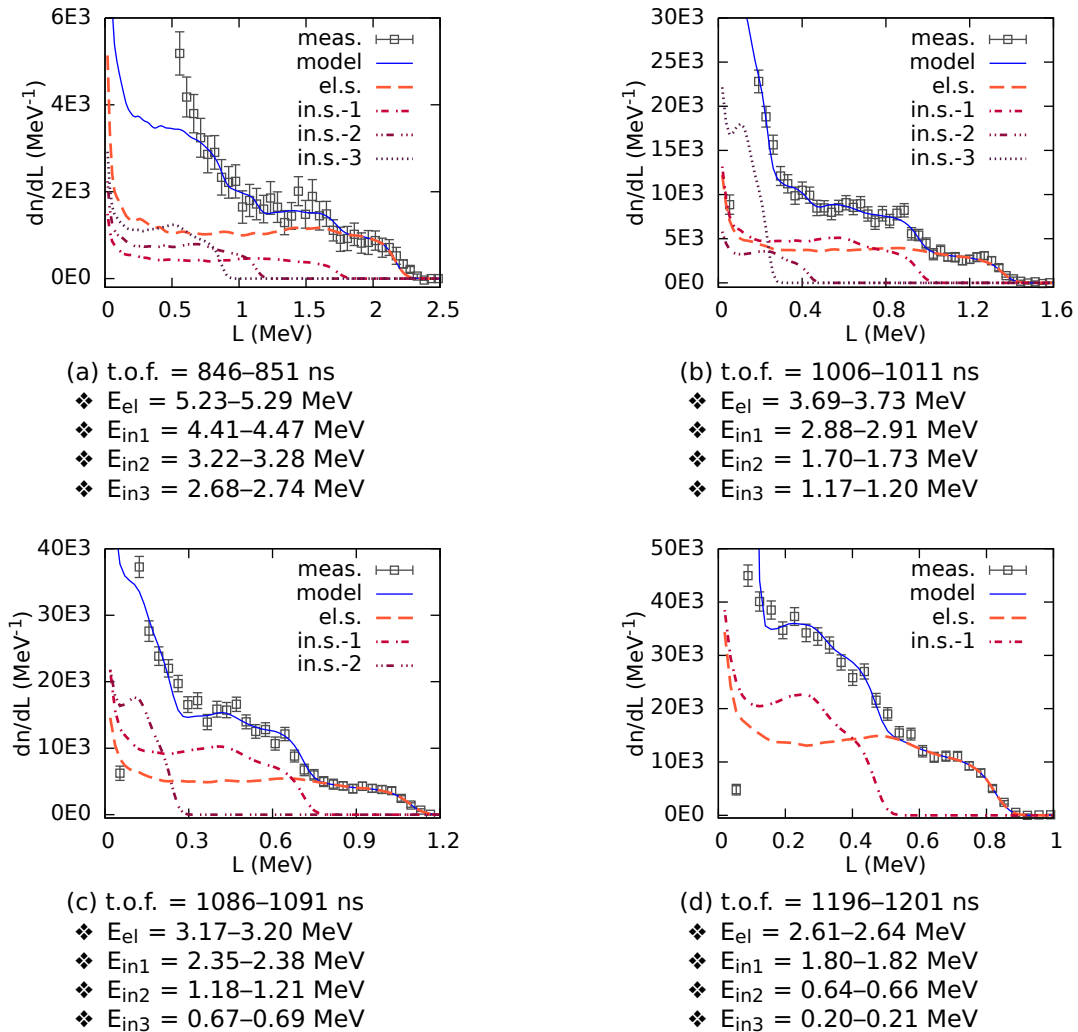
Figure 5.3: Experimental light output histograms ("data") measured with an EJ301 detector at 100.6° at GELINA (27 m flight path), compared to the simulated detector responses ("model"). The model represents the sum of the contributions of elastic scattering ("el.s."), and inelastic scattering from the first, second and third excited state of iron ("in.s.-1", "in.s.-2", and "in.s.-3"). Below each figure, the t.o.f. interval, and the corresponding neutron energies after an elastic ("*el*") or inelastic collision ("*in*1", "*in*2", and "*in*3") are indicated. The detection threshold for this detector is 60 keV in electron energy, or 540 keV in neutron energy.

(a) t.o.f. = 846–851 ns
- ❖ E_{el} = 5.23–5.29 MeV
- ❖ E_{in1} = 4.41–4.47 MeV
- ❖ E_{in2} = 3.22–3.28 MeV
- ❖ E_{in3} = 2.68–2.74 MeV

(b) t.o.f. = 1006–1011 ns
- ❖ E_{el} = 3.69–3.73 MeV
- ❖ E_{in1} = 2.88–2.91 MeV
- ❖ E_{in2} = 1.70–1.73 MeV
- ❖ E_{in3} = 1.17–1.20 MeV

(c) t.o.f. = 1086–1091 ns
- ❖ E_{el} = 3.17–3.20 MeV
- ❖ E_{in1} = 2.35–2.38 MeV
- ❖ E_{in2} = 1.18–1.21 MeV
- ❖ E_{in3} = 0.67–0.69 MeV

(d) t.o.f. = 1196–1201 ns
- ❖ E_{el} = 2.61–2.64 MeV
- ❖ E_{in1} = 1.80–1.82 MeV
- ❖ E_{in2} = 0.64–0.66 MeV
- ❖ E_{in3} = 0.20–0.21 MeV

Figure 5.4: Same as figures 5.3, but for an EJ315 detector. The detection threshold for this detector is 90 keV in electron energy, which corresponds to 655 keV in neutron energy.

For $LV = 0$, the area of $R(L, E'_0)$ is determined by the fit to the experimental light output distribution $N_{meas}(L)$ in the interval from $L_{THR,0}$ to $L_{MAX,0}$. For all other levels $LV > 0$, the function $R(L, E'_{LV})$ is fitted in the interval from $L_{THR,LV}$ to $L_{MAX,LV}$ to $N_{meas}(L) - \sum_{i=0}^{LV-1} R_{fit}(L, E'_i)$, where R_{fit} is the result of the fit performed for the underlying levels.

In figures 5.3 and 5.4, the results of this fitting procedure applied to the first three excited states are shown. For two detectors at 100.6° (an EJ301 and an EJ315), the light output spectra obtained for four different t.o.f. intervals are shown. All intervals correspond to incident energies above the threshold for inelastic scattering from the third level. However, in the distributions corresponding to the longest times (5.3c, 5.3d, 5.4c and 5.4d), neutrons scattering from the third and the second levels are either below the detection threshold (e.g. for the third level, figure 5.3d or 5.4d), or just slightly above it (figure 5.3c or 5.4c), so they could not be properly estimated. For the first level, for example, the contribution of inelastic reactions could be separated from that of the elastic reaction only starting from about 1.5 MeV neutron incident energy on iron. Because of this, the cross section could not be assessed close to the inelastic scattering threshold (862 keV for the first level).

In general, the model replicates well the experimental data, except in some cases with the EJ315 detectors (e.g. figure 5.4d). The discrepancies, which were noticed also when analysing the carbon measurements, vary with the neutron energy and affect in particular the low part of the light output histogram, so they are particularly problematic for the determination of the inelastic scattering yields. On this ground, the uncertainties are expected to be higher for the inelastic scattering cross section and angular distribution measured with the EJ315 detectors.

If $\varepsilon|_{L_{THR,LV}}$ is the detection efficiency corresponding to the threshold $L_{THR,LV}$, $\Delta\Omega$ is the detector opening angle, and F_{msc} the fraction of multiple scattering events, then the expression:
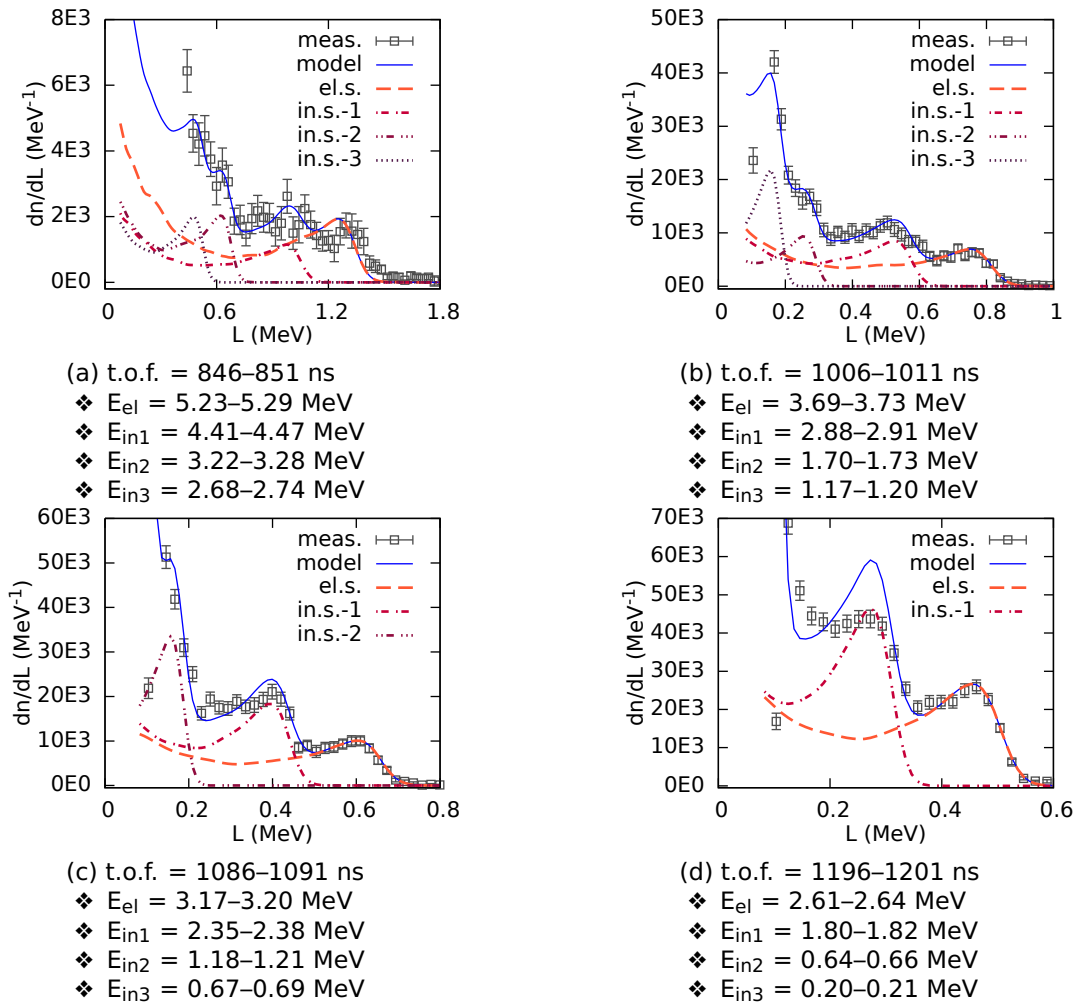
$$Y_{LV}(t.o.f., \theta) = \frac{1 - F_{msc}(t.o.f., \theta)}{\varepsilon(E'_{LV})|_{L_{THR,LV}} \Delta\Omega} \int_{L_{THR,LV}} R_{fit}(L, E'_{LV}) \, dL \tag{5.1}$$

gives the number of neutrons scattering from the level LV as a function of the neutron incident energy E_{LV} and the scattering angle θ ($Y_{LV}(t.o.f., \theta) = Y_{LV}(E_{LV}, \theta)$ because only single scattering events are considered). The differential cross section can be determined applying equation (4.5), and the angle integration is performed for each level separately according to the quadrature rule (2.7).

5.3 Elastic scattering

The differential cross section of elastic scattering on natural iron obtained in the two experiments at GELINA and nELBE is shown in figures 5.5 and 5.6. In figure 5.5, the differential cross section is represented as a function of the scattering angle cosine for 10 different energy bins, chosen to compare the results of the two experiments at GELINA and nELBE with the already existing measurements (see table 5.4). The experimental points are also compared with the CIELO evaluation. In figure 5.6, the results are presented by angle, as a function of the energy. The angle integrated cross section is shown in figure 5.7. Also in this case, the results are compared with other measurements (figure 5.7a) and the CIELO evaluation (figures 5.7b and 5.8). The cross section is presented in the incident neutron energy range from 2 MeV to 6 MeV: the carbon experiment proved that the results below 2 MeV are unreliable, and above 6 MeV the statistical fluctuations were such that the uncertainties amounted to almost 50% of the measurement.

The results of the two experiments at GELINA and nELBE are compatible with each other over the whole energy range. The nELBE and GELINA datasets are so close to each other, that it is reasonable to presume that the systematic uncertainties are caused by the data analysis, mostly by the uncertainties on the detector response determination, rather than by the instrumentation inaccuracies.

The uncertainties on the differential cross section range from 20% to 40% for the measurements at GELINA and from 20% to 50% for nELBE. In both cases the highest uncertainties

are found at backward angles for energies above 5 MeV, where statistics is low due to the physics of the process. Elastic scattering on iron is a strongly forward-peaked reaction: there is almost one order of magnitude difference between the differential cross section at the most forward angle (16.2°) and the angles larger than 60° (79.4°, 100.6°, 121.7°, 142.8°, and 163.8°). The only way to reduce the uncertainties at those angles would be making longer measurements.

For the angle-integrated cross sections, the uncertainties vary between 10% and 14% for GELINA, and between 10% and 18% for nELBE. The difference between the two datasets depends on the irradiation time, which was shorter in the case of nELBE.

The agreement with the other existing experimental results and the CIELO evaluation is good between 3 MeV and 4 MeV, and overall (admittedly, barely) within the uncertainty limits. In figure 5.8, where the comparison with the evaluation averaged according to the experimental energy resolution is shown, it is possible to notice how measured and evaluated cross sections are characterised by the same structures. However, the GELINA and nELBE datasets are systematically higher. The first impression is that of an underestimate of the normalization of the experimental cross section. If the normalization procedure were the cause, the same would have been observed for carbon, but that were not the case; on the contrary, the experimental and standard cross section were found to be highly compatible. For the same reason, if the cause for this bias were indeed a systematic effect due the analysis, it would be most likely related to the specificity of the iron measurement, not the general method. This difference goes in the same direction as the results presented in [35], where it was suggested that the elastic cross section reported in the libraries should be higher. In [35], the discrepancy is 21% at 6 MeV. For the measurements here presented, however, it is not higher than 13%, and it is almost in the limit of the experimental uncertainties. Regarding the differential cross sections, this discrepancy can be observed at 58.3° (figure 5.6f) and to a lesser extent at 16.2° (figure 5.6h)
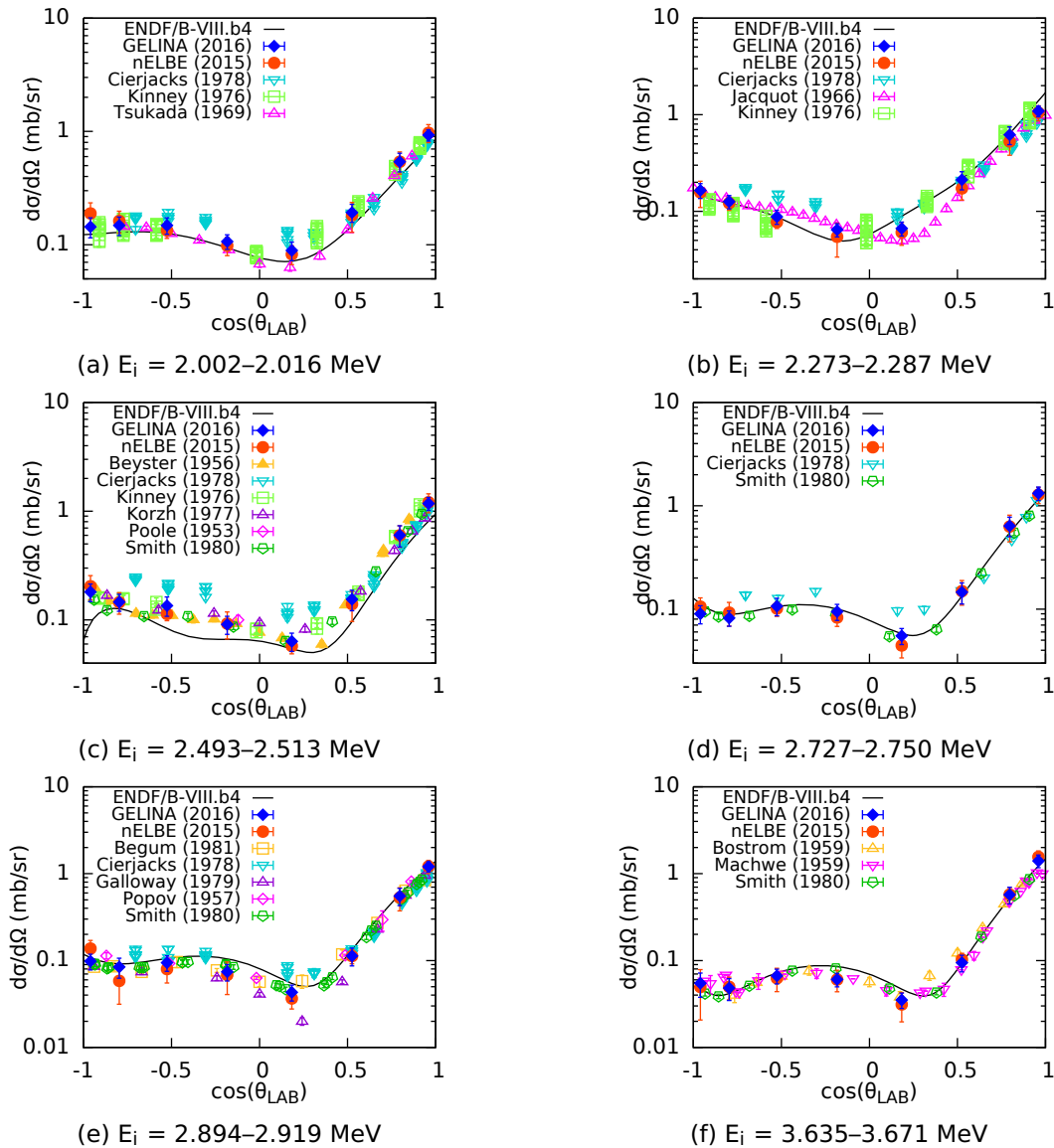
Figure 5.5: Differential cross section $d\sigma/d\Omega$ of neutron elastic scattering on natural iron as a function of the cosine of the scattering angle in the laboratory system θ_{LAB}, for selected intervals of incident neutron energy E_i. The results of the measurements at GELINA and nELBE are compared with the measurements from the EXFOR database and the angular distribution reported in the ENDF/B-VIII.b4 library (CIELO evaluation).

(g) E_i = 4.455–4.503 MeV

(h) E_i = 4.552–4.601 MeV

(i) E_i = 4.973–5.030 MeV

(j) E_i = 5.521–5.587 MeV
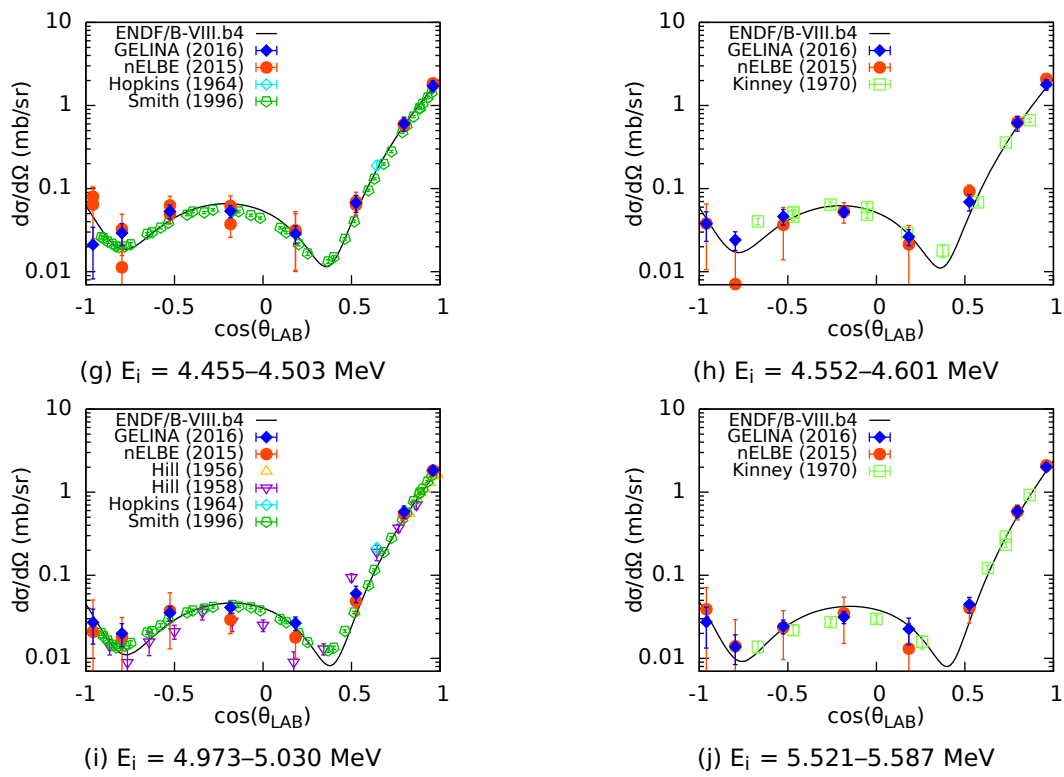
Figure 5.5: Continued from previous page.
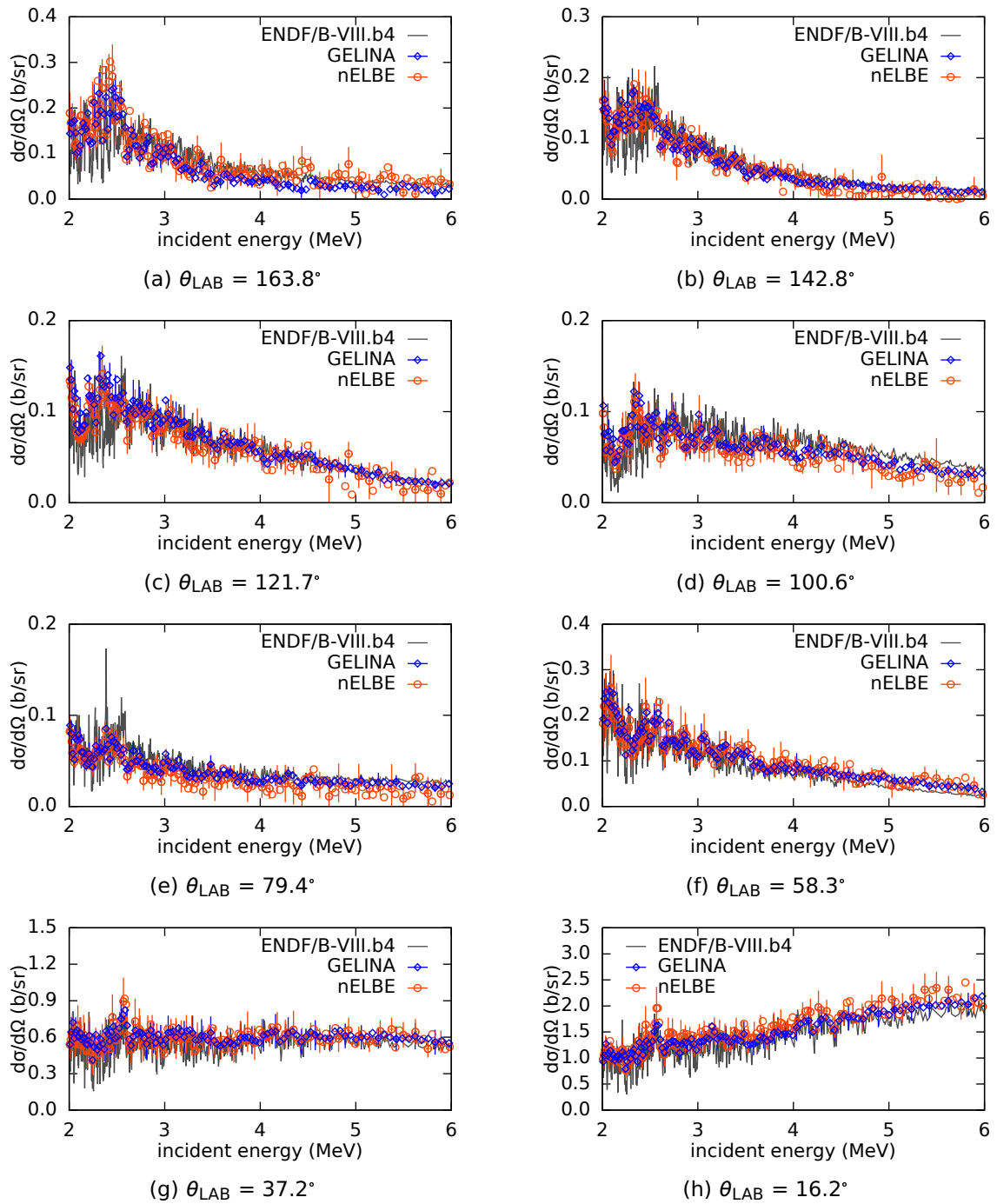
Figure 5.6: Differential cross section $d\sigma/d\Omega$ of neutron elastic scattering on natural iron as a function of the neutron incident energy: comparison of the measured values with the CIELO evaluation from the ENDF/B-VIII.b4 nuclear data library at the laboratory angles θ_{LAB}. To improve the readability of the graphs, the experimental uncertainties are given every three points.
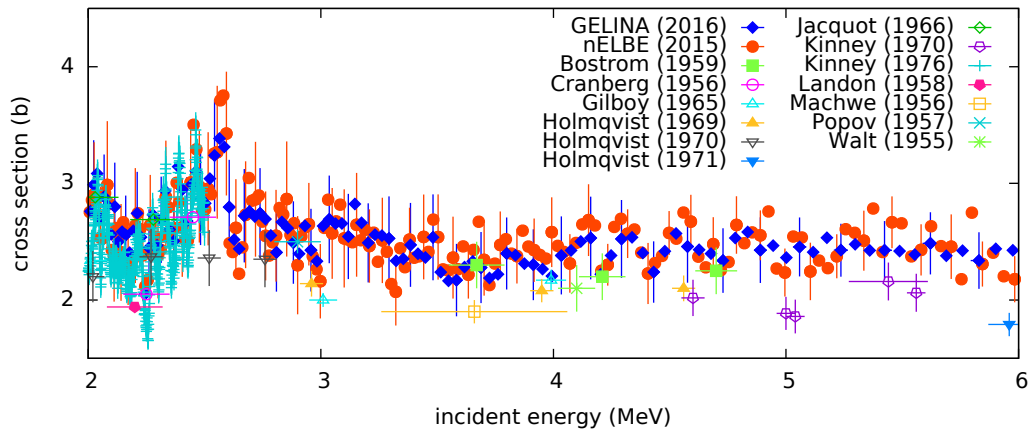
(a) Comparison with the experimental results available in EXFOR.
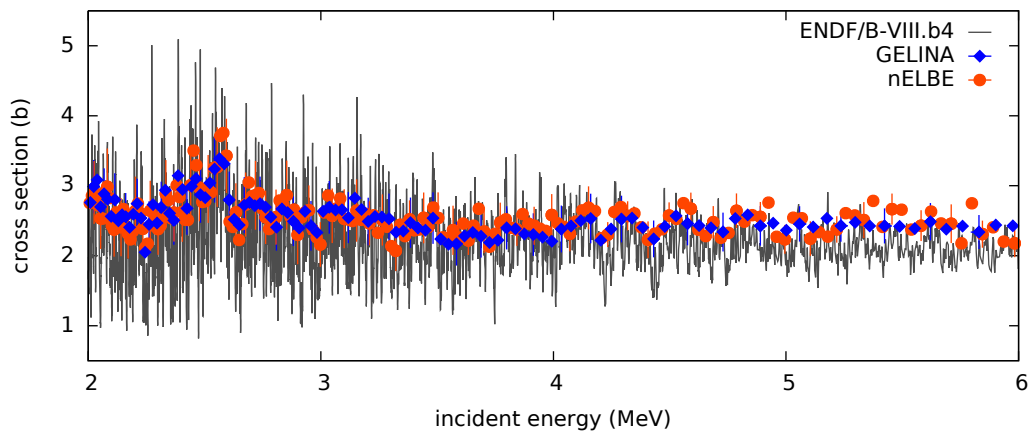
(b) Comparison with the CIELO evaluation.

Figure 5.7: Cross section of neutron elastic scattering on ^{nat}Fe as a function of the incident neutron energy: comparison of the values measured at GELINA and nELBE with other experiments from the EXFOR database and the CIELO evaluation from the ENDF/B-VIII.b4 nuclear data library. The uncertainties on the GELINA and nELBE datasets are given every three points to improve the graph readability.
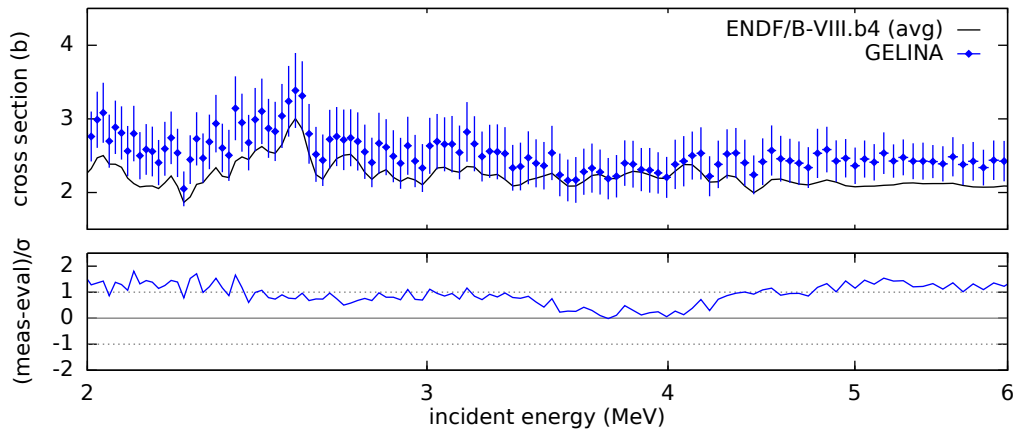
(a) Comparison with the GELINA dataset.
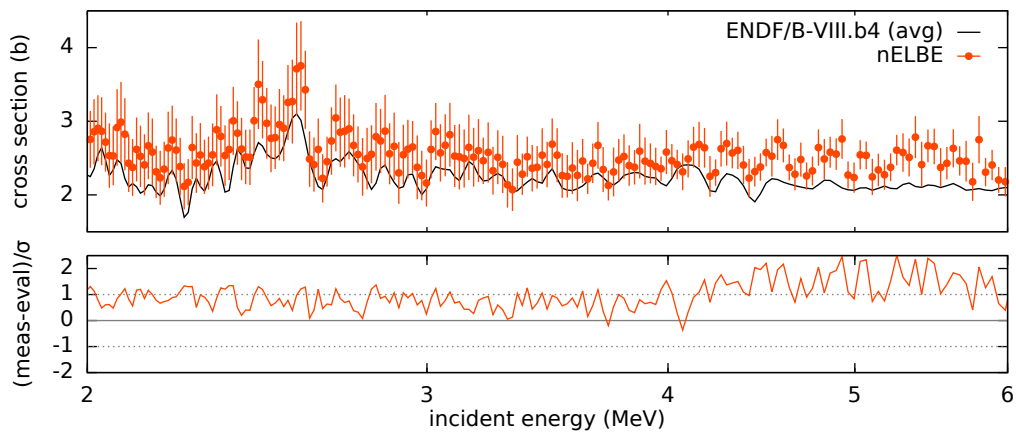
(b) Comparison with the nELBE dataset.

Figure 5.8: Cross section of neutron elastic scattering on ^{nat}Fe as a function of the incident neutron energy: comparison with the CIELO evaluation averaged according to the experimental energy resolution ("ENDF/B-VIII.b4 (avg)"). The deviation of the experimental data from the evaluated cross section is given as the difference between measurement and evaluation ($meas - eval$) divided by the experimental uncertainty (σ).

(a) GELINA measurement.   (b) nELBE measurement.

Figure 5.9: Differential cross section $d\sigma/d\Omega$ of neutron inelastic scattering from the first excited level of ^{56}Fe as a function of the neutron incident energy. The results obtained at 121.7° are shown for each detector separately (the scintillator type is indicated in the graph). The points are shown without uncertainties to improve the readability of the plot.

5.4   Inelastic scattering from the first excited state

The differential cross section of neutron inelastic scattering from the first excited level of ^{56}Fe is shown in figures 5.10 and 5.11. Similarly to the elastic scattering results, it is first represented as a function of the scattering angle cosine for 10 different energy intervals in figure 5.10. In figure 5.11, the results are presented by angle, as a function of the incident neutron energy.

The GELINA and nELBE results are overall compatible with each other. At 121.7°, however, below 3 MeV, the differential cross section measured at nELBE decreases with the neutron energy, while the cross section measured at GELINA remains more or less constant. The difference in the two trends is shown in figure 5.9, where the differential cross section is shown for each detector separately. The four datasets obtained at GELINA (figure 5.9a) are compatible with each other, while the two nELBE datasets (figure 5.9b) give discordant results for energies below 3 MeV. From the comparison between nELBE and GELINA, it seems that the problem has to be looked for somewhere in the analysis of the EJ315 detector data. The fact that the EJ315 cross section decreases with the energy (when it should not, or not to that extent), possibly indicates a problem with the determination of the efficiency as a function of the neutron energy. The efficiency however was determined in both experiments (GELINA and nELBE) in the same way and using the same parameters for the same detector. Therefore it is not clear what causes this trend, and the EJ315 data were not rejected because no reason was found to justify it. The large error bars on the nELBE differential cross section in figure 5.11c are the result of not being able to explain the different behaviour of the two detectors in figure 5.9b.

In general (the measurement at 121.7° included), the measurements at GELINA are affected by uncertainties that in most cases range from 20% to 50%, while for the nELBE data the uncertainties vary between 20% and 60%. The measurements are particularly problematic for the two most forward detectors, for energies above 4 MeV. This is because inelastic scattering is determined after the subtraction of the elastic scattering contribution. At forward angles, while the inelastic cross section decreases with the neutron energy, the elastic cross section keeps increasing. The predominance of elastic scattering becomes critical, for example, at 16.2° above 5 MeV: for this energy, the cross section of elastic scattering is two orders of magnitude higher than that of inelastic scattering. With the current statistics, the inelastic scattering events become indistinguishable; for this reason, in figure 5.11h, the experimental differential cross section above 5 MeV goes to zero. For the second-most forward angle (37.2°), the problem is similar: above 4 MeV, the uncertainties range from 40% to 100%. In general, the results at 16.2° and 37.2°, and also partially at

58.3°, are significantly higher than the other measurements (figure 5.10) and, accordingly, higher than the evaluation (figures from 5.11f to 5.11h). This is most likely an effect of the difficult separation between elastic and inelastic scattering. This is an indication that for the accurate determination of the inelastic scattering cross section higher statistics are needed. Moreover, a more sophisticated procedure for the separation of the various scattering components, such as proper unfolding of the scintillators light output distributions, might be necessary.

The overestimation of the differential cross section at the forward angles reflects also in the angle-integrated cross section, shown in figure 5.12a. The measurements at GELINA and nELBE are higher than any of the other measurements below 5 MeV. The difference is in this case a bit less accentuated because, when the Gaussian quadrature rule is applied, the most forward angles are weighted less than the central ones (see table 2.1). This issue poses nevertheless a limit on the final results: currently, for inelastic scattering, only partial angular distributions can be produced.

To verify the idea that the discrepancies are caused by the most forward measurements only, a correction was implemented, based on the approximation that the angular distributions are isotropic at all angles. If this is true, then the the values of the three most forward points may be replaced with the average of the backward values. The "corrected" angle-integrated cross section is shown in figure 5.12b). This correction is not particularly accurate, one could for example implement a correction based on the assumption of symmetry around 90°. It still provides some information on the angular distribution, such as indicating the limits for the isotropy assumption.
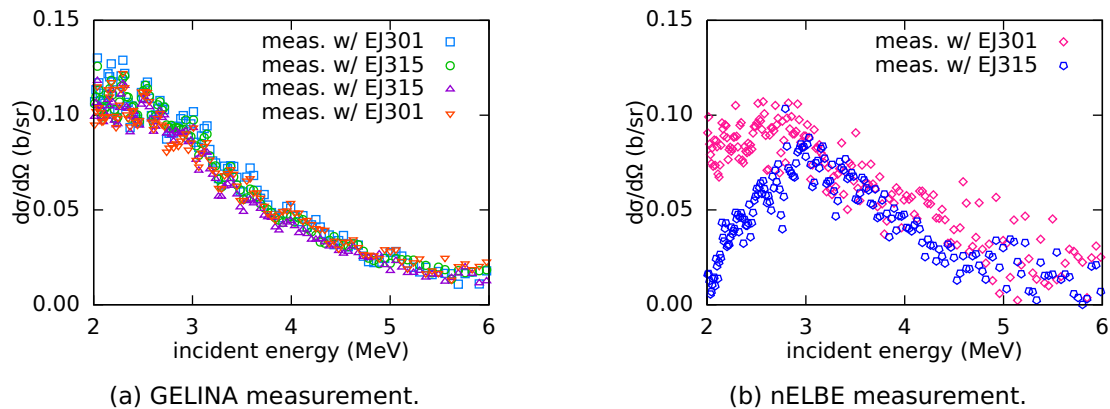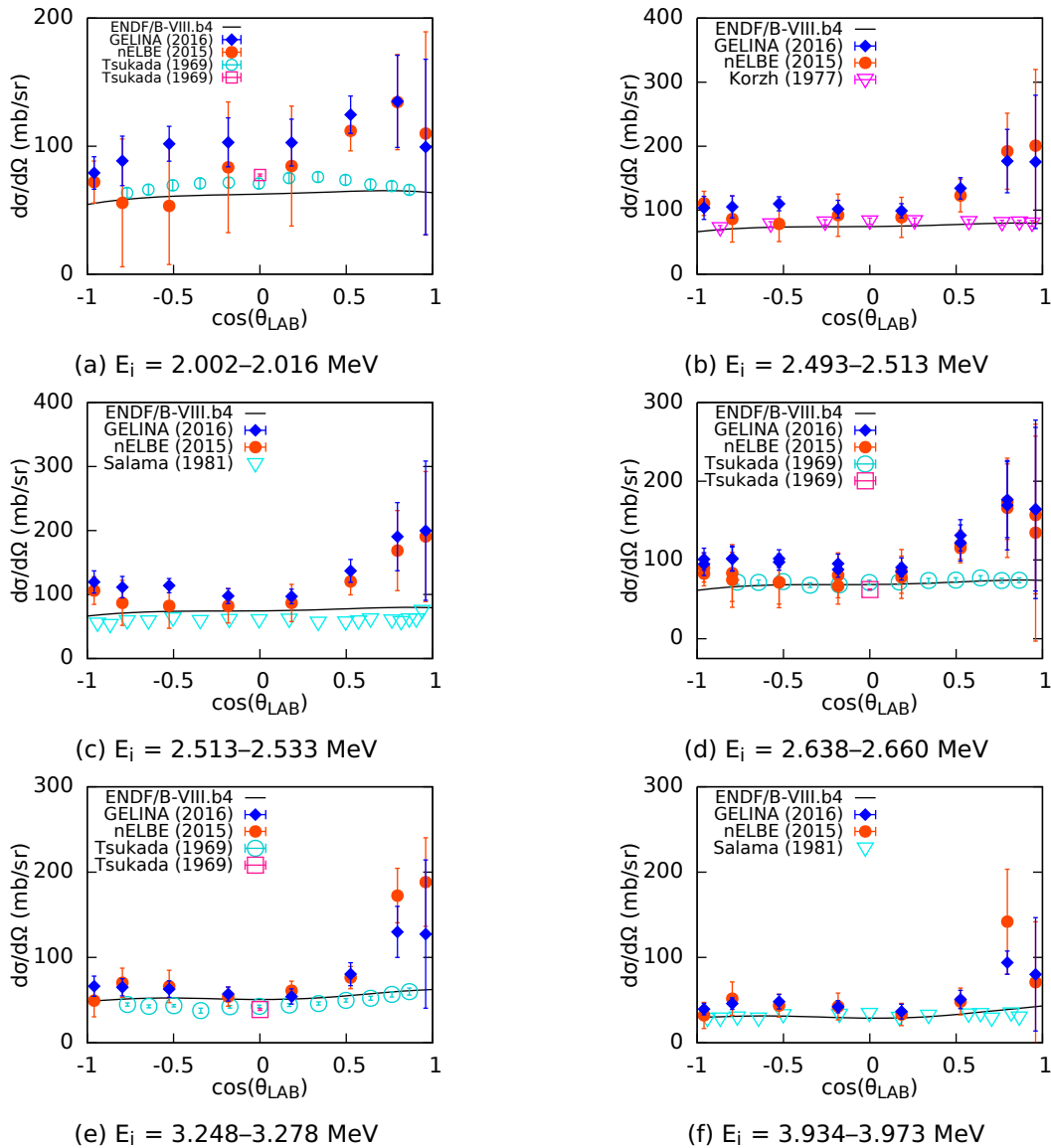
Figure 5.10: Differential cross section $d\sigma/d\Omega$ of neutron inelastic scattering from the first excited level of ^{56}Fe as a function of the cosine of the scattering angle in the laboratory system θ_{LAB}, for selected intervals of incident neutron energy E_i. The results of the measurements at GELINA and nELBE are compared with measurements from the EXFOR database and the angular distribution reported in the ENDF/B-VIII.b4 library (CIELO evaluation).

(g) E_i = 4.552–4.601 MeV

(h) E_i = 4.973–5.030 MeV

(i) E_i = 5.030–5.087 MeV

(j) E_i = 5.521–5.587 MeV
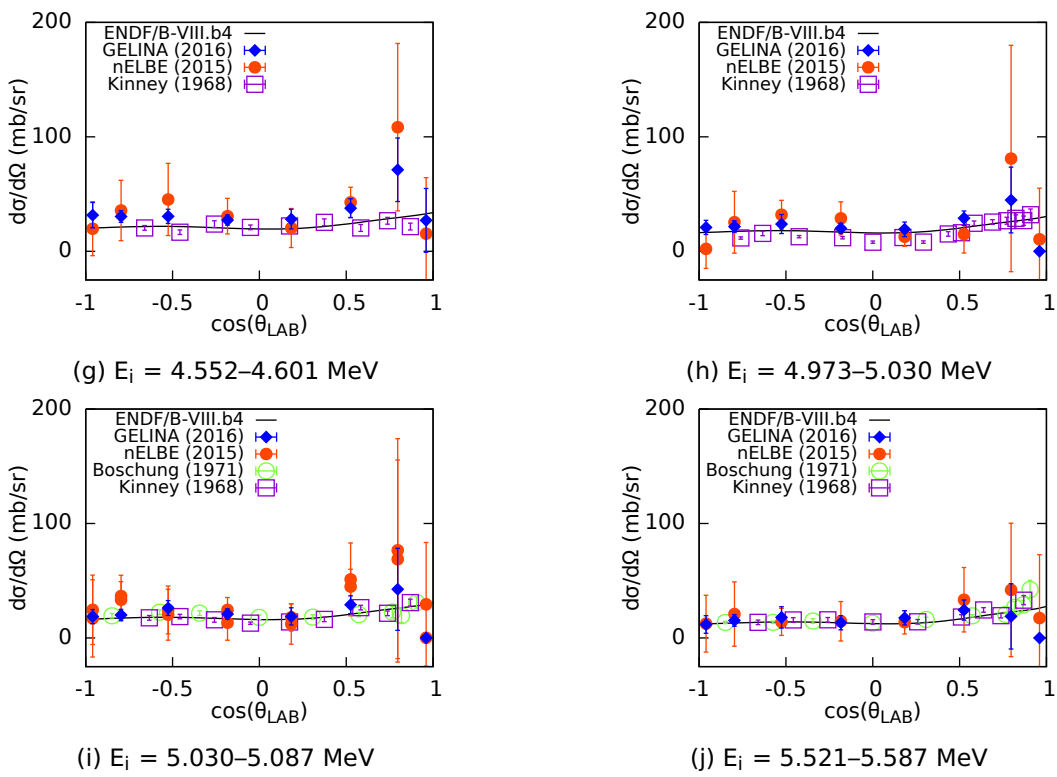
Figure 5.10: Continued from previous page.
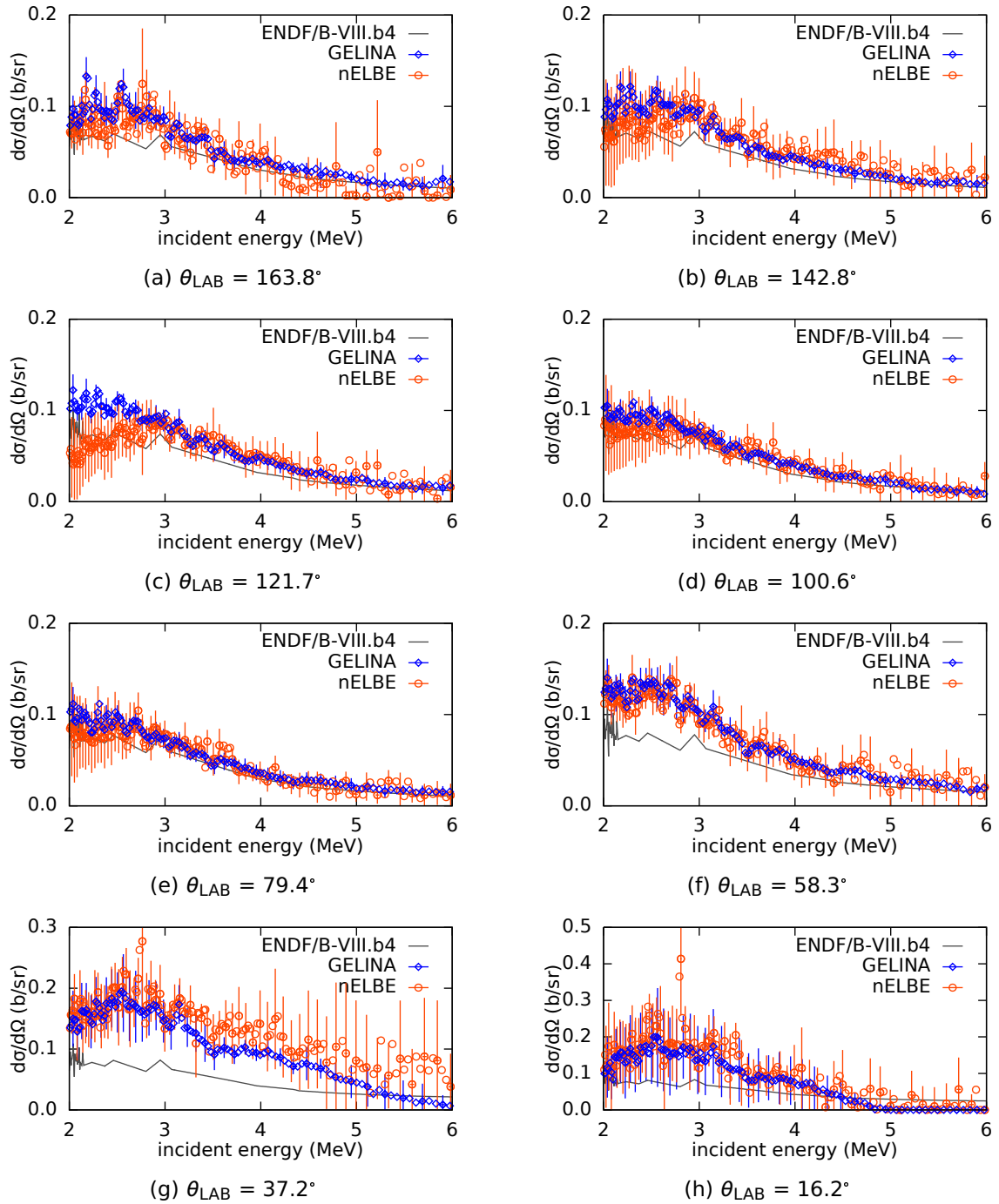
Figure 5.11: Differential cross section $d\sigma/d\Omega$ of neutron inelastic scattering from the first excited level of ^{56}Fe as a function of the neutron incident energy: comparison of the measured values with the evaluation from the ENDF/B-VII.1 nuclear data library at the laboratory angles θ_{LAB}. The experimental uncertainties are given every three points.
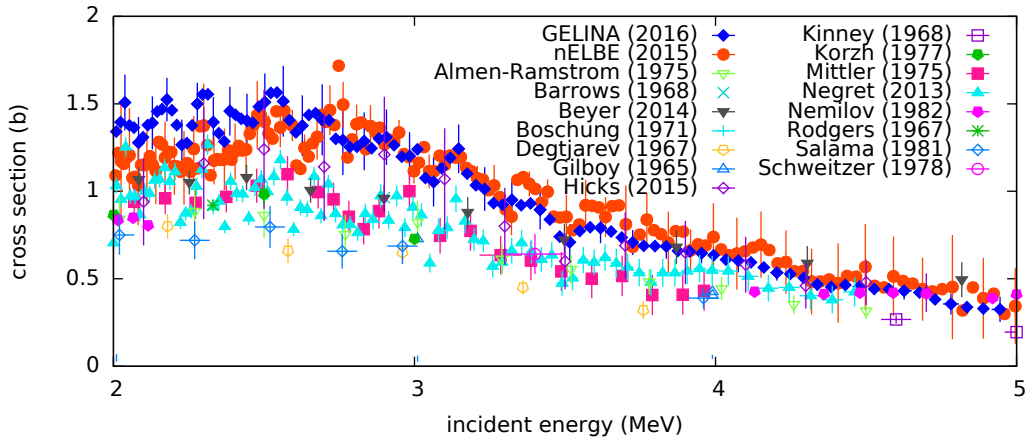
(a) Original results.
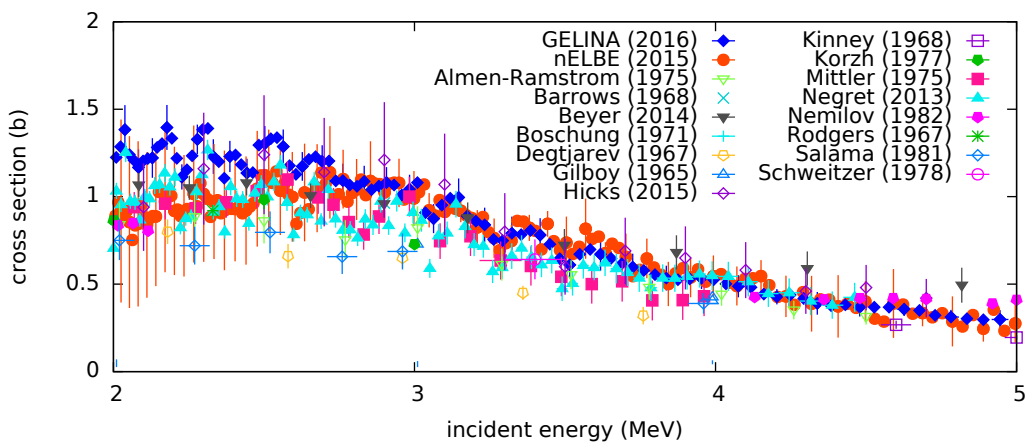
(b) Corrected data based on the isotropy assumption.

Figure 5.12: Cross section of of neutron inelastic scattering from the first excited level of ^{56}Fe as a function of the incident neutron energy: comparison of the values measured at GELINA and nELBE with other experiments from the EXFOR database. The experimental uncertainties on the GELINA and nELBE datasets are given every three points.

Backward-forward reaction asymmetry of neutron elastic scattering on deuterium

This chapter is the reproduction of a paper published in Physical Review C, volume 95, article 024601 (2017), coauthored with R. Beyer, A. R. Junghans, N. Nankov, R. Nolte, M. Nyman, and A. J. M. Plompen.

6.1 Introduction

Neutron scattering on deuterium is one of the simplest cases of the many body problem in nuclear physics and, as such, it is a valuable means of investigation of the fundamental interactions between nucleons. It is, moreover, a case study of practical interest for nuclear applications. In nuclear engineering, for instance, the interest mainly concerns the operation of heavy-water moderated reactors. In neutron metrology, the n-d scattering cross section is a necessary information as it determines the energy distribution of the D_2O-moderated ^{252}Cf fission neutron reference field, which is used for example for the calibration of neutron dosimeters [41]. In detector physics, the thorough knowledge of the reaction is crucial for the proper characterization of C_6D_6 scintillation detectors, whose response to neutrons depends indeed on n-d scattering [42].

The differential cross section of neutron elastic scattering on deuterium is an item in the High-Priority Request List of the OECD-NEA Data Bank for nuclear data measurements [34]. The request is motivated by the fact that the experimental angular distributions available in EXFOR [20] are scarce and partially inconsistent, particularly at angles near 180°, and the measurements are 25 to more than 50 years old [39]. Moreover, the energy-angle evaluated probability distributions have been found to cause inconsistencies when trying to reproduce the results of benchmark experiments for heavy-water moderated critical assemblies [19, 40].

In 2006, Townsend [39] reviewed the experimental n-d cross section data in the energy range relevant for fission reactions and the ENDF/B-VI.8 [141], JENDL-3.3 [142], and JEFF-3.1 [143] evaluations. The total elastic cross sections in ENDF/B-VI.8 and JEFF-3.1 were found to be identical, with JENDL-3.3 differing from them by less than 1%. However when angular distributions were considered, significant inconsistencies were noticed, particularly at backwards angles. In the range from 220 keV to 3.2 MeV the evaluations were compared to the experimental differential cross section, but an overall poor agreement was found.

In 2002 Canton *et al.* studied the consequences of introducing in the three-nucleon potential the irreducible effects generated by the one-pion-exchange mechanism [28]. They presented the theoretical predictions of the cross section and other observables of the nucleon-deuteron scattering in the energy range from 3 to 19 MeV. In 2007 Svenne *et al.* extended these calculations further down to 50 keV [144], and used the resulting differential cross section to provide additional information to compare to existing datasets the ENDF/B-VII.0 [145] and JENDL-3.3 libraries. Their results were found to have a better agree-

ment with JENDL-3.3, while the biggest difference with ENDF/B-VII.0 was found at backward angles.

More recently, the nucleon-deuteron scattering has been studied in the framework of effective field theory (EFT) [29, 37, 38]. In these works, the n-d scattering has been mainly used as means of validation of the three-nucleon potential derived via chiral perturbation theory applied to low-energy quantum chromodynamics. In [38], for instance, Golak *et al.* computed the three-nucleon forces at the fourth order (next-to-next-to-next-to the leading order, N3LO) of the expansion, and applied the full N3LO Hamiltonian to n-d elastic scattering and breakup reactions. For incoming nucleon energies below 20 MeV, discrepancies were observed between the EFT predictions of the spin observables and the experimental data. However, for the elastic scattering angular distribution in the same energy range, the effects of the three-nucleon forces were found to be negligible (see also [29]), and the theory agrees well with the data.

Since the n-d scattering total cross section is already well known, the present work focused only on the study of the backward-forward asymmetry of the reaction. The results are here presented of an experiment where the cross section ratio between the laboratory angles of 165° and 15° was determined. The aim was to provide a comparison between the main nuclear data libraries, theoretical calculations and new experimental data, therefore the two angles 165° and 15° were chosen in order to maximize the difference between evaluations.

The following libraries were considered: BROND-2.2 [146], CENDL-3.1 [15], JEFF-3.2 [12], JENDL-4.0 [14], ENDF/B-VII.1 [13] and ROSFOND-2010 [17]. All evaluations but ROSFOND-2010, which is based on ENDF/B-VI.3, result from independent analyses. CENDL-3.1, JEFF-3.2 and JENDL-4.0 are based on three-body models and the solution of the Faddeev equation; in ENDF/B-VII.1 the elastic angular distributions are the results of a coupled-channels *R*-matrix analysis.

In the experiment, performed at the nELBE neutron time-of-flight facility [147,148], neutrons scattered from a deuterated polyethylene (CD_2) sample were directly detected using lithium-6 enriched glass scintillators. As energies of interest range from a few hundred keV to few MeV, detectors such as organic scintillators, e.g., NE213 detectors, that use scattering on hydrogen as conversion reaction for neutron detection, were not considered suitable because of the strong quenching of the scintillation efficiency for neutron energies below 1 MeV and the related decrease of the efficiency for a given detection threshold. However, because of the low detection efficiency, it was necessary to have more than one detector at the selected positions, so in practice it was not possible to consider more than two angles.

A similar experiment was already attempted once before [149], but the amount of background due to room return neutrons made the analysis difficult and the poor statistics resulted in large uncertainties. After the enlargement of the nELBE experimental hall, the measurement was repeated, and with the room background significantly decreased it was possible to cover the energy range from 200 keV to 2 MeV.

6.2   Experimental setup

nELBE is the neutron time-of-flight facility installed at ELBE, the superconducting Electron Linac for beams with high Brilliance and low Emittance of the Helmholtz-Zentrum Dresden-Rossendorf [54, 55]. At nELBE [45], neutrons are produced by an electron beam impacting on a liquid lead target, via (γ,n) reactions induced by bremsstrahlung. Since the neutrons are emitted almost isotropically while the bremsstrahlung is forward peaked, the neutron beam is defined by a collimator: a steel tube with lead and polyethylene inserts, installed at 95° with respect to the primary electron beam. Different absorbers can be set up in front of the collimator in order to adjust the beam properties, such as the γ-flash intensity. In this experiment, 3 cm of lead were used. The experimental hall is separated from the neutron radiator by a 2.5 m thick wall of heavy and normal concrete, and the detector setup is located at least at 3 m from the walls, the ceiling and the floor.

The setup used for the experiment is shown in Fig. 6.1 and schematized in Fig. 6.2. Eight
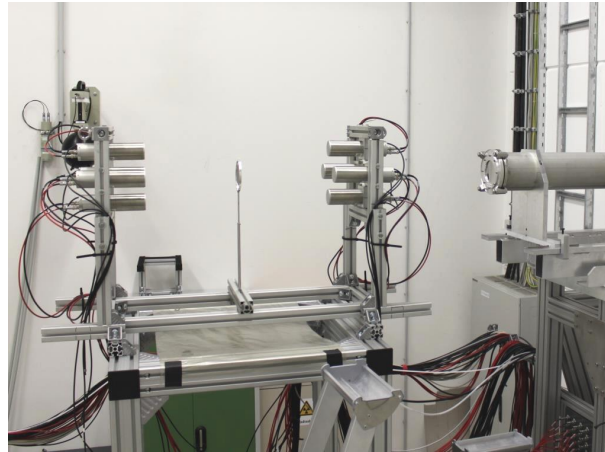
Figure 6.1: Picture of the detector array.
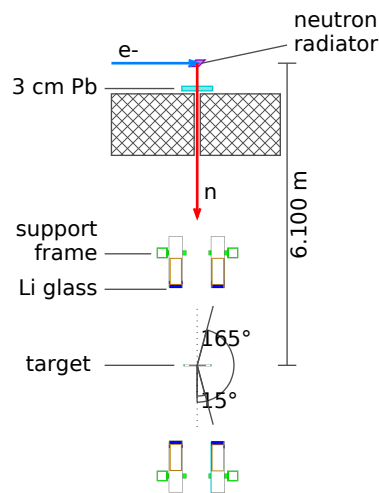
Figure 6.2: Diagram of the experimental setup (horizontal plane passing through the center of the target).

cylindrical lithium glass detectors enriched in lithium-6 from Scionix (model 51 B 12,7/2M-O-E1-LiG-Neg-X, see Table 6.1 for the specifics) were mounted on an aluminum frame, in two groups of four, at 165° and 15° to the beam axis. The sample was positioned in the middle of the frame centered on the beam axis, 6.100(1) m from the neutron source. Two different samples were used as targets: a deuterated polyethylene disk with 99.999% enrichment in deuterium, and a graphite disk which was used to assess the contribution of carbon in the CD_2 measurement. A measurement with the empty sample holder was also performed to determine the background due to neutrons scattering in air or in the supporting frame. The specifics of the samples and the position of the detectors are reported in Tables 6.2 and 6.3, respectively. A graphite sample three times thicker than the CD_2 target was chosen in order to avoid the problems encountered when carrying out the experiment the first time, when the measurements with a thinner carbon sample could not be used because of the amount of room return background.

The data acquisition (DAQ) system (diagram in Fig. 6.4) was based on commercially available VME modules read out by a CES RIO4 VME Power-PC running the real time operating system LynxOS and the DAQ software MBS developed by GSI Darmstadt [59]. The signal of each detector was split by a 50-Ohm-splitter and then fed to a charge-to-digital converter (QDC, type CAEN V965A) and a constant fraction discriminator (CFD, in house de-

Table 6.1: Lithium glass specifications by Scionix.

dimensions:	diameter	50.8 mm
	thickness	12.7 mm
composition:	SiO_2	56%
(% in weight)	MgO	4%
	Al_2O_3	18%
	Ce_2O_3	4%
	$^6Li_2O$	18%
lithium-6 content:	7.4% weight	
density:	2.5–2.7 g/cm^3	

Table 6.2: Physical properties of the samples.

	CD_2	graphite
diameter (cm)	7.00(2)	11.0(1)
thickness (cm)	0.30(2)	0.93(2)
areal density (g/cm^2)	0.3236(9)	1.52(1)
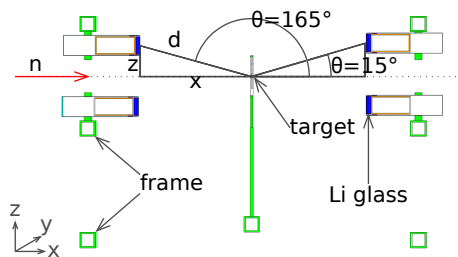
Figure 6.3: Model of the detectors, the target, and the supporting aluminum frame implemented in MCNP5. Here the vertical x-z plane passing through the center of the target is shown; an analogous figure is obtained when the x-y plane is plotted, with the difference that there the distance z is replaced by that along the y-axis. The distances x, y, and z were actually measured, d and the angle θ were computed accordingly. The exact values of x, y or z, d, and θ are reported in Table 6.3.

Table 6.3: Position of the detectors. The distances x, y, z, and d and the angle θ, defined as described in Fig. 6.3, refer to position of the center of the detector external housing's front face with respect to the beam axis or the center of the target. The angles covered by the whole front surface are in the range of ±4° the angle measured at its center.

x (mm)	$|y|$ or $|z|$ (mm)	d (mm)	$\cos\theta$	θ (°)
322(2)	86(1)	333(2)	0.9661(8)	15.0(2)
320(2)	92(1)	333(2)	0.9611(9)	16.0(2)
324(2)	87(1)	336(2)	0.9658(8)	15.0(2)
320(2)	88(1)	332(2)	0.9642(9)	15.4(2)
-327(2)	83(1)	338(2)	-0.9693(8)	165.8(2)
-327(2)	95(1)	340(2)	-0.9603(9)	163.8(2)
-328(2)	87(1)	339(2)	-0.9669(8)	165.2(2)
-328(2)	92(1)	341(2)	-0.9629(9)	164.3(2)
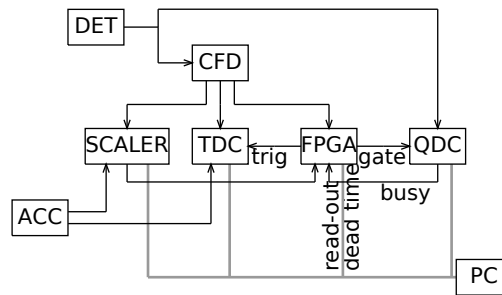
Figure 6.4: Diagram of the data acquisition system. DET: Li-glass detector; ACC: accelerator reference signal; CFD: constant fraction discriminator; FPGA: field programmable gate array logic module; QDC: charge-to-digital converter; TDC: time-to-digital converter; SCALER: scaler module.

velopment of HZDR). The output of the CFD was fed to a scaler (realized by an FPGA module type CAEN V1495), a time-to-digital converter (TDC, type CAEN V1290A) and a trigger logic module (implemented in a second FPGA module type CAEN V1495). The latter generated the trigger for both the QDC and the TDC, and accomplished the dead time logic. The TDC gathered the signals from both the detectors and the accelerator reference signal, determining in this way the time of flight (t.o.f.). The dead time of the DAQ system, i.e. the time needed for the analog-to-digital conversion of the signals and the read-out of the buffer memories, was determined integrally by the scaler and per event by the trigger logic, using a VETO signal that was the logical OR of the busy signals of all electronic modules. Thereby a t.o.f. dependent dead time correction could be applied using the procedure described in [45].

The present experiment did not aim at measuring the full angular distribution but only the backward-forward asymmetry at a selected pair of forward and backward angles. For this reason and because the relative neutron energy distribution was already determined previously using a ^{235}U fission chamber [45], a precise flux determination was not required. To compare the runs with different targets and the "sample-out" run, the relative beam fluence was derived from the total counts of a plastic scintillator installed downstream with respect to the setup. The scintillator is mainly sensitive to scattered photons, therefore its counting rate depended on the sample in place at a given moment. The differences were quantified by assuming that the beam flux would remain constant during the time needed to change or remove the sample. This was deemed reasonable because the accelerator current, measured continuously upstream, was notably stable during the whole experiment, and the procedure to change target needed about half an hour to be completed. Therefore, the difference in the counting rate of the monitor at the end of one run and the beginning of the following was caused only by the difference in the sample. The ratio between the two values was used to normalize the monitor counts of the graphite run and sample-out run to the CD_2 run.

6.3 Analysis of the time of flight spectra

In facilities such as nELBE, where an electron linac is used to produce neutrons, time of flight experiments are accomplished by operating the accelerator in pulsed mode and by measuring the elapsed time between the neutron production and their detection. In the case of ELBE, the electrons are produced in pulses of 5 ps width (FWHM) and kinetic energy up to 40 MeV; the repetition rate can reach up to 26 MHz, but for the production of neutrons it is typically set between 100 to 250 kHz [45] (101 kHz in this experiment).

In this experiment, the measured time of flight consisted of the sum of the time of flight

of the incoming neutron traveling from the source to the scattering target, and the time of flight of the scattered neutron going from the target to the detector. The relationship between time of flight (t.o.f.) and neutron energy before and after the collision (E and E') could then be expressed as:

$$\text{t.o.f.} = \frac{L}{c\sqrt{1 - \frac{1}{(1 + E/mc^2)^2}}} + \frac{L'}{c\sqrt{1 - \frac{1}{(1 + E'/mc^2)^2}}} \tag{6.1}$$

where c is the speed of light, m the neutron mass, L and L' the length of the flight paths, respectively, of the incident and scattered neutron. In case of elastic scattering on a given nuclide, the energy after the collision E' depends on the energy E and on the scattering angle θ. In fact, if m is the mass of the neutron, and M the mass of the target nuclide, then the conservation of energy gives, in case of an elastic collision in the laboratory frame of reference, the following expression:

$$E'(mc^2 + Mc^2) + E(mc^2 - Mc^2) + E'E = c^2pp'\cos\theta \tag{6.2}$$

where $p = \sqrt{E(E + 2mc^2)}/c$ and $p' = \sqrt{E'(E' + 2mc^2)}/c$ are the momentum of the neutron before and after the collision. Hence, Eq. (6.1) states a one-to-one correspondence between the time of flight measured with a fixed detector and the neutron initial energy. Equation (6.1) however works for neutrons that scatter one time only, and if the collision happens outside the target L and L' cannot be measured. Moreover, to be able to calculate E', the mass of the nuclide that was hit must be known. For this reasons, one of the main objectives of the data analysis was the separation of the events due to single scattering on deuterium from those due to, for example, multiple scattering, or scattering on carbon or in air.

6.3.1 Background subtraction

In the two-dimensional histograms shown in Fig. 6.5, the signals of two detectors, one at 15° and the other at 165°, were arranged according to the values given by the TDC and QDC modules, i.e., according to time and integrated charge. The absolute time of flight was obtained from the TDC values using the γ-flash as reference. In Fig. 6.5 the γ-flash is the sharp structure at the TDC channel 840 which corresponds to the time of flight of light $(L + L')/c$. The QDC values, proportional to the energy deposited in the active volume of the scintillator, were used to discriminate between neutron and photons. The lithium glass scintillators detect neutrons via the ^{6}Li(n,α)^{3}H reaction, and the relatively large Q-value of 4.78 MeV allows to discriminate neutron induced events from photon induced or other low-amplitude events by applying a proper gate on the charge. In the two examples in Fig. 6.5, the neutron events are those with QDC channel > 90 and TDC channel > 1100. The structure that can be noticed just after the TDC channel 1000 is most likely due to photons from inelastic scattering on carbon; the time of flight and the Monte Carlo simulations of the experiment are consistent with this explanation.

After applying proper time and charge conditions on the raw TDC-QDC matrices in order to separate the neutron events, their projections on the time axis, the t.o.f. histograms, still include a number of background events due to room return neutrons or neutrons detected after scattering in air or in the aluminum frame. As the room return background is independent from the time of flight, i.e., constant in time, it could be easily determined by averaging the counts in the t.o.f. intervals before the γ-flash and after the neutron burst. Figure 6.6 shows an example of two t.o.f. histograms after the subtraction of the time-independent component of the background.

After that, the time-dependent background component was estimated by rescaling the sample-out t.o.f. histogram with the monitor counts and then subtracting it from the CD_2 and carbon measurements. The net spectra obtained after the background subtraction still had to be corrected for the multiple scattering inside the sample, and this was determined by means of a Monte Carlo model of the experiment.
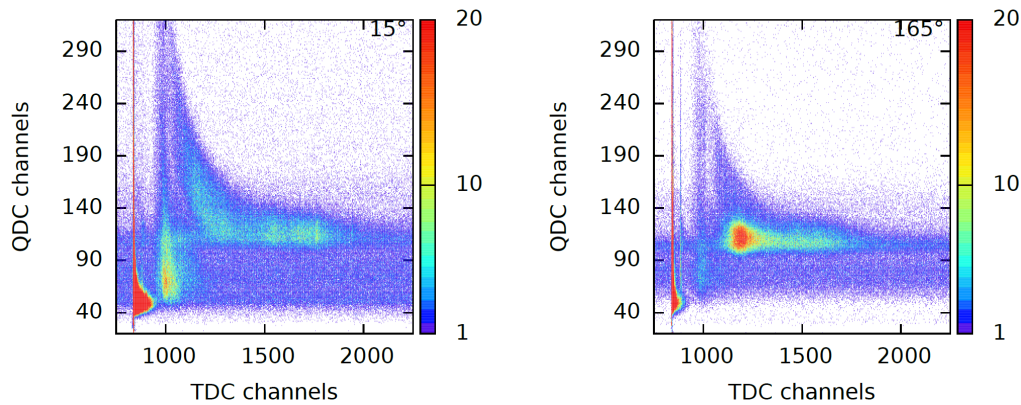
Figure 6.5: Example of raw data. The two-dimensional histograms show the counts as a function of the TDC time and QDC integrated charge recorded in almost 70 h of beam time, with the CD_2 sample as neutron scatterer, from one of the detectors at 15°and one at 165°.
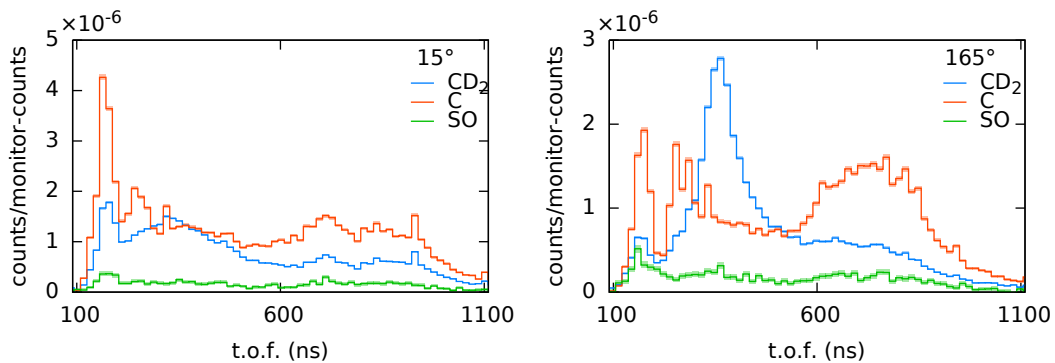
Figure 6.6: Example t.o.f. histograms, one for a detector at 15° and one at 165°, after the room background subtraction. The counts have been normalized with the monitor counts for proper comparison between the CD_2, sample-out (SO) and graphite (C - carbon) measurements.

6.3.2 Multiple scattering

In the model, implemented in MCNP5 [71] (see Fig. 6.3 for the geometry), the CD_2 or graphite target and the detectors were placed in vacuum and, for the neutron source, the energy distribution measured previously in the same experimental configuration was used. The average neutron flux and the rate of the $^6Li(n,\alpha)^3H$ reaction were tallied over the lithium glass volume as a function of the time of flight. Using the "PTRAC" option it is possible to follow every history event by event, and this was used to determine the percentage of neutrons arriving at a detector after single scattering on deuterium, carbon, hydrogen (negligible), or multiple scattering in the target (see Figs. 6.8 and 6.10).

Detector by detector, the simulation results were compared with the data, finding a good overall agreement. As it is possible to notice from the two example in Figs. 6.7 and 6.9, only for short t.o.f., ca. 110–200 ns, it was not possible to reproduce the data well. However when the photon flux over the detector's sensitive volume was tallied, its shape matched this part of the spectrum, so it is possible that those unrecognized events are photons misclassified as neutrons. Anyway, this does not really pose a problem, since for neutrons scattering on deuterium the t.o.f. corresponds to incident energies of about 18 MeV at 15° and 23 MeV at 165°, well beyond the range of interest.

For these simulations, all cross section libraries were from ENDF/B-VII. No other library was considered at this stage because the aim was to estimate the multiple scattering in
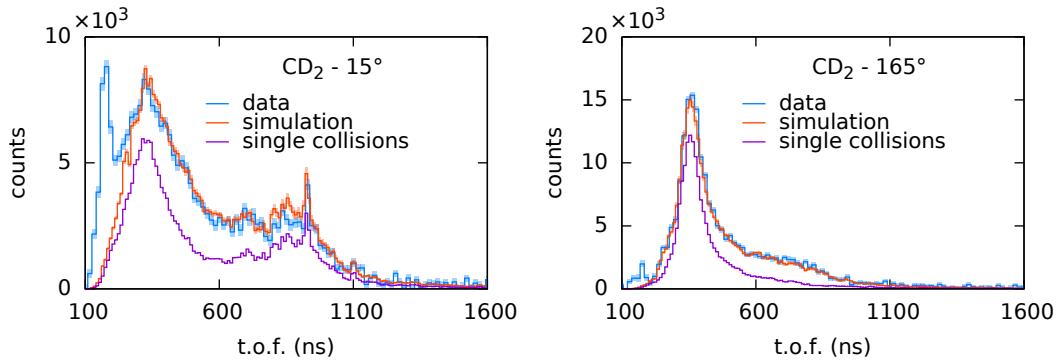
Figure 6.7: Experimental CD$_2$ t.o.f. histograms ("data"), at 15° and 165°, after the subtraction of the contribution of scattering in air, compared with the simulated ^{6}Li(n,α) reaction rate tallied in the detector sensitive volume ("simulation"). The "single collisions" lines are the simulation results when only neutrons arriving after a single collision on deuterium are considered.
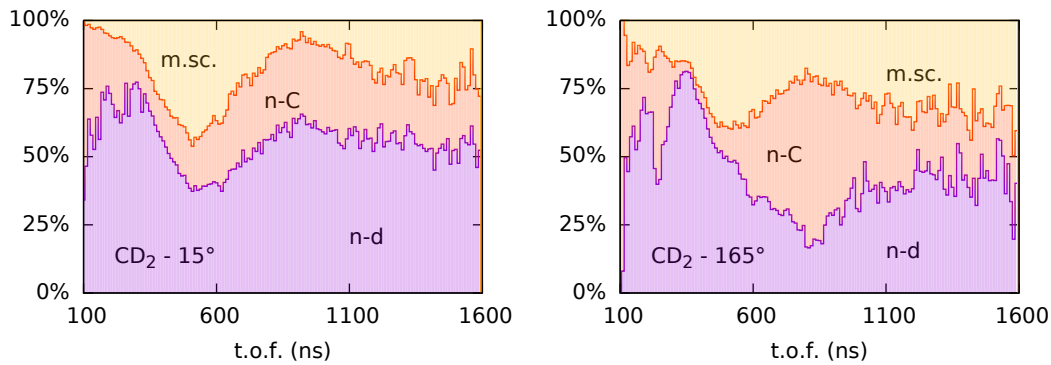
Figure 6.8: Contribution of multiple scattering in the target ("m.sc."), single scattering on deuterium ("n-d") or on carbon ("n-C"), expressed in percentage of number of events as a function of the time of flight.

the target, not to appraise different evaluations.

Without a measurement of the neutron flux model and experiment cannot be compared directly. Hence, the MCNP results were rescaled to the data by a constant factor, which was found by minimizing the difference between data and simulations with the linear least square method applied in the t.o.f. interval from 450 to 750 ns. This interval was defined in the attempt to find a region in the energy distributions with good statistics and small contribution of the multiple scattering component when compared to the single scattering.

In principle, the rescaling factor depends only on the incident flux, and thus can serve as parameter for a consistency check: if the detectors are all equivalent, the rescaling coefficient must be the same for all of them, independently from their position or the sample in place. It was computed assuming that the ratio between the counts at a given t.o.f. in the experimental histograms normalized by the monitor counts ($DATA(t.o.f.)$) and the ^{6}Li(n,α) events scored by MCNP for the same t.o.f. ($MCNP(t.o.f.)$) was constant, by the linear regression of the relation: $DATA(t.o.f.) = b \cdot MCNP(t.o.f.)$. The results of the regression for the parameter b, obtained for each detector and for each run with a different target (see Fig. 6.11), were consistent with each other. The arithmetic average of all values was therefore used to rescale the MCNP simulation to the data.

To investigate the accuracy of the model, the sample-out measurement was also reproduced (see Fig. 6.12). In this case, only the target holder was modelled and a cylindrical volume of air was positioned around the beam axis while the detectors were still in vacuum.
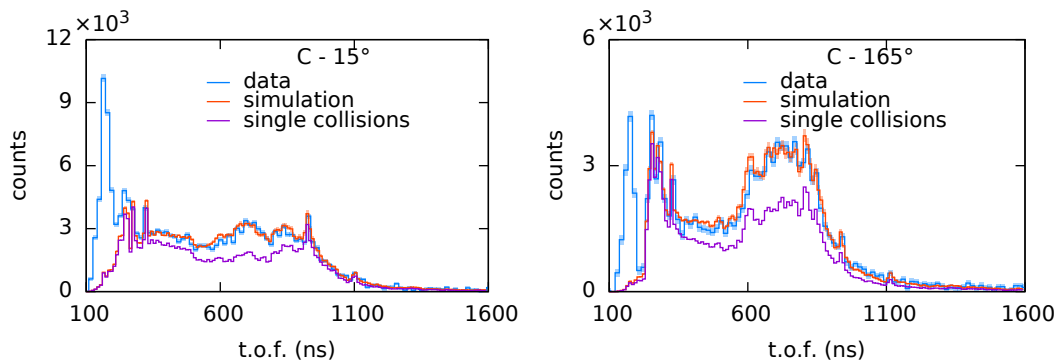
Figure 6.9: Same as Fig. 6.7 but for the carbon data. In this case the "single collisions" lines indicate the single collision on carbon.
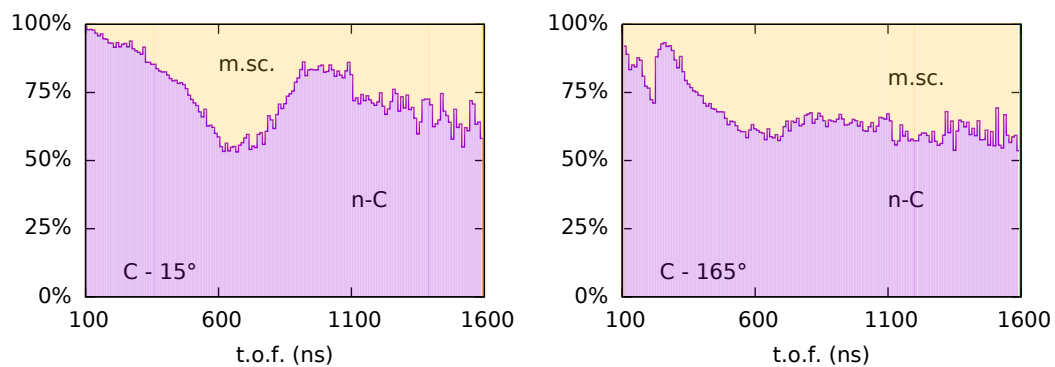
Figure 6.10: Same as Fig. 6.8 but for the carbon data.
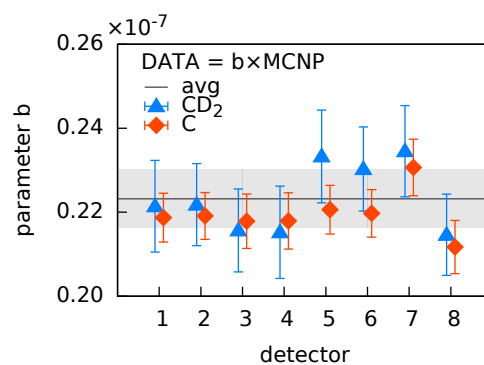
Figure 6.11: Rescaling factor for the MCNP results obtained for each detector (detectors at 15°: numbers 3, 4, 7, and 8; at 165°: 1, 2, 5, and 6), for the CD$_2$ and graphite (C) runs. The parameter b has an order of magnitude of 10^{-7} because the data were normalized by the monitor counts. The arithmetic average (avg) of all values is what was used to rescale the simulations to the data in Figs. 6.7, 6.9, and 6.12.
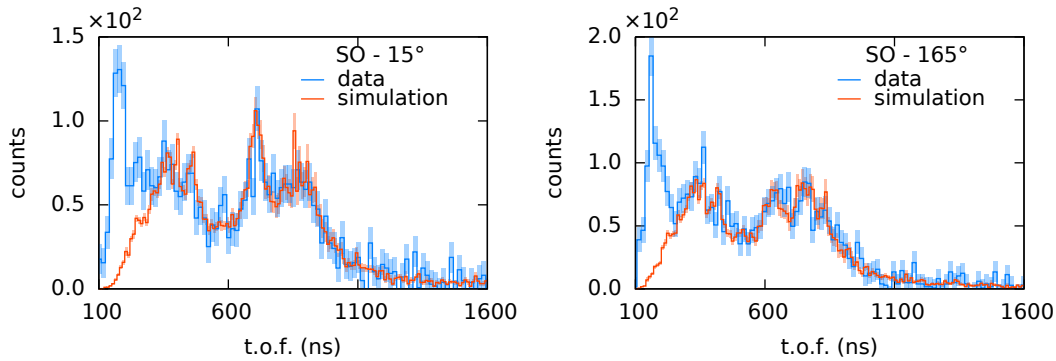
Figure 6.12: Experimental t.o.f. histograms ("data") for the sample-out run, at 15° and 165°, compared to the simulated ^{6}Li(n,α) reaction rate tallied in the glass volume ("simulation").

The outcome confirmed that the t.o.f. dependent background component, as measured in the sample-out measurement, mainly results from neutrons scattering once or twice in air before being detected.

It was also possible to prove that adding further details to the model (the aluminum frame, air in the whole room, the concrete walls) did not significantly change the results. Including the detector supporting structure, for example, led to a systematic increase in the number of ^{6}Li(n,α)^{3}H events tallied as function of the t.o.f. over the detectors' sensitive volume. At 2 MeV of neutron incident energy this increase amounted to 1% of the value obtained with the original model, at 500 keV it was 4%, and at 200 keV it was 5%. This contribution however was lower than the relative statistical uncertainties of the simulation, which ranged from 2% at 2 MeV to 7% at 200 keV. Also, it was regarded as negligible compared to the uncertainties on the experimental t.o.f. histograms, which went from 4% at 2 MeV to 20% at 200 keV. Modeling the concrete walls that delimited the experimental hall and filling the empty space with air caused a difference that fluctuated between -2% and 2% in the range from 1 to 2 MeV, and between -5% and 5% in the range from 200 keV to 500 keV. The combined effects of considering both the aluminum frame and the air-filled room varied between -2% and 2% at 1–2 MeV, -2% and 4% at 0.5–1 MeV, -5% and 7% at 0.2–0.5 MeV, always lying within the limits of the uncertainties.

6.3.3 Scattering on deuterium

Since the simulations allowed to assess the fraction of detected events happening after multiple scattering, the data were reduced to have only events due to single collisions in the target. At this point, knowing the areal density of both the CD_2 and graphite samples, the graphite t.o.f. spectra were multiplied by the ratio of the masses per unit area to determine and subtract the contribution of carbon from the CD_2 measurement. The spectra for single scattering on deuterium obtained after the subtraction are shown in Fig. 6.13, with the time of flight converted in neutron incident energy. The spectra of the detectors at the same angle are very similar and, therefore, the counts were summed together without further corrections.

The two total histograms at 15° and 165° cannot be directly compared because of the detection efficiency, which does not depend on the incident energy. Assuming all detectors are equivalent, the efficiency depends on the angle in the sense that for the same initial (incident) energy, neutrons scattered at 15° have a different final energy from those arriving at 165°, so a different probability of being detected.

The detection efficiency was determined analyzing the results of the simulation with the CD_2 target, the PTRAC file, a second time. Considering only the histories including one single n-d scattering event, the number of ^{6}Li(n,t)^{4}He events relative to the number of incoming neutrons and thus the detection efficiency were determined as function of the neutron energy E as it is before colliding with the target. This method was used in order
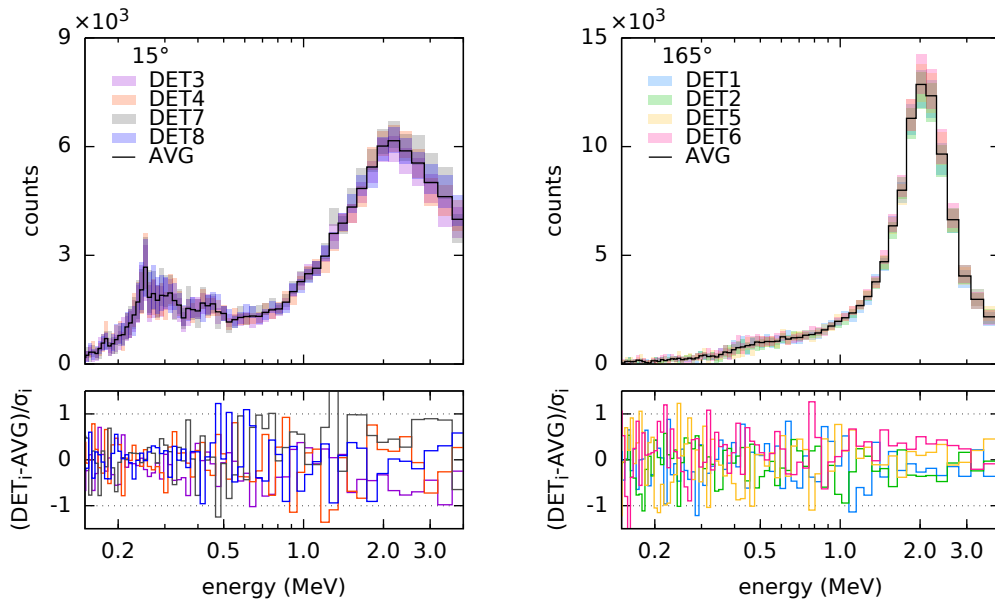
Figure 6.13: Single scattering on deuterium events at 15° and 165°, for every detector alone ($DET_i(E)$), and their average ($AVG(E)$), as a function of the incident neutron energy E. The deviation from the average, expressed as $(DET_i(E) - AVG(E))/\sigma_{DET_i}(E)$, where σ is the uncertainty on the measured events, is also plotted for each detector.

to be able to take automatically into account the full geometry of the experiment and the changes in the neutron energy after every collision in the target and in the detectors. Figure 6.14 shows the efficiency $\varepsilon(E)$ at the two scattering angles 165° and 15° as a function of the incident energy on deuterium.

Finally, the ratio between 165° and 15° was computed in function of the incident energy E by

$$\frac{\frac{d\sigma}{d\Omega}(E)\big|_{165°}}{\frac{d\sigma}{d\Omega}(E)\big|_{15°}} = \frac{n_{single}(E)\big|_{165°} \cdot \varepsilon(E)|_{15°}}{n_{single}(E)\big|_{15°} \cdot \varepsilon(E)|_{165°}} \tag{6.3}$$

where n_{single} is the number of detected events due to single scattering on deuterium.
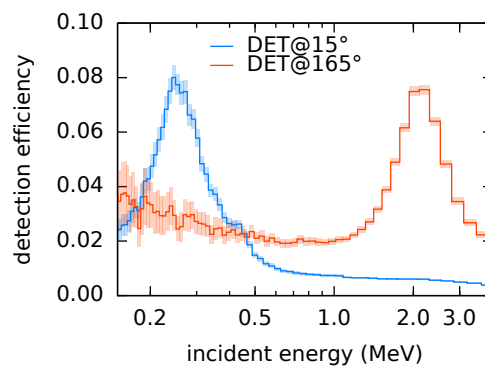
Figure 6.14: Calculated detection efficiency for detectors at 15° and at 165° as a function of the neutron energy incident on deuterium.
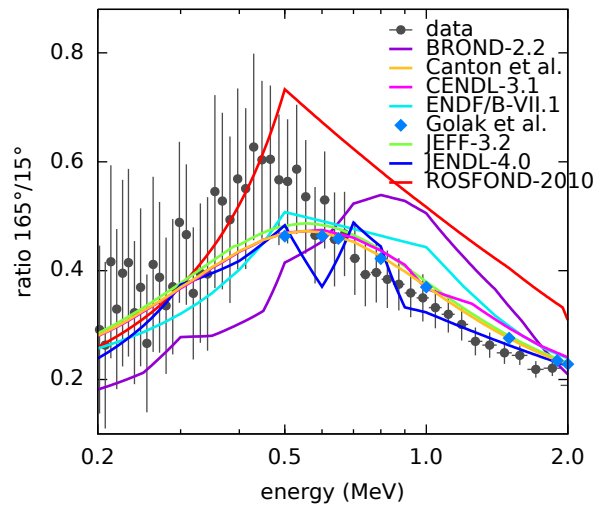
Figure 6.15: Comparison of the ratio $\left.\frac{d\sigma}{d\Omega}\right|_{165°}\!\!\bigg/\left.\frac{d\sigma}{d\Omega}\right|_{15°}$: experimental results versus the main evaluated libraries and the calculations of Canton *et al.*

6.4 Results

Figure 6.15 shows the experimental results of $\left.\frac{d\sigma}{d\Omega}\right|_{165°}\!\!\bigg/\left.\frac{d\sigma}{d\Omega}\right|_{15°}$, compared with the evaluated libraries, the theoretical calculations of Canton *et al.* [28] and of Golak *et al.* [38, 150]. Because of the low counting statistics, especially at 165°, and thus of the large uncertainties, it was not possible to extend the results below 200 keV. Above 2 MeV, the data cannot be fully trusted because the detectors response was not fully modelled (see Figs. 6.7, 6.9 and 6.12 for t.o.f. < 300 ns). For example, the ^{6}Li(n,n'd)^{4}He reaction, which has a negative Q-value of -1.47 MeV, was not included in the simulations for the determination of the efficiency. This does not affect the data of the detectors at backward angles, because neutrons with initial energy of 2 MeV have a kinetic energy of 230 keV after the scattering at 165°; but it could have some impact for the data of detectors at 15°.

In general, the data suggest that in the energy range from 350 to 600 keV the n-d scattering angular distribution is either more isotropic or more backward peaked than how it is reported in the evaluated nuclear libraries. Overall, the data are compatible with the theoretical calculations of Canton *et al.* and the recent EFT based one of Golak *et al.*, and the evaluated libraries CENDL-3.1 and JEFF-3.2. Also JENDL-4.0 is compatible, but the dip at 600 keV does not seem to be very physical. ENDF/B-VII.1 is in agreement with the data up to 700 keV, slightly below the measurements for energies below 500 keV. From 700 keV to 1.7 MeV the ratio 165° over 15° is higher than what found experimentally. ROSFOND-2010 is consistent only with the data below 490 keV and BROND-2.2 exhibits the largest deviations, but those two libraries are also the oldest evaluations among those presented.

To understand to what degree the comparison between the experimental results and the different options for the angular distribution of n-d scattering could be affected by the method of data analysis, we provide in Fig. 6.16 a direct comparison of the raw experimental data with a full simulation of the setup. This has the advantage that no approximations are made to account for the detector response. The data are shown with the background from the sample-out run subtracted. The calculation uses the full specification of the neutron beam, the sample, the detectors and the frame that holds them. The data used for each nucleus were kept the same (ENDF/B-VII) except for the data for deuterium. The region of normalization is for time of flights between 450 and 750 ns. To better visualize the differences the ratio between the calculations and the experimental data are plotted in Fig. 6.17.
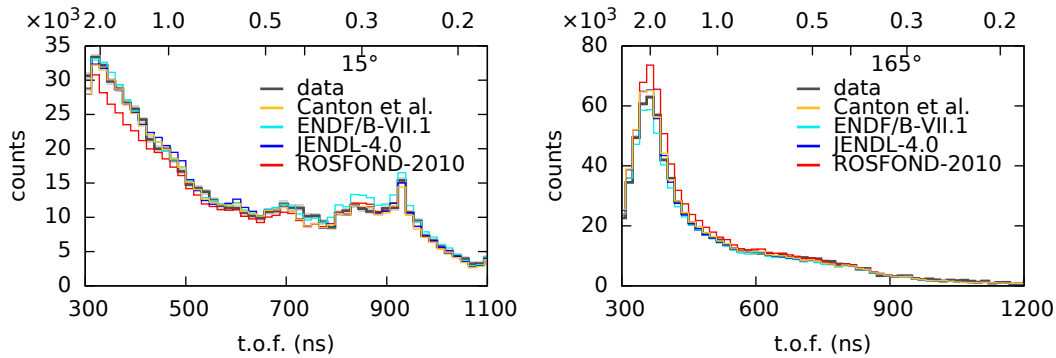
Figure 6.16: Comparison the experimental t.o.f. spectra with the MCNP5 simulations obtained after using several different libraries for the deuterium cross section tables. These spectra are the sum of the counts coming from all detectors at same angle.

In the energy range from 200 keV to 2 MeV the calculations for n-d scattering that are in best agreement with the experimental data are by Canton *et al.* and those included in JENDL-4.0. At 15° the cross section data calculated by Canton *et al.* show smaller deviations from the experiment. For both libraries, the difference with the data remains within 10% in the entire range at 15° and above 300 keV at 165°. Below 300 keV, however, the low statistic at 165° results in large fluctuations. At 15° for t.o.f. from 720 to 780 ns, i.e. from about 355 keV to 420 keV of neutron energy, there is a clear dip where all four simulations display a similar trend. A similar feature, but less pronounced, is also found at 165° in the same t.o.f. interval. This suggests that this discrepancy is not due to the deuterium cross section since for scattering on deuterium the same time of flight interval corresponds to very different detected energies. If this were an artifact of the simulation, then in Fig. 6.15 the experimental data for the differential cross sections ratio of 165° to 15° would be reduced by about 5% for incident neutrons with energies between 355 keV and 420 keV. For the simulations using the ENDF/B-VII.1 evaluated library the ratio "MCNP/data" remains within 15% from the data everywhere at 165°, while at 15° it is so only for energies above 355 keV (t.o.f. < 780 ns). If only the values that were not used for the normalization are considered, then it means that ENDF/B-VII.1 tends to overestimate the scattering at 15° for energies below 355 keV. ROSFOND-2010 is compatible with the data only at low energies: below 530 keV (t.o.f. > 700 ns) at 165° and below 350 keV (t.o.f. > 790 ns) at 15°. In the rest of the range, the simulation overestimates the number of events at the backward angles and underestimates them at forward angles, which implies that the angular distribution should be less backward peaked. For the calculations by Golak *et al.* no MCNP compatible file (ACE file) was available allowing a similar comparison. The strong similarity with Canton *et al.* in Fig. 6.15 suggests it would perform similarly in Figs. 6.16 and 6.17 as well.

6.5 Conclusions

A new experiment for the investigation of the n-d scattering angular distribution was performed at the neutron t.o.f. facility nELBE. The measurement, carried out using a highly enriched CD_2 sample, was complemented with two additional runs, one with graphite and the other with no sample. The three runs were realized so to be able to discriminate between n-d scattering and n-carbon scattering or background events. Extensive MCNP simulations with a realistic experimental geometry and neutron flux were used to subtract the multiple scattering contribution and to determine the efficiency of the detectors.

The ratio of the differential cross section at 15° and 165° was determined, and the results cover the neutron energy range from 200 keV to 2 MeV. The experimental data are in agreement with the theoretical calculations performed by Canton *et al.* and Golak *et al.*, who obtained highly compatible predictions for the n-d scattering differential cross section
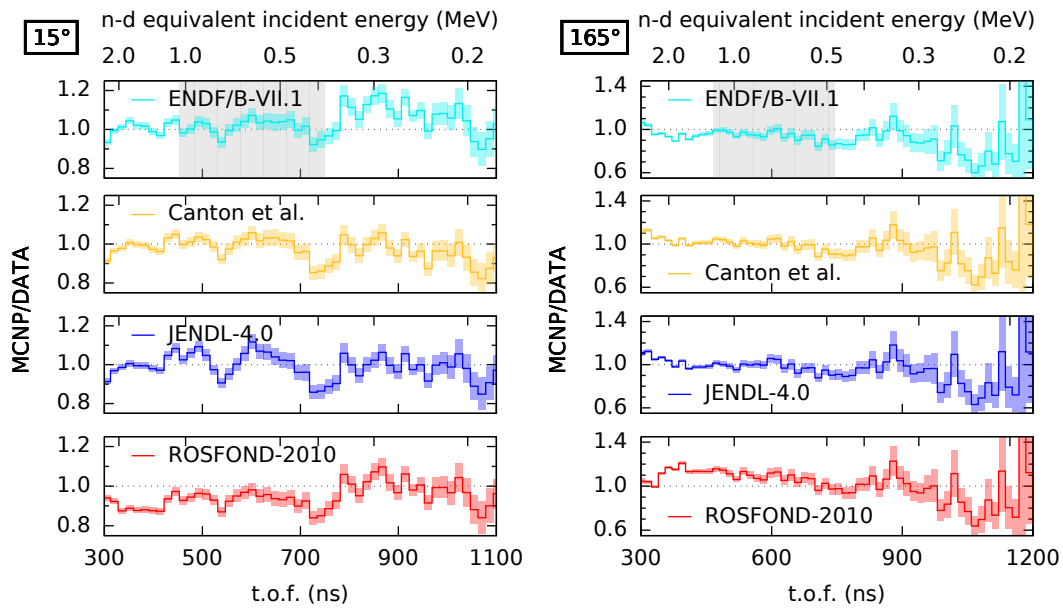
Figure 6.17: Ratio between the MCNP and the experimental t.o.f. histograms shown in Fig. 6.16. The grey area represent the t.o.f. interval considered when computing the rescaling factor for the comparison between data and simulation.

using two different formulations of the nuclear potential. The comparison with the evaluated nuclear data libraries indicates CENDL-3.1, JEFF-3.2 and JENDL-4.0 as the evaluations that best describe the asymmetry of the n-d scattering. In the energy range from 350 and 600 keV, however, the experimental backward to forward ratio is higher than that reported in the libraries. This suggests that the angular distributions should be either more isotropic or more backward peaked. ENDF/B-VII.1 predicts a higher backward to forward ratio than that actually measured for energies above 700 keV, while below 500 keV it is slightly lower. ROSFOND-2010 and BROND-2.2 are based on old evaluations and also have the worst compatibility with the experimental data.

Summary 7

Except in the case of a few light nuclei, nuclear properties and reaction data cannot be predicted a priori, but must be determined experimentally. These properties include observables such as lifetimes, masses, or energy level structures. The focus of this doctoral thesis is on neutron induced reactions and in particular on the measurement of neutron scattering differential cross sections.

Neutron scattering constitutes a powerful tool for studying the properties of the nucleus, and has numerous applications in both science and technology. Cross section data are used for confirmation of ab initio calculations; differential cross sections, especially of elastic scattering, are used for tuning phenomenological models describing the nuclear potential and assessing the quality of microscopic approaches. Technologies relying on neutron scattering data include important applications such as the design of medical accelerators for radiation therapy, and energy production (fission and fusion reactors). For applications, the importance of neutron scattering is in transport in large media due to the magnitude of the cross section and the typically small absorption cross section. A very important aspect is its role in the moderation process of fast neutrons. Accurate differential data are required for the modelling of nuclear systems, for the determination of neutron flux spatial and energy distributions, and for reaction rate calculations.

The main objective of this work has been the development of a new experimental setup for the study of neutron scattering angular distributions in the fast neutron energy range employing liquid organic scintillators. It included the design of a new digitizer-based data-acquisition system and the required software for data taking and sorting. The method further involved the development of simulations for multiple scattering corrections, response function determination and their proper combination using the MCNP5 code with the PTRAC option storing full histories. A code was developed to interpret the PTRAC output, which was validated against MCNP5 standard tallies and the response function code NRESP for cases where these work reliably. The full method was validated with a measurement of the cross section of neutron elastic scattering on carbon. It was then used to deliver new iron scattering data in the interest of nuclear applications. In the experiments on iron, the possibility of extending the method to determine also inelastic scattering cross sections and angular distributions was investigated. The validity of the method and the iron results were also confirmed with a second experiment for n-Fe scattering at the neutron time-of-flight facility nELBE of the Helmholtz-Zentrum Dresden-Rossendorf where a classical state-of-the-art data-acquisition system was used. Measurements on the backward-forward asymmetry of scattering on deuterium were also performed, covering a neutron energy range extending to energies below 1 MeV. A different experimental setup with lithium glass scintillators was utilized in this case and use was made of the low-scattering facility of nELBE to limit room return.

The organic scintillator spectrometer was designed and assembled at GELINA, the white neutron source operated by the Joint Research Centre in Geel. The scintillators characterization measurements, the experiments on carbon and iron were carried out there. The setup consists of an ^{235}U fission chamber as flux monitor, and 32 liquid organic scintillators for the detection of scattered neutrons. The scintillators are arranged in four groups of 8 detectors each; 16 detectors are EJ301 detectors (hydrogen based) while the other

16 are EJ315 (deuterium based). Organic scintillators are fast detectors, well suited for time-of-flight measurements thanks to the short signal rise time and duration, and their n/γ separation capabilities. Having four sets of detectors allows to check the repeatability of the measurements, while having these two types of scintillators gives the chance to recognize systematic effects due to the response function. For each group, the detectors are placed at 8 specific angles to the neutron beam, which were chosen to be able to apply the 8-points Gauss-Legendre quadrature. This numerical integration rule grants exact integration results for polynomials of order 15 or less. This matches the expected highest degree of polynomial for cases such as carbon and iron, and also for higher masses provided the incident energy is less than 10 MeV.

In this work it has been shown that the setup allows the simultaneous determination of the differential cross section and the angle-integrated scattering cross section with high energy resolution using the neutron time-of-flight technique. The discrimination of elastic from inelastic scattering, based on the observation that different reactions (elastic, inelastic from the first level, etc) produce neutrons with different energies, is achieved by taking advantage of the spectrometry capabilities of the organic scintillators. Although the energy of the scattered neutron cannot be determined event-by-event, the spectrometry information is achieved analysing the pulse-height distributions. This analysis requires the thorough characterization of the detector response to both neutrons and photons, which was obtained combining calibration measurements and Monte Carlo simulations. The simulations were implemented in MCNP5, which was used to model the photon and neutron transport, while a separate post-processing code was prepared to correlate the neutron energy deposition with the scintillation light output. In order to calibrate the neutron response, it was assumed that the pulse-height spectra corresponding to different t.o.f. intervals in the carbon measurement were produced by monoenergetic neutrons whose energies were defined by kinematics. These calibration measurements are in good agreement with the model calculations for the hydrogen-based detectors, while for the deuterium-based ones the agreement varied with the neutron energy. The discrepancies are possibly due to the contributions of multiple scattering events in the carbon target, and also to the evaluated n-d scattering angular distributions used in the simulations.

The angle-integrated cross section of elastic scattering on carbon turned out to be compatible with the results of previous experiments and the evaluation from the ENDF/B-VII.1 nuclear data library in the energy range from 2 MeV to 7 MeV, with uncertainties ranging from 5% to 10%. Above 7 MeV, the flux at GELINA is too low and precise measurements are difficult. Below 2 MeV, the discrepancies are most likely due to the high detection threshold of the detectors, which complicated applying the detector response model. The differential cross sections have uncertainties that range from 9% to 15%. In the energy interval from 2 MeV to 7 MeV they were found to be consistent with the other available measurements but not with the evaluated differential cross sections for angles close to 90°. Above 2 MeV the differential cross section of elastic scattering on carbon is not considered a standard, and this discrepancy suggests that some improvements might be necessary in the range from 3 MeV to 5 MeV.

For the measurement on iron, both elastic and inelastic scattering from the first excited state were considered. For the elastic scattering cross section the experimental uncertainties ranged from 10% to 18%, while for the differential cross section they were between 20% and 50%. The results obtained at both facilities agree with each other confirming the validity of the new digitizer-based data-acquisition. The energy resolution of both experiments is not enough to resolve the fine structure of the cross section. However, the main features of the reaction are well represented, like the strong forward asymmetry, and the increasing contribution of the backward scattering for decreasing energies. The new results compare well with both previous experiments for energies where results are available and the latest evaluations. The new results add substantially to the database for angular distributions for energies from 3 to 6 MeV and for the angle integrated elastic scattering cross section. The inelastic scattering angular distribution determination was affected by larger uncertainties, in particular at forward angles, where the combination of the statistical uncertainties and the predominance of elastic scattering gave unreliable results. Partial

angular distributions could still be determined, and the assumption of a nearly-isotropic differential cross sections (supported by the statistical model) was used to correct the angle integration.

In the complementary experiment on n-d scattering, the targeted energy range extended to energies below 1 MeV. For this reason lithium glass scintillators were use instead of organic scintillators. However, because of the lower detection efficiency, the measurements were limited to two angles only, to increase statistics. To avoid flux normalization complications, only the angular distribution and not the differential cross section was considered. The backward to forward asymmetry was determined and compared with the result of the main nuclear data libraries evaluations, and with theoretical models based on the application of the effective field theory. This investigation revealed that below 2 MeV, the evaluations that best describe the reaction asymmetry are those included in the CENDL-3.1, JEFF-3.2 and JENDL-4.0 libraries. A good description is also obtained with the model calculations by Canton et al. based on meson exchange and a proposal for the three-body interaction by Golak et al. based on effective field theory.

In the current experimental databases, most of the neutron angular distribution measurements were performed with the intent of providing point-wise results needed by fundamental research, rather than with the idea of producing complete datasets. There are few exceptions like carbon: for the establishment of the standard, numerous high-resolution experiments were carried out. Also in this case, most of the datasets are limited, in the sense that they only reach the upper limit of the energy interval where the cross section is considered a standard. The scarcity of measurements in the fast neutron energy region poses a problem for the nuclear data evaluations used in applications. In particular, to lower the uncertainties below the limits requested by the engineering of advanced nuclear systems, high-resolution double-differential cross-section measurements are necessary. Regarding the method presented in this thesis, some improvements are still necessary in the case of inelastic scattering, but the first measurements provided good results for elastic scattering differential and angle-integrated cross sections.

For future work with this setup several improvements should be considered. It was observed in all measurements that the thickness and the diameter of the target play an important role and can influence the accuracy of the data analysis. Therefore, they should be optimized to minimize the effects of multiple scattering. Ideally the diameter should be just large enough to intercept the beam and the thickness should be such that the multiple scattering contribution does not exceed the 10% of the total. The measurements for characterizing the neutron response of the organic scintillators were also affected by multiple scattering. The parameters obtained analysing the response to scattered neutrons should be verified with the analysis of the (d,Be) measurement carried out at the Physikalisch-Technische Bundesanstalt, where the detectors were directly irradiated with neutrons. These data for the deuteron based EJ315 detectors are again of interest for the determination of the angular distribution of n-d scattering as the deuteron recoil energy distributions directly reflect this quantity, in particular for backward scattering.

For cases like iron, the composition of the target affects the accuracy of the separation of the elastic and inelastic reactions. The measurement of the isotope of interest is affected by the presence of other species. Elastic scattering from different isotopes cannot be discriminated on the basis of the neutron energy because the resolution of the detectors does not allow it. Due to overlapping levels, inelastic scattering is affected too. Measurements with highly enriched samples are preferred as it is extremely difficult to separate the contribution of low-abundance isotopes during the data analysis.

The measurements on carbon and iron were both relatively short because of the delays in the development of the data acquisition system and the timeframe imposed by the PhD contract. As the assessment of the background requires both sample-in and sample-out measurements, the actual irradiation time of the carbon and iron targets was limited to a few days only. The easiest way to obtain higher precision is therefore to carry out longer measurements, which can now be justified on account of the good results obtained in this campaign and will be a necessary requirement for thinner targets minimizing multiple scat-

tering. This will help also improving the results of the inelastic scattering differential cross section, as higher statistics would help to achieve better separation.

Samenvatting

Behalve in enkele gevallen kunnen kerneigenschappen en reactie-gegevens niet a priori worden voorspeld maar moeten ze experimenteel worden bepaald. Deze eigenschappen betreffen grootheden zoals de levensduur, massa's of energieniveaus. De focus van dit proefschrift betreft neutron-geïnduceerde reacties en in het bijzonder de meting van differentiële doorsneden van neutronenverstrooiing.

Neutronenverstrooiing is een krachtige methode voor het bestuderen van kerneigenschappen en heeft vele toepassingen in wetenschap en technologie. Gegevens voor werkzame doorsneden worden gebruikt voor ab initio berekeningen; differentiële werkzame doorsneden, in het bijzonder voor elastische verstrooiing, worden gebruikt voor het aanpassen van fenomenologische modellen voor de kernpotentiaal en om de kwaliteit van microscopische benaderingen te beoordelen. Het gebruik van verstrooiingsgegevens voor neutronen in de technologie betreft belangrijke toepassingen zoals het ontwerp van medische versnellers voor stralingstherapie en opwekking van energie middels splijting of fusie. Voor toepassing ligt het belang van neutronenverstrooiing in het transport in grote media als gevolg van de grootte van de werkzame doorsnede en de kleine doorsnede voor absorptie. Van groot belang is de rol bij het modereren van snelle neutronen. Accurate werkzame doorsneden zijn nodig voor berekeningen van de plaats- en energie-afhankelijkheid van de neutronenflux en van reactiesnelheden.

Het hoofddoel van dit werk was de ontwikkeling van een nieuwe experimentele opstelling voor de bestudering van hoekverdelingen van verstrooide snelle neutronen, gebruik-makend van vloeistofscintillatoren. Dit omvatte het ontwerp van een nieuwe op digitizers gebaseerde data-acquisitie opstelling en de ontwikkeling van de benodigde software voor het registreren van de gegevens en het analyseren daarvan. De methode betreft ook de ontwikkeling van simulaties ten behoeve van correcties voor meervoudige verstrooiing, het bepalen van responsfuncties en een correcte combinatie van deze twee aspecten. Dit werd gerealiseerd met gebruik van de MCNP5 code met de PTRAC optie voor het registreren van complete interactiegeschiedenissen. Een code werd ontwikkeld voor de interpretatie van de PTRAC uitvoer en gevalideerd tegen standaard MCNP5 scores en responsfuncties berekend met de NRESP code voor gevallen waar deze alternatieven betrouwbare resultaten geven. De geldigheid van de methode en de resultaten voor ijzer werden bevestigd met een tweede experiment voor n-Fe verstrooiing aan de neutronenvluchttijdopstelling van nELBE op het Helmholtz-Zentrum Dresden-Rossendorf, waar een klassieke state-of-the-art data-acquisitie opstelling werd gebruikt. Een belangrijk tweede doel van dit werk betrof metingen van de voorwaarts-achterwaarts asymmetrie van neutron-deuteron verstrooiing voor energieën beneden 1 MeV. Hiervoor moest een andere opstelling gebaseerd op lithium-glas detectoren worden gebruikt en werd wederom gemeten aan de nELBE faciliteit vanwege de lage bijdrage van neutronen die terugkeren naar de detectoren na verstrooiing in de meetruimte aldaar.

De spectrometer van organische vloeistofscintillatoren is ontworpen en gebouwd aan GELINA, de witte neutronenbron die operationeel is bij het Gemeenschappelijk Centrum voor Onderzoek in Geel. De metingen voor het karakteriseren van de scintillatoren en de experimenten op koolstof en ijzer werden hier uitgevoerd. De opstelling maakt gebruik van een splijtkamer met ^{235}U voor het registreren van de flux en van 32 vloeistofscintillatoren

voor het detecteren van de verstrooide neutronen. De scintillatoren zijn verdeeld in vier groepen van acht; 16 zijn van het type EJ301 (gebaseerd op protonen) en 16 zijn van het type EJ315 (gebaseerd op deuterium). Organische vloeistofscintillatoren zijn snelle detectoren die uitermate geschikt zijn voor vluchttijdmetingen vanwege een korte rijstijd en duur van het signaal en de mogelijkheid neutronen te scheiden van fotonen. Met vier groepen van detectoren is er redundantie waardoor consistentie kan worden geverifieerd en met twee types scintillator kunnen systematische effecten als gevolg van de responsfunctie worden geïdentificeerd. Voor elke groep staan de detectoren onder 8 specifieke hoeken met de neutronenbundel met als doel het toepassen van de 8-punts Gauss-Legendre integratie-regel. Deze regel voor numerieke integratie is exact voor polynomen van orde 15 of minder. Dit komt overeen met de verwachtte hoogste orde van een polynoom (in de cosinus van de verstrooingshoek) dat de hoekverdeling beschrijft in geval van bijvoorbeeld koolstof en ijzer, maar ook voor zwaardere kernen zolang het inkomende neutron een energie minder dan 10 MeV heeft.

In dit werk is aangetoond dat de opstelling tegelijkertijd differentiële en hoek-geïntegreerde werkzame doorsneden kan bepalen met een hoge energieresolutie door middel van bepaling van de vluchttijd van neutronen. Het onderscheiden van elastische en inelastische verstrooiing, gebaseerd op het verschil in energie na verstrooiing door de reactie (elastisch, inelastisch naar het eerst niveau, etc.), wordt bereikt door gebruik te maken van het spectrometrisch vermogen van de organische scintillatoren. Hoewel de energie van het gedetecteerde neutron niet voor iedere gebeurtenis kan worden bepaald, kan analyse van het pulshoogte-spectrum wel de benodigde informatie geven. Deze analyse vereist een grondige karakterisering van de responsfunctie van de detector voor zowel neutronen als fotonen, welke werd bereikt door het combineren van kalibratiemetingen met Monte Carlo simulaties. De simulaties werden uitgevoerd met MCNP5 voor het neutron en foton-transport, terwijl een aparte code werd gebruikt voor het verwerken van de uitvoer en het correleren van de energieafgifte door neutronen met het licht afgegeven door de scintillator. Om de neutronenrespons te kalibreren werd aangenomen dat het pulshoogte-spectrum van bepaalde vluchttijd-intervallen bij de meting voor koolstof werd veroorzaakt door mono-energetische neutronen waarvan de energie vastligt door de kinematica. Deze kalibratiemetingen komen goed overeen met de modelberekeningen in het geval van de proton-gebaseerde detectoren, terwijl voor de deuteron-gebaseerde detectoren de overeenkomst afhangt van de energie. De afwijkingen zijn mogelijk het gevolg van de bijdragen van meervoudige verstrooiing in de koolstof trefplaat en ook van de n-d hoekver-delingen zoals gebruikt in de simulaties.

De hoek-geïntegreerde werkzame doorsneden voor elastische verstrooiing aan koolstof bleken compatibel te zijn met resultaten behaald in eerdere experimenten en de evalu-atie van de ENDF/B-VII.1 gegevensbank voor het energiegebied van 2 tot 7 MeV binnen de onzekerheden die tussen 5% en 10% liggen. Boven 7 MeV is de flux aan GELINA te laag en zijn precieze metingen moeilijk. Beneden 2 MeV zijn de afwijkingen hoogst waarschijn-lijk het gevolg van de hoge detectiedrempel waardoor toepassing van het responsmodel gecompliceerd is. De differentiële werkzame doorsneden hebben onzekerheden tussen 9% en 15%. In het energiegebied van 2 tot 7 MeV zijn deze consistent bevonden met andere beschikbare metingen maar niet met bibliotheken van geëvalueerde werkzame doorsneden voor hoeken rond 90 graden. Boven 2 MeV is de differentiële werkzame doorsnede voor elastische verstrooiing geen standaard en deze afwijking wijst erop dat enige verbetering tussen 3 en 5 MeV nog nodig is.

Voor de meting van ijzer werden zowel elastische als inelastische verstrooiing naar het eerste aangeslagen niveau bekeken. Voor elastische verstrooiing lagen de experimentele onzekerheden tussen 10% en 18% terwijl deze voor de differentiële werkzame doorsnede tussen 20% en 50% lagen. De resultaten behaald aan beide faciliteiten kwamen met elkaar overeen, hetgeen het nieuwe systeem voor data-acquisitie op basis van digitizers valideert. In beide experimenten is de energie-resolutie onvoldoende om de fijnstructuur in de werkzame doorsnede op te lossen. Daar staat tegenover dat de belangrijkste ei-genschappen van de reactie goed naar voren komen, in het bijzonder de sterke voorwaartse asymmetrie en de toename in achterwaartse verstrooiing met afnemende energie. De

nieuwe resultaten komen goed overeen met eerdere experimenten voor zover beschikbaar en met de meest recente evaluaties. Ze leveren een belangrijke nieuwe bijdrage tot de data voor hoekverdelingen in het energiegebied tussen 3 en 6 MeV en voor de werkzame doorsneden voor elastische verstrooiing. De bepaling van de hoekverdeling voor inelastische verstrooiing was omgeven met grotere onzekerheden, in het bijzonder voor voorwaartse hoeken waar statistische onzekerheden en de dominantie van elastische verstrooiing tot onbetrouwbare resultaten leiden. Een gedeeltelijke hoekverdeling kan nog wel worden bepaald en met de aanname van een nagenoeg isotrope verdeling (ondersteund door het statistisch model) werd de hoekintegraal gecorrigeerd.

In het complementaire experiment voor n-d verstrooiing werd gestreefd naar energieën beneden 1 MeV. Om deze reden werden acht lithium-glas detectoren gebruikt in plaats van organische vloeistofscintillatoren. Echter, vanwege de lage detectie-efficiëntie werd de meting beperkt tot 2 hoeken om de statistiek te verhogen. Om complicaties van fluxnormering te voorkomen werd een hoekverhouding bepaald en niet de differentiële werkzame doorsnede. De gemeten achterwaarts-voorwaarts asymmetrie werd vergeleken met de belangrijkste evaluaties en met theoretische modellen gebaseerd op effectieve veldentheorie. Dit onderzoek liet zien dat beneden 2 MeV de beste overeenstemming wordt gevonden voor de evaluaties uit de CENDL-3.1, JEFF-3.2 en JENDL-4.0 bibliotheken. Een goede overeenkomst wordt ook gevonden met de modelberekeningen van Canton et al. gebaseerd op meson-uitwisseling en een voorstel voor de 3-nucleon wisselwerking en van Golak et al. gebaseerd op effectieve velden- theorie.

In de huidige experimentele databanken zijn de meeste metingen van neutronen-hoekverdelingen verricht met het doel om enkele resultaten te verschaffen voor fundamenteel onderzoek en niet met het doel om complete datasets te produceren. Er zijn maar weinig uitzonderingen zoals koolstof: voor het vaststellen van een standaard werden vele metingen met een hoge resolutie uitgevoerd. Ook in dit geval zijn de beschikbare data beperkt en wel tot de energielimiet waar die standaard van toepassing is. Het tekort aan metingen voor snelle neutronen leidt tot problemen bij de evaluatie van kernreactie-gegevens voor toepassingen. In het bijzonder zijn, om te komen tot onzekerheden beneden de limieten afgeleid uit ontwikkelingseisen voor geavanceerde kernenergiesystemen, hoge resolutie dubbeldifferentiële werkzame doorsneden nodig. Voor wat betreft de methode gepresenteerd in dit proefschrift zijn zekere verbeteringen aangewezen voor het geval van inelastische verstrooiing, maar de eerste resultaten zijn goed voor elastisch verstrooiing, zowel voor differentiële als voor hoek-geïntegreerde werkzame doorsneden.

Voor verder werk met deze opstellingen moeten een aantal verbeteringen worden overwogen. Zoals werd vastgesteld in alle metingen zijn de dikte en diameter van de trefplaat belangrijk en hebben een duidelijke invloed op de nauwkeurigheid van de analyse. Ze moeten daarom geoptimaliseerd worden met het oog op minimalisatie van de effecten van meervoudige verstrooiing. Ideaal gezien zou de diameter net voldoende moeten zijn om de bundel te onderscheppen en de dikte moet zo worden gekozen dat meervoudige verstrooiing niet meer bijdraagt dan 10%. Ook de metingen voor de karakterisering van de respons van de organische scintillatoren ondervonden het effect van meervoudige verstrooiing. De parameters afkomstig uit de analyse van de respons voor verstrooide neutronen moeten worden geverifieerd met de responsfuncties bepaald met de (d,Be) meting uitgevoerd aan de Physikalisch Technische Bundesanstalt waar de detectoren direct waren blootgesteld aan neutronen. Deze gegevens voor de deuteron-gebaseerde EJ315 detectoren zijn ook van belang voor de bepaling van hoekverdelingen voor n-d verstrooiing omdat de deuteron energieverdelingen rechtstreeks betrekking hebben op deze grootheid, in het bijzonder voor achterwaartse verstrooiing.

In het geval van ijzer bepaalt de samenstelling van het materiaal de nauwkeurigheid van de scheiding van elastische en inelastische verstrooiing. De meting van het belangrijkste isotoop wordt beperkt door de aanwezigheid van andere isotopen. Elastische verstrooiing aan verschillende isotopen is niet te scheiden omdat de energieverschillen te klein zijn. Als gevolg van overlappende niveaus zijn er ook beperkingen voor inelastische verstrooiing. Metingen met hoogaangerijkte trefplaten verdienen de voorkeur omdat het erg moeilijk is

om de bijdrage van isotopen met een lage aanrijking te onderscheiden.

De metingen aan koolstof en ijzer waren beide relatief kort als gevolg van de vertragin-gen in de ontwikkeling van het data-acquisitie systeem en de duur van het doctoraatscon-tract. Aangezien de bepaling van de ondergrond vraagt om zowel trefplaat-in en trefplaat-uit metingen was de tijd voor bestraling van koolstof en ijzer beperkt tot enkele dagen. De gemakkelijkste manier om tot een betere nauwkeurigheid te komen is dus langer meten, iets wat gerechtvaardigd is op basis van de goede resultaten behaald in deze campagne. Dit is ook noodzakelijk als dunnere trefplaten worden gebruikt zoals vereist voor een min-imalisatie van de bijdrage van meervoudige verstrooiing. Deze verbeteringen zullen ook bijdragen aan een verbetering van de resultaten voor de differentiële werkzame doorsnede voor inelastische verstrooiing, omdat betere statistiek leidt tot een beter onderscheidend vermogen.

Bibliography

[1] R. Machleidt, "The nuclear force: Meson theory versus chiral effective field theory," *International Journal of Modern Physics E*, vol. 26, p. 1740018, 2017.

[2] R. Henning, "Current status of neutrinoless double-beta decay searches," *Reviews in Physics*, vol. 1, pp. 29–35, 2016.

[3] S. Woosley, A. Heger, and T. Weaver, "The evolution and explosion of massive stars," *Rev. Mod. Phys.*, vol. 74, pp. 1015–1071, 2002.

[4] R. Cyburt, B. Fields, K. Olive., and T.-H. Yeh, "Big bang nucleosynthesis: Present status," *Reviews of Modern Physics*, vol. 88, p. 015004, 2016.

[5] F. Käppeler, R. Gallino, S. Bisterzo, and W. Aoki, "The s process: Nuclear physics, stellar models, and observations," *Reviews of Modern Physics*, vol. 83, pp. 157–193, 2011.

[6] A. Robinson, "New libraries for simulating neutron scattering in dark matter detector calibrations," *Physical Review C*, vol. 89, p. 032801, 2014.

[7] G. Locatelli, M. Mancini, and N. Todeschini, "Generation IV nuclear reactors: Current status and future prospects," *Energy Policy*, vol. 61, pp. 1503–1520, 2013.

[8] "Status of accelerator driven systems research and technology development," IAEA TECDOC series IAEA-TECDOC-1766, International Atomic Energy Agency, 2015.

[9] J. Ongena and Y. Ogawa, "Nuclear fusion: Status report and future prospects," *Energy Policy*, vol. 96, pp. 770–778, 2016.

[10] M. Salvatores and R. Jacqmin, "Uncertainty and target accuracy assessment for innovative systems using recent covariance data evaluations," NEA/WPEC subgroup 26 final report, OECD Nuclear Energy Agency, 2008.

[11] H. Harada and A. Plompen, "Meeting nuclear data needs for advanced reactor systems," NEA/WPEC subgroup 31 final report, OECD Nuclear Energy Agency, 2014.

[12] OECD Nuclear Energy Agency, "JEFF-3.2 Evaluated Data Library." available at `https://www.oecd-nea.org/dbforms/data/eva/evatapes/jeff_32/`.

[13] M. B. Chadwick, M. Herman, P. Obložinský, M. E. Dunn, Y. Danon, A. C. Kahler, D. L. Smith, B. Pritychenko, G. Arbanas, R. Arcilla, R. Brewer, D. A. Brown, R. Capote, A. D. Carlson, Y. S. Cho, H. Derrien, K. Guber, G. M. Hale, S. Hoblit, S. Holloway, T. D. Johnson, T. Kawano, B. C. Kiedrowski, H. Kim, S. Kunieda, N. M. Larson, L. Leal, J. P. Lestone, R. C. Little, E. A. McCutchan, R. E. MacFarlane, M. MacInnes, C. M. Mattoon, R. D. McKnight, S. F. Mughabghab, G. P. A. Nobre, G. Palmiotti, A. Palumbo, M. T. Pigni, V. G. Pronyaev, R. O. Sayer, A. A. Sonzogni, N. C. Summers, P. Talou, I. J. Thompson, A. Trkov, R. L. Vogt, S. C. van der Marck, A. Wallner, M. C. White, D. Wiarda, and P. G. Young, "ENDF/B-VII.1 nuclear data for science and technology: cross sections, covariances, fission product yields and decay data," *Nuclear Data Sheets*, vol. 112, pp. 2887–2996, 2011. Special Issue on ENDF/B-VII.1 Library.

[14] K. Shibata, O. Iwamoto, T. Nakagawa, N. Iwamoto, A. Ichihara, S. Kunieda, S. Chiba, K. Furutaka, N. Otuka, T. Ohsawa, T. Murata, H. Matsunobu, A. Zukeran, S. Kamada, and J. I. Katakura, "JENDL-4.0: A new library for nuclear science and engineering," *Journal of Nuclear Science and Technology*, vol. 48, pp. 1–30, 2011.

[15] Z. G. Ge, Z. X. Zhao, H. H. Xia, Y. X. Zhuang, T. J. Liu, J. S. Zhang, and H. C. Wu, "The updated version of Chinese Evaluated Nuclear Data Library (CENDL-3.1)," *Journal of the Korean Physical Society*, vol. 59, pp. 1052–1056, 2011.

[16] Institute of Physics and Power Engineering, "BROND-3.1 library." available at `https://www.vant.ippe.ru/en/brond-3-1.html`.

[17] Institute of Physics and Power Engineering, "ROSFOND-2010 library." available at `http://www.ippe.ru/podr/abbn/libr/rosfond.php`.

[18] M. Chadwick, E. Dupont, E. Bauge, A. Blokhin, O. Bouland, D. Brown, R. Capote, A. Carlson, Y. Danon, C. D. S. Jean, M. Dunn, U. Fischer, R. Forrest, S. Frankle, T. Fukahori, Z. Ge, S. Grimes, G. Hale, M. Herman, A. Ignatyuk, M. Ishikawa, N. Iwamoto, O. Iwamoto, M. Jandel, R. Jacqmin, T. Kawano, S. Kunieda, A. Kahler, B. Kiedrowski, I. Kodeli, A. Koning, L. Leal, Y. Lee, J. Lestone, C. Lubitz, M. MacInnes, D. McNabb, R. McKnight, M. Moxon, S. Mughabghab, G. Noguere, G. Palmiotti, A. Plompen, B. Pritychenko, V. Pronyaev, D. Rochman, P. Romain, D. Roubtsov, P. Schillebeeckx, M. Salvatores, S. Simakov, E. Soukhovitskiĭ, J. Sublet, P. Talou, I. Thompson, A. Trkov, R. Vogt, and S. van der Marck, "The CIELO collaboration: neutron reactions on ^{1}H, ^{16}O, ^{56}Fe, ^{235,238}U, and ^{239}Pu," *Nuclear Data Sheets*, vol. 118, pp. 1–25, 2014.

[19] K. Kozier, "Sensitivity of MCNP5 calculations for a spherical numerical benchmark problem to the angular scattering distributions for deuterium," in *PHYSOR 2006 Topical Meeting: Advances in Nuclear Analysis and Simulation*, (Vancouver, BC), pp. 2123–2132, American Nuclear Society, 10-14 September 2006.

[20] N. Otuka, E. Dupont, V. Semkova, B. Pritychenko, A. I. Blokhin, M. Aikawa, S. Babykina, M. Bossant, G. Chen, S. Dunaeva, R. A. Forrest, T. Fukahori, N. Furutachi, S. Ganesan, Z. Ge, O. O. Gritzay, M. Herman, S. Hlavač, K. Katō, B. Lalremruata, Y. O. Lee, A. Makinaga, K. Matsumoto, M. Mikhaylyukova, G. Pikulina, V. G. Pronyaev, A. Saxena, O. Schwerer, S. P. Simakov, N. Soppera, R. Suzuki, S. Takács, X. Tao, S. Taova, F. Tárkányi, V. V. Varlamov, J. Wang, S. C. Yang, V. Zerkin, and Y. Zhuang, "Towards a more complete and accurate Experimental Nuclear Reaction Data Library (EXFOR): international collaboration between Nuclear Reaction Data Centres (NRDC)," *Nuclear Data Sheets*, vol. 120, pp. 272–276, 2014.

[21] N. Schunck and L. M. Robledo, "Microscopic theory of nuclear fission: a review," *Reports on Progress in Physics*, vol. 79, p. 116301, 2016.

[22] R. Machleidt, F. Sammarruca, and Y. Song, "Nonlocal nature of the nuclear force and its impact on nuclear structure," *Physical Review C*, vol. 53, pp. R1483–R1487, 1996.

[23] W. Hauser and H. Feshbach, "The inelastic scattering of neutrons," *Physical Review*, vol. 87, pp. 366–373, 1952.

[24] P. Hodgson, "The neutron optical potential," *Reports on Progress in Physics*, vol. 47, pp. 613–654, 1984.

[25] R. Varner, W. Thompson, T. McAbee, E. Ludwig, and T. Clegg, "A global nucleon optical model potential," *Physics Reports*, vol. 201, pp. 57–119, 1991.

[26] A. Koning and J. Delaroche, "Local and global nucleon optical models from 1 keV to 200 MeV," *Nuclear Physics A*, vol. 713, pp. 231–310, 2003.

[27] J. P. Svenne, K. Amos, D. van der Knijff, L. Canton, and G. Pisent, "MCAS: A multichannel algebraic scattering theory of low energy nucleon-nucleus reactions," *AIP Conference Proceedings*, vol. 769, pp. 1096–1099, 2005.

[28] L. Canton, W. Schadow, and J. Haidenbauer, "Irreducible pionic effects in nucleon-deuteron scattering below 20 MeV," *European Physical Journal A*, vol. 14, pp. 225–238, 2002.

[29] S. Binder, A. Calci, E. Epelbaum, R. J. Furnstahl, J. Golak, K. Hebeler, H. Kamada, H. Krebs, J. Langhammer, S. Liebig, P. Maris, U. G. Meißner, D. Minossi, A. Nogga, H. Potter, R. Roth, R. Skibiński, K. Topolnicki, J. P. Vary, and H. Witała, "Few-nucleon systems with state-of-the-art chiral nucleon-nucleon forces," *Physical Review C*, vol. 93, p. 044002, 2016.

[30] J. Lachkar, "Evaluation and use of carbon as a standard," in *Neutron Standards and Applications*, (Gaithersburg, MD), pp. 93–100, 28–31 March 1977. NBS special publication 493.

[31] A. Carlson, "The neutron cross section standards, evaluations and applications," *Metrologia*, vol. 48, pp. S328–S345, 2011.

[32] G. James, "Neutron energy standards," in *Neutron Standards and Applications*, (Gaithersburg, MD), pp. 319–328, 28–31 March 1977. NBS special publication 493.

[33] A. Infantino, M. Marengo, S. Baschetti, G. Cicoria, V. L. Vaschetto, G. Lucconi, P. Massucci, S. Vichi, F. Zagni, and D. Mostacci, "Accurate monte carlo modeling of cyclotrons for optimization of shielding and activation calculations in the biomedical field," *Radiation Physics and Chemistry*, vol. 116, pp. 231–236, 2015. Proceedings of the 9th International Topical Meeting on Industrial Radiation and Radioisotope Measurement Applications.

[34] OECD Nuclear Energy Agency, "Nuclear Data High-Priority Request List." available at http://www.oecd-nea.org/dbdata/hprl/.

[35] M. Wenner, A. Haghighat, J. Adams, A. Carlson, S. Grimes, and T. Massey, "Novel investigation of iron cross sections via spherical shell transmission measurements and particle transport calculations for material embrittlement studies," *Nuclear Science and Engineering*, vol. 170, pp. 207–233, 2012.

[36] H. Witała, W. Glöckle, J. Golak, A. Nogga, H. Kamada, R. Skibiński, and J. Kuroś-Żołnierczuk, "Nd elastic scattering as a tool to probe properties of 3N forces," *Physical Review C*, vol. 63, p. 024007, 2001.

[37] L. Marcucci, A. Kievsky, L. Girlanda, S. Rosati, and M. Viviani, "N-d elastic scattering using the hyperspherical harmonics approach with realistic local and nonlocal interactions," *Physical Review C*, vol. 80, p. 034003, 2009.

[38] J. Golak, R. Skibiński, K. Topolnicki, H. Witała, E. Epelbaum, H. Krebs, H. Kamada, U. G. Meißner, V. Bernard, P. Maris, J. Vary, S. Binder, A. Calci, K. Hebeler, J. Langhammer, R. Roth, A. Nogga, S. Liebig, and D. Minossi, "Low-energy neutron-deuteron reactions with N3LO chiral forces," *European Physical Journal A*, vol. 50, p. 177, 2014.

[39] L. W. Townsend, "Neutron-deuterium cross section evaluation," Final Technical Report AECL Purchase Order 217739, Atomic Energy of Canada Limited, 2006.

[40] R. Mosteller, J. Campbell, and R. Little, "Reactivity impact of ENDF/B-VI cross sections for deuterium in heavy-water solution benchmarks," in *2005 Annual Meeting of the American Nuclear Society*, (San Diego, CA), pp. 669–671, American Nuclear Society, 5-9 June 2005.

[41] J. Atanackovic, A. Yonkeu, J. Dubeau, S. H. Witharana, and N. Priest, "Characterization of neutron fields from bare and heavy water moderated ^{252}Cf spontaneous fission source using Bonner Sphere Spectrometer," *Appl. Radiat. Isotopes*, vol. 99, pp. 122–132, 2015.

[42] H. Wang and A. Enqvist, "Pulse height model for deuterated scintillation detectors," *Nuclear Instruments and Methods in Physics Research Section A: Accelerators, Spectrometers, Detectors and Associated Equipment*, vol. 804, pp. 167–174, 2015.

[43] E. Pirovano, R. Beyer, A. Junghans, N. Nankov, R. Nolte, M. Nyman, and A. Plompen, "Backward-forward reaction asymmetry of neutron elastic scattering on deuterium," *Physical Review C*, vol. 95, p. 024601, 2017.

[44] W. Mondelaers and P. Schillebeeckx, "GELINA, a neutron time-of-flight facility for high-resolution neutron data measurements," *Notiziario neutroni e luce di sincrotrone*, vol. 11, no. 2, pp. 19–25, 2006.

[45] R. Beyer, E. Birgersson, Z. Elekes, A. Ferrari, E. Grosse, R. Hannaske, A. Junghans, T. Kögler, R. Massarczyk, A. Matić, R. Nolte, R. Schwengner, and A. Wagner, "Characterization of the neutron beam at nELBE," *Nuclear Instruments and Methods in Physics Research Section A: Accelerators, Spectrometers, Detectors and Associated Equipment*, vol. 723, pp. 151–162, 2013.

[46] P. Baeten, M. Schyns, R. Fernandez, D. De Bruyn, and G. Van den Eynde, "MYRRHA: A multipurpose nuclear research facility," *EPJ Web of Conferences*, vol. 79, p. 03001, 2014.

[47] Eljen Technology, "EJ301, EJ309 data sheet." available at `http://www.eljentechnology.com/products/liquid-scintillators/ej-301-ej-309`.

[48] Eljen Technology, "EJ315 data sheet." available at `http://www.eljentechnology.com/products/liquid-scintillators/ej-315`.

[49] G. Knoll, *Radiation detection and measurement*. John Wiley & Sons, New York, third ed., 2000.

[50] M. Reginatto, "Overview of spectral unfolding techniques and uncertainty estimation," *Radiation Measurements*, vol. 45, no. 10, pp. 1323–1329, 2010. Proceedings of the 11th symposium on neutron and ion dosimetry.

[51] E. Dekempeneer, H. Liskien, L. Mewissen, and F. Poortmans, "A spectrometer for double-differential neutron-emission cross section measurements in the energy range 1.6 to 16 MeV," *Nuclear Instruments and Methods in Physics Research Section A: Accelerators, Spectrometers, Detectors and Associated Equipment*, vol. 256, pp. 489–498, 1987.

[52] S. Kopecky and A. Plompen, "R-matrix analysis of the total and inelastic scattering cross section of ^{23}Na," JRC scientific and technical reports JRC67884, EC Joint Research Centre, 2011.

[53] D. Tronc, J. Salomé, and K. Böckhoff, "A new pulse compression system for intense relativistic electron beams," *Nuclear Instruments and Methods in Physics Research Section A: Accelerators, Spectrometers, Detectors and Associated Equipment*, vol. 228, pp. 217–227, 1985.

[54] F. Gabriel, P. Gippner, E. Grosse, D. Janssen, P. Michel, H. Prade, A. Schamlott, W. Seidel, A. Wolf, and R. Wünsch, "The Rossendorf radiation source ELBE and its FEL projects," *Nuclear Instruments and Methods in Physics Research Section B: Beam Interactions with Materials and Atoms*, vol. 161–163, pp. 1143–1147, 2000.

[55] J. Teichert, A. Büchner, P. Evtushenko, F. Gabriel, U. Lehnert, P. Michel, and J. Voigtländer, "Results of beam parameter measurement of the ELBE electron accelerator after commissioning," *Nuclear Instruments and Methods in Physics Research Section A: Accelerators, Spectrometers, Detectors and Associated Equipment*, vol. 507, pp. 354–356, 2003.

[56] D. Gedcke and W. McDonald, "A constant fraction of pulse height trigger for optimum time resolution," *Nuclear Instruments and Methods*, vol. 55, pp. 377–380, 1967.

[57] V. Modamio, J. Valiente-Dobón, G. Jaworski, T. Hüyük, A. Triossi, J. Egea, A. D. Nitto, P.-A. Söderström, J. A. Ros, G. de Angelis, G. de France, M. Erduran, S. Ertürk, A. Gadea, V. González, J. Kownacki, M. Moszynski, J. Nyberg, M. Palacz, E. Sanchis, and R. Wadsworth, "Digital pulse-timing technique for the neutron detector array NEDA," *Nuclear Instruments and Methods in Physics Research Section A: Accelerators, Spectrometers, Detectors and Associated Equipment*, vol. 775, pp. 71–76, 2015.

[58] F. Brooks, "A scintillation counter with neutron and gamma-ray discriminators," *Nuclear Instruments and Methods*, vol. 4, pp. 151–163, 1959.

[59] GSI Helmholtzzentrum für Schwerionenforschung GmbH, Darmstadt, "Multi-Branch-System 5.0." available at `https://www.gsi.de/en/work/research/electronics/data_processing/data_acquisition/mbs.htm`, 2006.

[60] J. Birks, *The theory and practice of scintillation counting*, vol. 27 of *International series of monographs on electronics and instrumentation*. Macmillian, New York, 1964.

[61] G. Dietze and H. Klein, "Gamma-calibration of NE 213 scintillation counters," *Nuclear Instruments and Methods in Physics Research*, vol. 193, pp. 549–556, 1982.

[62] H. Klein, "Neutron spectrometry in mixed fields: NE213/BC501A liquid scintillation spectrometers," *Radiation Protection Dosimetry*, vol. 107, pp. 95–109, 2003.

[63] K. Gamage, M. Joyce, and N. Hawkes, "A comparison of four different digital algorithms for pulse-shape discrimination in fast scintillators," *Nuclear Instruments and Methods in Physics Research Section A: Accelerators, Spectrometers, Detectors and Associated Equipment*, vol. 642, pp. 78–83, 2011.

[64] J. Polack, M. Flaska, A. Enqvist, C. Sosa, C. Lawrence, and S. Pozzi, "An algorithm for charge-integration, pulse-shape discrimination and estimation of neutron/photon misclassification in organic scintillators," *Nuclear Instruments and Methods in Physics Research Section A: Accelerators, Spectrometers, Detectors and Associated Equipment*, vol. 795, pp. 253–267, 2015.

[65] H. Klein and S. Neumann, "Neutron and photon spectrometry with liquid scintillation detectors in mixed fields," *Nuclear Instruments and Methods in Physics Research Section A: Accelerators, Spectrometers, Detectors and Associated Equipment*, vol. 476, pp. 132–142, 2002. Int. Workshop on Neutron Field Spectrometry in Science, Technology and Radiation Protection.

[66] N. Kornilov, I. Fabry, S. Oberstedt, and F.-J. Hambsch, "Total characterization of neutron detectors with a ^{252}Cf source and a new light output determination," *Nuclear Instruments and Methods in Physics Research Section A: Accelerators, Spectrometers, Detectors and Associated Equipment*, vol. 599, pp. 226–233, 2009.

[67] A. Tomanin, J. Paepen, P. Schillebeeckx, R. Wynants, R. Nolte, and A. Lavietes, "Characterization of a cubic EJ-309 liquid scintillator detector," *Nuclear Instruments and Methods in Physics Research Section A: Accelerators, Spectrometers, Detectors and Associated Equipment*, vol. 756, pp. 45–54, 2014.

[68] G. Dietze, "Energy calibration of NE-213 scintillation counters by γ-rays," *IEEE Transactions on Nuclear Science*, vol. NS-26, pp. 398–402, 1979.

[69] N. Hawkes, J. Adams, D. Bond, S. Croft, O. Jarvis, and N. Watkins, "Measurements of the proton light output function of the organic liquid scintillator NE213 in several detectors," *Nuclear Instruments and Methods in Physics Research Section A: Accelerators, Spectrometers, Detectors and Associated Equipment*, vol. 476, pp. 190–194, 2002. Int. Workshop on Neutron Field Spectrometry in Science, Technology and Radiation Protection.

[70] D. Schmidt, B. Asselineau, R. Böttger, H. Klein, L. Lebreton, S. Neumann, R. Nolte, and G. Pichenot, "Characterization of liquid scintillation detectors," *Nuclear Instruments and Methods in Physics Research Section A: Accelerators, Spectrometers, Detectors and Associated Equipment*, vol. 476, pp. 186–189, 2002. Int. Workshop on Neutron Field Spectrometry in Science, Technology and Radiation Protection.

[71] X-5 Monte Carlo Team, *MCNP - A General Monte Carlo N-Particle Transport Code, Version 5*. Los Alamos National Laboratory, 2003. LA-UR-03-1987.

[72] G.Dietze and H.Klein, "NRESP4 and NEFF4 Monte Carlo codes for the calculation of neutron response functions and detection efficiencies for NE 213 scintillation detectors," Tech. Rep. PTB-Bericht ND-22, Physikalisch-Technische Bundesanstalt, 1982.

[73] H. H. Barschall, M. E. Battat, W. C. Bright, E. R. Graves, T. Jorgensen, and J. H. Manley, "Measurement of transport and inelastic scattering cross sections for fast neutrons. II. experimental results," *Physical Review*, vol. 72, p. 881, 1947.

[74] N. A. Bostrom, I. L. Morgan, J. T. Prud'homme, P. L. Okhuysen, and O. M. Hudson Jr, "Neutron interactions in lithium, carbon, nitrogen, aluminum, argon, manganese, yttrium, zirconium, radiolead and bismuth.," Tech. Rep. 59, 1959. Wright Air Devel. Centre Reports.

[75] W. Galati, J. D. Brandenberger, and J. L. Weil, "Scattering of neutrons by carbon from 3 to 7 MeV," *Physical Review, Part C, Nuclear Physics*, vol. 5, p. 1508, 1972.

[76] E. Haddad and D. D. Phillips, "Elastic and inelastic scattering of neutrons from C^{12}," *Bulletin of the American Physical Society*, vol. 4, p. 358(J2), 1959.

[77] M. Hosoe and S. Suzuki, "Gamma rays from neutron inelastic scattering of magnesium, aluminum, iron and bismuth," *Journal of the Physical Society of Japan*, vol. 14, p. 699, 1959.

[78] H. D. Knox, J. M. Cox, R. W. Finlay, and R. O. Lane, "Differential cross section and polarization for 2.63 MeV neutrons scattered from ^{12}C," *Nuclear Physics, Section A*, vol. 217, p. 611, 1973.

[79] R. O. Lane, A. S. Langsdorf Jr, J. E. Monahan, and A. J. Elwyn, "The angular distributions of neutrons scattered from various nuclei," *Annals of Physics (New York)*, vol. 12, p. 135, 1961.

[80] R. O. Lane, R. D. Koshel, and J. E. Monahan, "Polarization and differential cross section for neutrons scattered from ^{12}C," *Physical Review*, vol. 188, p. 1618, 1969.

[81] A. Langsdorf, J. , R. O. Lane, and J. E. Monahan, "Angular distributions of scattered neutrons," *Physical Review*, vol. 107, p. 1077, 1957.

[82] R. N. Little, Jr, B. P. Leonard, Jr, J. T. Prudhomme, and L. D. Vincent, "Liquid scintillator measurements of angular elastic scattering of neutrons from carbon, aluminum, and sulfur," *Physical Review*, vol. 98, p. 634, 1955.

[83] F. G. Perey and W. E. Kinney, "Carbon neutron elastic-and inelastic-scattering cross sections from 4.5 to 8.5 MeV," Tech. Rep. 4441, 1969. Oak Ridge National Lab. Reports.

[84] F. G. Perey and W. E. Kinney, "Elastic and inelastic scattering cross sections in the energy range 5.2 - 8.7 MeV.," Progress Report 42, 1978. U.S.AEC Nucl.Cross Sections Advisory Comm. Repts.

[85] A. Smith, R. Holt, and J. Whalen, "Neutron interaction with carbon-12 in the few-MeV region," *Nuclear Science and Engineering*, vol. 70, p. 281, 1979.

[86] M. Walt and J. R. Beyster, "Interaction of 4.1-MeV neutrons with nuclei," *Physical Review*, vol. 98, p. 677, 1955.

[87] H. B. Willard, J. K. Bair, and J. D. Kington, "Elastic scattering angular distributions of fast neutrons on light nuclei," *Physical Review*, vol. 98, p. 669, 1955.

[88] J. E. Wills, J. , J. K. Bair, H. O. Cohn, and H. B. Willard, "Scattering of fast neutrons from C^{12} and F^{19}," *Physical Review*, vol. 109, p. 891, 1958.

[89] J. Meija, T. Coplen, M. Berglund, W. Brand, P. D. Bièvre, M. Gröning, N. Holden, J. Irrgeher, R. Loss, T. Walczyk, and T.Prohaska, "Isotopic compositions of the elements 2013 (IUPAC Technical Report)," *Pure and Applied Chemistry*, vol. 88, pp. 293–306, 2016. IUPAC Technical Report.

[90] J. Meija, T. Coplen, M. Berglund, W. Brand, P. D. Bièvre, M. Gröning, N. Holden, J. Irrgeher, R. Loss, T. Walczyk, and T.Prohaska, "Atomic weights of the elements 2013 (IUPAC Technical Report)," *Pure and Applied Chemistry*, vol. 88, pp. 265–291, 2016. IUPAC Technical Report.

[91] D. Gayther, "International intercomparison of fast neutron fluence-rate measurements using fission chamber transfer instruments," *Metrologia*, vol. 27, pp. 221–231, 1990.

[92] A. Plompen, N. Nankov, C. Rouki, M. Stanoiu, C. Borcea, D. Deleanu, A. Negret, P. Dessagne, M. Kerveno, G. Rudolf, J. Thiry, M. Mosconi, and R. Nolte, "Method developing and testing for inelastic scattering measurements at the GELINA facility," *Journal of the Korean Physical Society*, vol. 59, no. 23, pp. 1581–1584, 2011.

[93] C. Budtz-Jørgensen, H. Knitter, and G. Bortels, "Assaying of targets for nuclear measurements with a gridded ionization chamber," *Nuclear Instruments and Methods in Physics Research Section A: Accelerators, Spectrometers, Detectors and Associated Equipment*, vol. 236, pp. 630–640, 1985.

[94] H. Junde, H. Su, and Y. Dong, "Nuclear data sheets for A=56," *Nuclear Data Sheets*, vol. 112, pp. 1513–1645, 2011.

[95] Y. Dong and H. Junde, "Nuclear data sheets for A=54," *Nuclear Data Sheets*, vol. 121, pp. 1–142, 2014.

[96] M. Bhat, "Nuclear data sheets for A=57," *Nuclear Data Sheets*, vol. 85, pp. 415–536, 1998.

[97] R. L. Becker, W. G. Guindon, and G. J. Smith, "Elastic scattering of 3.2 MeV neutrons from many elements," *Nuclear Physics*, vol. 89, p. 154, 1966.

[98] *Nuclear Science and Applications, Series B*, vol. 12/13, p. 13, 1981.

[99] J. R. Beyster, M. Walt, and E. W. Salmi, "Interaction of 1.0-, 1.77-, 2.5-, 3.25-, and 7.0-MeV neutrons with nuclei," *Physical Review*, vol. 104, p. 1319, 1956.

[100] N. A. Bostrom, I. L. Morgan, J. T. Prud'homme, P. L. Okhuysen, and O. M. Hudson Jr, "Interaction of fast neutrons in iron, lead, oxygen and hydrogen.," Tech. Rep. 59, 1959. Wright Air Devel. Centre Reports.

[101] S. W. Cierjacks, I. Schouky, and F. Voss, "Investigation of S-wave resonances and a possible doorway state in Fe below 850 keV." Private communication, 1978.

[102] L. Cranberg and J. S. Levin, "Neutron scattering at 2.45 MeV by a time-of-flight method," *Physical Review*, vol. 103, p. 343, 1956.

[103] R. B. Galloway and A. Waheed, "The differential cross section and polarization for the elastic scattering of 2.9 MeV neutron by Fe, Cu, I, Hg and Pb," *Nuclear Physics, Section A*, vol. 318, p. 173, 1979.

[104] W. B. Gilboy and J. H. Towle, "A neutron scattering study of Fe^{56}," *Nuclear Physics*, vol. 64, p. 130, 1965.

[105] R. W. Hill, "Small-angle elastic scattering of 5-MeV neutrons from carbon, aluminum, iron, copper, and lead.," *Bulletin of the American Physical Society*, vol. 1, p. 174(F1), 1956.

[106] R. W. Hill, "Angular distributions of elastic scattering of 5-MeV neutrons," *Physical Review*, vol. 109, p. 2105, 1958.

[107] B. Holmqvist and T. Wiedling, "Neutron elastic scattering cross sections, experimental data and optical model cross section calculations," Aktiebolaget Atomenergi, Stockholm/Studsvik Repts AE-366, 1969.

[108] B. Holmqvist, S. Johansson, G. Lodin, M. Salama, and T. Wiedling, "A neutron elastic scattering study of chromium, iron and nickel in the energy region 1.77 to 2.76 MeV," Aktiebolaget Atomenergi, Stockholm/Studsvik Repts AE-385, 1970.

[109] B. Holmqvist and T. Wiedling, "Optical model analyses of experimental fast neutron elastic scattering data," Aktiebolaget Atomenergi, Stockholm/Studsvik Repts AE-430, 1971.

[110] J. C. Hopkins and M. G. Silbert, "Inelastic scattering of 2- to 5-MeV neutrons by iron," *Nuclear Science and Engineering*, vol. 19, p. 431, 1964.

[111] A. Jacquot and C. Rousseau, "Fast neutron scattering cross sections of iron," *Nuclear Physics*, vol. 84, p. 239, 1966.

[112] W. E. Kinney and F. G. Perey, "Neutron elastic- and inelastic-scattering cross sections for 56Fe in the energy range 4.19 to 8.56 MeV," Tech. Rep. 4515, 1970. Oak Ridge National Lab. Reports.

[113] W. E. Kinney and J. W. Mcconnell, "High resolution neutron scattering experiments at ORELA," p. 1319, 1976. Int.Conf.on Interact.of Neutr.with Nuclei,Lowell 1976.

[114] *Ukrainskii Fizichnii Zhurnal*, vol. 22, p. 87, 1977.

[115] H. H. Landon, A. J. Elwyn, G. N. Glasoe, and S. Oleksa, "Neutron scattering at 2.2 MeV by time of flight," *Physical Review*, vol. 112, p. 1192, 1958.

[116] M. K. Machwe, D. W. Kent, Jr, and S. C. Snowdon, "Elastic scattering of 3.7-Mev neutrons from S, Fe, Co, Ni, Cu and Zn," *Physical Review*, vol. 114, p. 1563, 1959.

[117] M. V. Pasechnik, I. F. Barchuk, I. A. Totskiy, V. I. Strizhak, A. M. Korolev, Y. V. Gofman, G. N. Lovchikova, E. A. Koltypin, and G. B. Yan'kov, "Scattering and capture of fast neutrons by the nuclei," vol. 15, p. 18(2030), 1958. Second Internat. At.En. Conf., Geneva 1958.

[118] *Philosophical Magazine*, vol. 44, p. 1398, 1953.

[119] *Atomnaya Energiya*, vol. 3, no. 12, p. 498, 1957.

[120] O. A. Salnikov, "Angular distribution of elastic and inelastic scattering of 2.34 MeV neutrons from chromium, iron and lead," *Atomnaya Energiya*, vol. 3, no. 8, p. 106, 1957.

[121] A. Smith and P. Guenther, "Scattering of MeV neutrons from elemental iron," *Nuclear Science and Engineering*, vol. 73, p. 186, 1980.

[122] A. B. Smith, "Neutron scattering and models: Iron," *Nuclear Physics, Section A*, vol. 605, p. 269, 1996.

[123] Y. Tomita, K. Tsukada, M. Maruyama, and S. Tanaka, "Neutron scattering cross-sections of iron," in *Nuclear Data for Reactors Conference Proceedings*, vol. 2, (Helsinki), pp. 301–304, 15-19 June 1970.

[124] K. Tsukada, S. Tanaka, and M. Maruyama, "Inelastic scattering of neutrons by the time-of-flight method," *Journal of the Physical Society of Japan*, vol. 16, p. 166, 1961.

[125] K. Tsukada, S. Tanaka, Y. Tomita, and M. Maruyama, "Elastic and inelastic scattering of fast neutrons from iron, nickel andtungsten," *Nuclear Physics, Section A*, vol. 125, p. 641, 1969.

[126] E. Almen-Ramstrom, "A systematic study of neutron inelastic scattering in the energy range 2.0 to 4.5 MeV," Aktiebolaget Atomenergi, Stockholm/Studsvik Repts AE-503, 1975.

[127] A. W. Barrows, R. C. Lamb, D. Velkley, and M. T. McEllistrem, "Levels of ^{51}V and ^{55}Mn via (n,n'γ) reactions," *Nuclear Physics, Section A*, vol. 107, p. 153, 1968.

[128] R. Beyer, R. Schwengner, R. Hannaske, A. R. Junghans, R. Massarczyk, M. Anders, D. Bemmerer, A. Ferrari, A. Hartmann, T. Kogler, M. Roder, K. Schmidt, and A. Wagner, "Inelastic scattering of fast neutrons from excited states in ^{56}Fe," *Nuclear Physics, Section A*, vol. 927, p. 41, 2014.

[129] P. Boschung, J. T. Lindow, and E. F. Shrader, "Scattering of fast neutrons by ^{12}C, ^{54}Fe, ^{56}Fe, ^{58}Ni, and^{60}Ni," *Nuclear Physics, Section A*, vol. 161, p. 593, 1971.

[130] *Atomnaya Energiya*, vol. 23, no. 6, p. 568, 1967.

[131] S. F. Hicks, J. R. Vanhoy, A. J. French, S. L. Henderson, T. J. Howard, R. L. Pecha, Z. C. Santonil, B. P. Crider, S. Liu, M. T. Mcellistrem, E. E. Peters, F. M. Prados-Estevez, T. J. Ross, and S. W. Yates, "Studies of 54,56Fe neutron scattering cross sections," *EPJ Web of Conferences*, vol. 93, p. 02002, 2015.

[132] Tech. Rep. 2052, 1968. Oak Ridge National Lab. technical memo.

[133] *Ukrainskii Fizichnii Zhurnal*, vol. 22, no. 1, p. 112, 1977.

[134] vol. 1, p. 231, 1977. 4.All Union Conf.on Neutron Phys.,Kiev,18-22 Apr 1977.

[135] A. Mittler, J. Nardini, and G. P. Couchell, *Measurements of neutron inelastic scattering cross sections for natural iron.* PhD thesis, 1975. Thesis or dissertation.

[136] A. Negret, C. Borcea, and A. J. M. Plompen, "Neutron inelastic scattering measurements for background assessment in neutrinoless double β decay experiments," *Physical Review, Part C, Nuclear Physics*, vol. 88, p. 027601, 2013.

[137] Y. A. Nemilov, L. A. Pobedonostsev, and E. L. Teterin, ".inelastic scattering of neutrons on 56Fe nuclei," *Atomnaya Energiya*, vol. 53, no. 3, p. 194, 1982.

[138] W. L. Rodgers, E. F. Shrader, and J. T. Lindow, "Neutron scattering from C12, Fe54, Fe56, Cu65, Ni58, and Ni60.," Progress Report 1573, 1967. Chicago Operations Office,A.E.C.,Contract rept.

[139] M. Salama, "Inelastic scattering of fast neutrons from iron," *Atomkernenergie*, vol. 37, p. 221, 1981.

[140] T. Schweitzer, D. Seeliger, and K. Seidel, "Differentielle elastische und unelastische streuquerschnitte fur magnesium, silizium, eisen und wismut bei einer neutroneneinschussenergie von 3,4 MeV," *Kernenergie*, vol. 20, p. 174, 1977.

[141] Cross Section Evaluation Working Group, "ENDF/B-VI summary documentation," Report No. BNL-NCS-17541 (ENDF-201), Brookhaven National Laboratory, 1991. edited by P. F. Rose.

[142] K. Shibata, T. Kawano, T. Nakagawa, O. Iwamoto, J. Katakura, T. Fukahori, S. Chiba, A. Hasegawa, T. Murata, H. Matsunobu, T. Ohsawa, Y. Nakajima, T. Yoshida, A. Zukeran, M. Kawai, M. Baba, M. Ishikawa, T. Asami, T. Watanabe, Y. Watanabe, M. Igashira, N. Yamamuro, H. Kitazawa, N. Yamano, and H. Takano, "Japanese Evaluated Nuclear Data Library version 3 revision-3: JENDL-3.3," *J. Nucl. Sci. Technol.*, vol. 39, pp. 1125–1136, 2002.

[143] "The JEFF-3.1 Nuclear Data Library," JEFF Report 21, OECD Nuclear Energy Agency, 2006. edited by A. Koning, R. Forrest, M. Kellett, R. Mills, H. Henriksson and Y. Rugama.

[144] J. P. Svenne, L. Canton, K. Kozier, and L. Townsend, "Re-evaluating low-energy neutron-deuteron elastic scattering using three-nucleon theory," in *International Conference on Nuclear Data for Science and Technology*, vol. 1, (Nice), pp. 243–246, 22-27 April 2007.

[145] M. B. Chadwick, P. Obložinský, M. Herman, N. M. Greene, R. D. McKnight, D. L. Smith, P. G. Young, R. E. MacFarlane, G. M. Hale, S. C. Frankle, A. C. Kahler, T. Kawano, R. C. Little, D. G. Madland, P. Moller, R. D. Mosteller, P. R. Page, P. Talou, H. Trellue, M. C. White, W. B. Wilson, R. Arcilla, C. L. Dunford, S. F. Mughabghab, B. Pritychenko, D. Rochman, A. A. Sonzogni, C. R. Lubitz, T. H. Trumbull, J. P. Weinman, D. A. Brown, D. E. Cullen, D. P. Heinrichs, D. P. McNabb, H. Derrien, M. E. Dunn, N. M. Larson, L. C. Leal, A. D. Carlson, R. C. Block, J. B. Briggs, E. T. Cheng, H. C. Huria, M. L. Zerkle, K. S. Kozier, A. Courcelle, V. Pronyaev, and S. C. van der Marck, "ENDF/B-VII.0: next generation Evaluated Nuclear Data Library for nuclear science and technology," *Nuclear Data Sheets*, vol. 107, pp. 2931–3060, 2006. Evaluated Nuclear Data File ENDF/B-VII.0.

[146] A. Blokhin, B. Fursov, A. Ignatyuk, V. Koshcheev, E. Kulikov, B. Kuzminov, V. Manokhin, and M. Nikolaev, "Current status of Russian Evaluated Neutron Data Libraries," in *International Conference on Nuclear Data for Science and Technology*, vol. 2, (Gatlinburg, TN), pp. 695–698, 9-13 May 1994.

[147] E. Altstadt, C. Beckert, H. Freiesleben, V. Galindo, E. Grosse, A. R. Junghans, J. Klug, B. Naumann, S. Schneider, R. Schlenk, A. Wagner, and F. P. Weiss, "A photo-neutron source for time-of-flight measurements at the radiation source ELBE," *Ann. Nucl. Energy*, vol. 34, pp. 36–50, 2007.

[148] J. Klug, E. Altstadt, C. Beckert, R. Beyer, H. Freiesleben, V. Galindo, E. Grosse, A. R. Junghans, D. Légrády, B. Naumann, K. Noack, G. Rusev, K. D. Schilling, R. Schlenk, S. Schneider, A. Wagner, and F. P. Weiss, "Development of a neutron time-of-flight source at the ELBE accelerator," *Nucl. Instrum. Methods Phys. Res. A*, vol. 577, pp. 641–653, 2007.

[149] N. Nankov, A. J. M. Plompen, S. Kopecky, K. S. Kozier, D. Roubtsov, R. Rao, R. Beyer, E. Grosse, R. Hannaske, A. R. Junghans, R. Massarczyk, R. Schwengner, D. Yakorev,

A. Wagner, M. Stanoiu, L. Canton, R. Nolte, S. Röttger, J. Beyer, and J. Svenne, "The angular distribution of neutrons scattered from deuterium below 2 MeV," *Nucl. Data Sheets*, vol. 119, pp. 98–103, 2014.

[150] W. Glöckle, H. Witała, D. Hüber, H. Kamada, and J. Golak, "The three-nucleon continuum: achievements, challenges and applications," *Phys. Rep.*, vol. 274, pp. 107–285, 1996.

Acknowledgements

This work would not have been possible without the support and assistance of many people, and I would like to express my deepest gratitude and appreciation to those who, in different ways, contributed to the realisation of the thesis.

First, I would like to thank my promotors Prof. Wim Mondelaers and Prof. Luc Van Hoorebeke, for giving me to opportunity of pursuing my PhD at the University of Ghent and to work at the Joint Research Centre.

I am immensely grateful to my supervisor Dr. Arjan Plompen for his guidance throughout every step of this project. The discussions, corrections, and explanations have been a constant source of insightful ideas, significantly shaping my work and the thesis.

I am much obliged to Dr. Arnd Junghans and the Institute of Radiation Physics of the HZDR for hosting me in the last six months during the finalization of the data analysis and the writing.

My deepest appreciation goes to all colleagues I have been working with at GELINA, who always have been ready to help me with all matters related to my everyday struggles. I wish to acknowledge and thank Ruud Wynants for the design of the detector frame, Marzio Vidali and Danny Vendelbo for their assistance with the hated/loved but mostly hated DAQ, Dr. Markus Nyman and Dr. Carlos Paradela for proofreading the thesis. Thanks all colleagues of the SN3S unit and the fellow students, for always being so supportive, for the enjoyable working environment, and for making my stay in Belgium a memorable experience.

In addition to the JRC, I was lucky enough to carry out my measurements in two other institutes and I am thankful to the colleagues from nELBE and from the PTB Neutron Radiation department for sharing their expertise, and for their support before, during and after the experiments.

Sembrano passati un milione di anni da quando sono arrivata a Geel la prima volta, e ancora non ci credo di essere riuscita ad arrivare viva alla fine. Non ho parole a sufficienza per esprimere cosa questa esperienza ha significato per me, vorrei peró ringraziare ancora una volta tutte le persone che ho incontrato in questi anni per averli resi indimenticabili, e in particolare amici e famiglia, per essermi stati vicini anche da lontano, per il sostegno e l'incoraggiamento costanti, per avermi supportato e sopportato, grazie di cuore!